CONFIDENTIAL

Advanced Control of Coating Weight in a Hot-Dip Galvanizing Line

An adaptive time-delay compensation strategy

Saket Sarawgi

Master of Science Thesis

Delft University of Technology

Delft Center for Systems and Control

MSCCONFIDENTIAL

Advanced Control of Coating Weight in a Hot-Dip Galvanizing Line

An adaptive time-delay compensation strategy

Master of Science Thesis

For the degree of Master of Science in Systems and Control at Delft University of Technology

Saket Sarawgi

August 16, 2020

Faculty of Mechanical, Maritime and Materials Engineering (3mE) · Delft University of Technology

The work in this thesis was supported by Tata Steel Europe in IJmuiden. Their cooperation is hereby gratefully acknowledged.

Delft University of Technology
Department of
Delft Center for Systems and Control (dcsc)

The undersigned hereby certify that they have read and recommend to the Faculty of Mechanical, Maritime and Materials Engineering (3mE) for acceptance a thesis entitled

Advanced Control of Coating Weight in a Hot-Dip Galvanizing Line

by

Saket Sarawgi

in partial fulfillment of the requirements for the degree of

Master of Science Systems and Control

Dated: August 16, 2020

Supervisor(s): dr.ir. Riccardo Ferrari

Reader(s): dr.ir. Manuel Mazo Jr

dr. Yichao Liu

ir. Cor Jan Boeder

Abstract

Flat steel strip processing is carried out through a sequence of continuous methods, commonly recognized as hot rolling, pickling, cold rolling, annealing, and hot-dip galvanizing. Among all these processes, hot-dip galvanizing is a process that has been popularly used to produce high quality galvanized cold-rolled sheets that are extensively used in the manufacture of automobile and domestic electrical appliances. In particular, the main objective of galvanizing is to protect the steel strip from corrosion by applying a suitable coating of zinc-based alloy.

During hot-dip galvanization, the steel strip after leaving the annealing furnace is dipped into a bath of molten zinc, enabling the formation of zinc coating. The amount of this coating is controlled by the widely used air-knife wiping system installed just above the zinc bath. The coating thickness obtained after the wiping process depends mainly on the strip speed, wiping gas pressure, and strip-to-knife distance. After a significant distance from the air knives, the cold coating gauge is located to measure the thickness of the zinc coating.

The quality of the product depends on the amount of zinc-based alloy deposited at the strip's surface. The over-deposition of zinc at the strip surface results in excessive use of zinc, which is expensive, and under-coated strip results in a product of poor quality. The control of the coating deposition is based on the air-knife wiping pressure, and therefore, the challenge is to determine and control the pressure, given the operating conditions, which are the strip speed, strip-to-knife distance, and the target coating thickness.

One of the main concerns in the closed-loop control of coating thickness is the need to account for the measurement delay arising from the time-varying strip speed across the gap between the air knives and the cold coating gauge. In this thesis, different modeling and control strategies have been studied to improve the quality of the galvanized sheet produced at Hot-dip Galvanizing Line 1 (HDGL) of Tata Steel in IJmuiden.

Table of Contents

List of Figures

List of Tables

Acknowledgements

I would like to thank my academic supervisor Dr. Riccardo M.G. Ferrari, for his guidance and assistance throughout this study and also for encouraging me to do my thesis with Tata Steel Europe. Thank you for always providing me with your valuable input at times when I was stuck with problems.

I am also very grateful to the Thermal Processing group at Tata Steel Europe in IJmuiden for allowing me to carry out the thesis with them. In particular, I would like to thank Dr. Berend Brasjen and Cor Jan Boeder for their support and valuable insights during the course of the thesis. Thank you for planning productive weekly meetings and regular discussions that helped me produce this final work. Additionally, I would like to thank Jaap van Eenennaam for performing the experiments to realize the pressure distribution profiles.

Finally, and most importantly, I would like to thank my family and friends for their constant support and belief in me over the past years.

Delft, University of Technology
August 16, 2020

Saket Sarawgi

Chapter 1

Introduction

Tata Steel's Hot-dip Galvanizing Line 1 (HDGL) at IJmuiden is committed to the manufacture of galvanized steel coils primarily for the automotive industry. In the galvanizing line's continuous process, the steel strip is annealed and then covered with a thin layer of zinc-based alloy to shield the strip from corrosion. This zinc layer coating formed on the strip has to meet quality requirements associated with its appearance, thickness, and uniformity.

In the HDGL process, the steel strip undergoes a heating treatment in the annealing furnace to modify the properties of cold-rolled steel. During the course of annealing, recrystallization occurs, and new grain structures are formed, which increases the ductility. Upon leaving the annealing furnace, the strip is immersed into a bath of liquid zinc at a temperature of around 730K [51], enabling the zinc coating to develop. The amount of zinc held on the strip as it extracts from the bath is controlled by the commonly used air-knives wiping system. The excess liquid zinc is immediately wiped off, and the remaining is solidified when transported along the cooling section. After a significant distance from the air knives, the cold coating gauge is located to measure the thickness of the zinc coating. The zinc-coated steel strip is further temper rolled to have a uniform surface texture.

One of the key objectives in this process is to control the zinc layer coating thickness. The air-knives placed just above the zinc bath work either with compressed dry air or nitrogen. The final coating thickness in the galvanizing process after the air-knives wiping system depends mainly on the air-knife wiping pressure, the strip-to-knife distance, and the strip speed.

The quality of the steel depends on the thickness of the coating, that is, the amount of zinc deposited at the surface of the strip. An under-coated strip leads to poor-quality/rejected products, and an over-coated strip leads to overuse use of zinc, which is expensive. In order to increase the efficiency of the galvanizing process, and the uniformity of the coating thickness, many different modeling, and control strategies have been studied by various researchers.

In a galvanizing line, the strip speed depends on the operating conditions of the annealing furnace and the buffer level in the entry/exit accumulators. Therefore, the strip speed may be changed at any point of time to suit the furnace operation [14]. Moreover, the strip-to-knife distance is significantly limited by the strip shape and stability. So, the challenge is to determine and control the optimum chamber pressure, given the operating conditions, which are the strip speed, strip-to-knife distance, and the target coating thickness.

Although the literature addresses coating thickness for the coating in any given application, the normal practice is to specify and manufacture to meet a given coating weight. As the density of the zinc layer [kg/m^3] is known, the thickness of the galvanized layer [mm] can easily be computed once the coating weight per unit area [g/m^2] is determined. In this thesis, modeling and control of coating weight is discussed.

1-1 Current Status

It has been well-established that, in most environments, coating weight is essential to determine the expected life of the galvanized steel in any given application. Therefore, hot-dip galvanized surface products are manufactured according to stringent coating weight requirements.

A control system is often integrated into the air-knife wiping method to improve both the quality and the uniformity of the coating weight. For this control system, a mathematical model is necessary to determine the coating weight based on the different process variables. The galvanizing process is complex, with multiple process variables influencing the final coating weight. Consequently, the industries seem to rely on an empirical model that is easy to build and put into implementation. The major drawback of an empirical model is that it is applicable only for the process design when acquiring the database.

Currently, Tata Steel makes use of a feed-forward controller that corrects for the measured disturbances and reference changes. It consists of a power-law model that determines the required changes in the control inputs to directly account for the impact of process fluctuations before the zinc layer is affected. Therefore, the feed-forward controller can only be triggered by measurable disturbances, the effect of which can be modeled on the coating weight. The empirical model's precision and reliability are of prime importance.

The galvanizing process can be prone to variations induced by unmeasured disturbances and variables whose effects on coating weight cannot be predicted [19]. Therefore, the residual prediction errors and unmeasured disturbances cannot be addressed by a feed-forward controller. At times, when zinc coating weight achieved is less than the reference (because of prediction model inaccuracy), the portions of the coil need to be cut out that do not meet the specifications.

In fact, residual prediction error and unmeasured disturbances can only be corrected after the cold coating gauge has measured its consequences. As a result, they can be addressed by coating weight feedback control. Furthermore, a physical model of the galvanizing process using the first principles might improve the prediction accuracy. Accomplishing advanced feedback control strategy along with a better prediction model would increase the process quality, which in turn lead to advantages, such as reduced rejections, waste, and operating cost.

1-2 Goals and Motivation of the thesis

Many industrial processes demonstrate time delays in their dynamic behavior. Dead times are mostly induced by information, electricity, or mass transport phenomena. Systems with time delays have often required additional efforts in the area of control engineering to develop an effective method. A delayed response to the applied inputs may result in a control performance that is too aggressive after the time delay has passed, resulting in a high overshoot or instability.

The easiest analogy that can be offered to explain the complexity of handling such systems comes from real life: an individual who needs to take a shower. The individual will regulate the hot water tap to achieve the optimum temperature, but the effects of his adjustments will only be sensed by his skin, which acts as a sensor after the water has traveled through the water tubes (transportation delay). Therefore, the individual, who tends to achieve optimal temperature at the earliest moment, will be vulnerable to turn the knob too fast, producing too hot or too cold water.

The issues with time delay described above have another aspect because the time delay varies in time. It leads us to the real challenge of this study i.e., the zinc coating weight obtained after the air-knives due to control actions or process disturbances will not be measured until that section of the strip has reached the coating gauge. The strip must be cooled before it passes through the cold gauge, which is placed about 150 meters downstream from the air-knives. Therefore, the gap between the air-knives and the coating gauge results in a time delay, which relies on the strip's speed.

This thesis aims to study different characteristics of the air-knife wiping process to model the coating weight according to different process parameters. To cope with such a highly non-linear complex phenomenon and compensate for the substantial time-varying measurement delay, it becomes essential to incorporate an advanced control to avoid the associated unreliability. The goal is to improve the quantity and the quality of the galvanized sheet produced at HDGL of Tata Steel in IJmuiden.

The main challenges to control the coating weight of the zinc layer are:

- The strip speed might change too often, causing coating weight transients.
- Usually, the target coating weight is constant over the length of one coil, and therefore, an accurate control is needed at the beginning of the coil when the reference coating weight changes [14].
- There exists a time-varying measurement delay between the air knives and the coating gauge, which has a deteriorating effect on the behavior of the feedback system [22].

1-3 Structure of the thesis

This study consists of nine chapters, which are arranged as follows. Following a brief introduction and goal of this thesis in this chapter, Chapter 2 outlines the series of different processes realized for the production of a flat steel strip.

Chapter 3 provides background knowledge on the galvanizing process, the coating weight control equipment, and the coating gauge. In addition, the first-principle coating weight model is described as a function of various process parameters such as the strip speed, air-knife wiping pressure, and the strip-to-knife distance.

The first-principle coating weight model includes pressure and shear-stress correlations that are specific to the air-knife setup employed in the galvanizing line. Therefore, in Chapter 4, these correlations are appropriately parameterized and estimated using non-linear system identification techniques. The results from the first principle model are also compared with the existing power-law model.

In Chapter 5, properties of time delay in continuous-time and discrete-time are discussed. Furthermore, a discrete-time formulation of the time-varying measurement delay is presented. Chapter 6 talks about the choice of sampling time and model discretization.

In Chapter 7, one of the most popular dead-time compensation strategy known as Smith Predictor is discussed. At first, the PI controller is tuned considering two main control objectives: reference tracking and disturbance rejection. Later, closed-loop simulations are performed to analyze the performance of the control achieved.

In Chapter 8, an advanced control algorithm known as Non-linear Extended Prediction Self-Adaptive Control (NEPSAC) is explained with some modifications to deal with variable time delay. Moreover, closed-loop simulations are performed and compared to the PI controller.

Lastly, Chapter 9 presents a discussion of the results presented in Chapters 4, 7, and 8. This chapter also provides insight into potential future work.

Chapter 2

Processing of Steel

Tata Steel in IJmuiden is Europe's second-largest producer and distributor of steel. It supplies more than 7 million tones of high quality coated steel in the form of rolls, which is used in many fields such as the automobile, construction, and packaging industries. The product is often used in batteries, tubes, industrial vehicles, and white goods such as refrigerators and stoves [1]. The demand for the production of high-strength steel has been actively increasing, since the last few years because of its increasingly lightweight applications [23, 33]. To produce Advanced or Ultra-high strength steel, it is desired to have thinner, stronger, and more ductile steel than the conventional low to high strength steel.

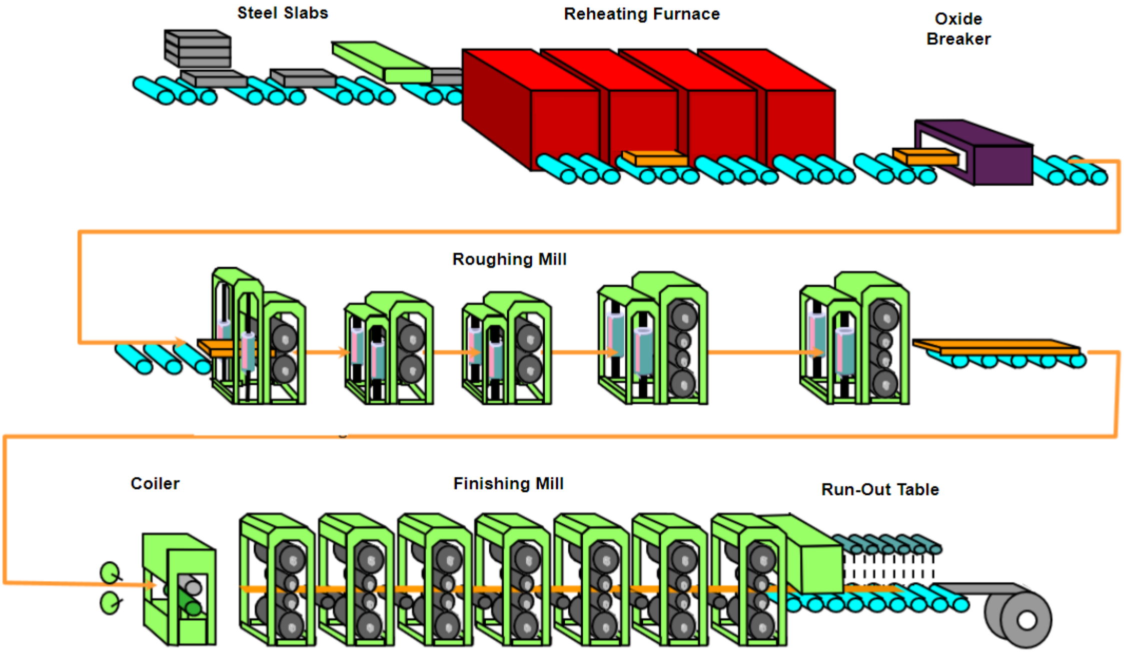

Figure 2-1: Schematic layout of hot strip mill, adapted from [25]

2-1 Hot Rolling

In the processing of steel, the Hot Strip Mill (HSM) is used to minimize the thickness of the strip to a few millimeters by rolling thick slabs of hot steel in several steps starting from the heating furnace, the roughing mill, the finishing mill, the laminar cooling to the coiler as shown in Figure 2-1.

The steel slabs enter the mill either directly from the continuous caster or from the yards, held in the storage, and cooled. These slabs are first heated at a temperature of around 1500K in the reheat furnaces to reduce the yield stress [39]. The slab then exits the furnace on the roller tables as depicted in Figure 2-2. During reheating, oxidation causes a thick scale to build upon the slab's surface, which is removed by scale breakers and high-pressure water jets [11]. The slab is then passed through the roughing mill, which consists of several horizontal rollers called roughing rollers (to reduce the strip thickness) and vertical rollers called edging rollers (to control the strip width) as depicted in Figure 2-3. At this stage, the slab is translated to what is called a transfer bar [49]. The transfer bar then might be coiled in a coil-box, to reduce the total required mill length as opposed to the straight-through mill.

Figure 2-2: Reheating furnace

Figure 2-3: Roughing mill

The transfer bar is uncoiled from the coil-box and moved across the finishing mill at a temperature of approximately 1350K [11], where the strip further undergoes more precise deformation before cold rolling. The finishing mill consists of several stands with loopers in between, as shown in Figure 2-4. By moving the strip over the loopers, it can be buffered and tensioned. The strip leaves the stand at a temperature of about 1150K and moves on the run-out table, where it is cooled at a regulated pace by a sequence of water jets, as shown in Figure 2-5. In the end, the strip is coiled in the coiler. It is essential to note that the temperature at the end of finishing mill, the cooling rate in the run-out table, and the final winding temperature all have implications on the final structure and mechanical properties of steel [49].

The rolling process consists of two stages - hot rolling and cold rolling. Hot rolling reduces the thickness of the steel slabs into coils of strip that can be used as a final product, or they can also be further cold-rolled to produce strips of finer thickness and surface finish.

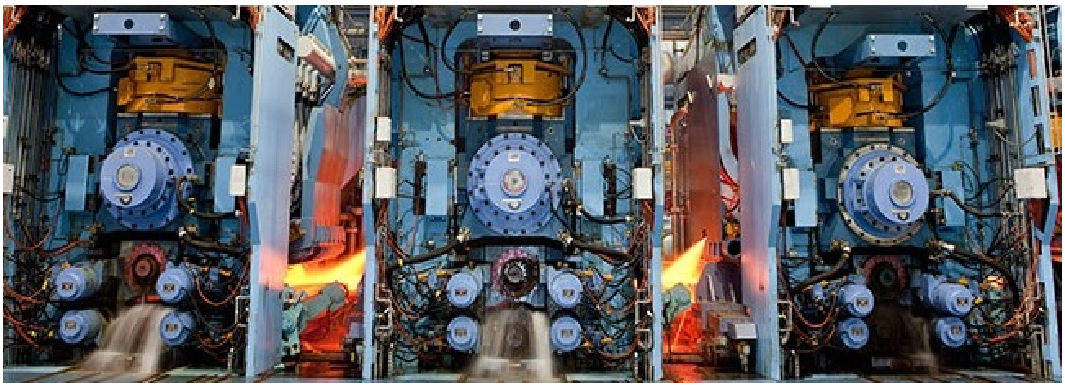

Figure 2-4: Finishing mill with loopers in between

Figure 2-5: Run out table

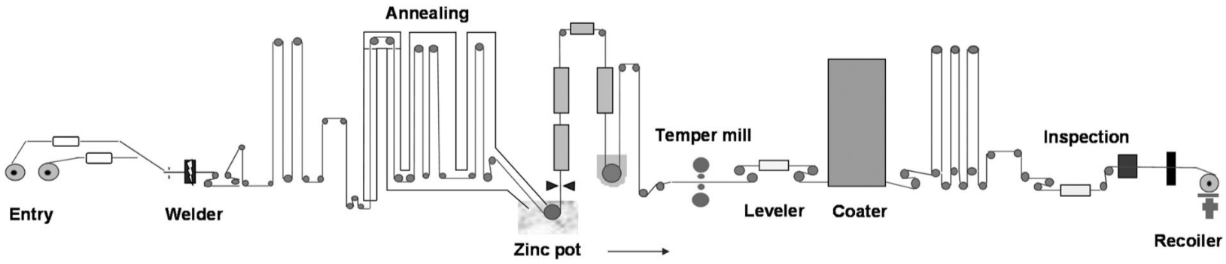

Figure 2-6: Schematic layout of continuous galvanizing line [50]

2-2 Cold Rolling, Annealing and Galvanizing

The strip surface will again have an accumulated scale due to the high raised temperature of the hot rolling process. Before further processing, this scale is extracted by a technique called pickling in which the coil is cleaned by either sulphuric or hydrochloric acid to remove the surface oxide formed during the hot rolling process. The coil can then be cold rolled. In order to further minimize the thickness of the steel strip, the coil is passed through a set of roll stands during this process. Cold rolling is similar to hot rolling except for the fact that it is not pre-heated [8]. The term 'cold' means that the procedure is carried out at a temperature below the steel's recrystallization temperature [49]. The cold-rolled strip is continuously annealed and galvanized, followed by temper rolling and/or surface treatment in the Hot-dip galvanizing line (HDGL), as shown in Figure 2-6.

After cold reduction, the strip possesses high hardness and low ductility, and therefore, it undergoes a heat treatment known as annealing to produce the desired microstructure and mechanical properties. For example, in the Galvanizing Line 2 of Tata Steel, the strip passes through the installations of Preheating furnace (PHF), Direct fired furnace (DFF), a Radiant tube heater (RTH) and a Gas jet cooler (GJC) as shown in Figure 2-7. All of these installations have different dimensions, working structures, and thermal dynamics. The strip is first heated in PHF by DFF produced hot flue gases, and then in DFF, where the main burners are mounted, and combustion occurs. The strip hits the highest temperature in RTH before cooling down in GJC. In fact, a safe gas layer within RTH and GJC is retained to prepare the strip for the galvanizing process [50].

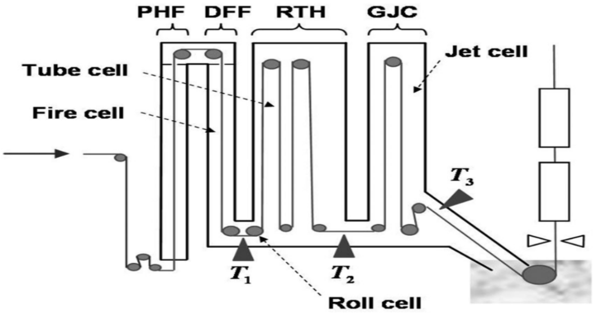

Figure 2-7: Schematic layout of continuous annealing section [50]

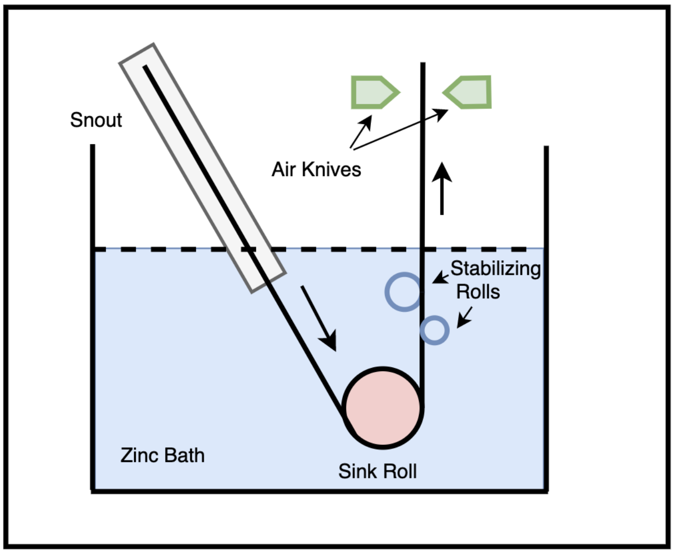

Figure 2-8: Schematic layout of the galvanizing bath

To ensure excellent corrosion tolerance, the strip is further continuously submerged in a bath of molten zinc around the temperature of 750K. As shown in Figure 2-8, the strip enters the bath through the snout, passes under the sink roll, and exits vertically from the bath between two asymmetrically placed stabilizing rollers. The amount of the zinc accumulated on the strip after it escapes from the hot bath is regulated by the air knives, which cause the excess zinc to move back into the bath by applying high pressure to the moving strip.

Towards the end of the line, the strip goes through the temper mill. It is another rolling method to manage the surface finish of the strip. The strip then passes through a tension leveler where it is tightly worked up and down so as to normalize the stress, reduce the strain marks, and provide a smooth surface texture to the coated strip. Just before the final inspection, the strip might be coated with oil/color as per the customer's requirement. Finally, the strip is inspected to ensure that the surface quality is in the acceptable range. The final cold-rolled sheet is characterized by improved surface quality and greater uniformity of thickness and annealed mechanical properties compared to the hot-rolled strip.

Galvanized steel products have been in demand for the assembly of modern vehicles as they are lightweight and more immune to the impact. The production of galvanized steel poses many difficulties for the manufacturers, such as the need to cover a range of low cost, high strength steel grades with reduced zinc consumption and minimal surface defects [2]. Therefore, in this thesis, different modeling and control strategies will be studied for controlling the coating (zinc) weight by the air-knives, to improve the zinc yield and thus increasing the effectiveness of the wiping control while satisfying customer requirements.

Chapter 3

Process Background

3-1 Process Description

3-1-1 Hot dip galvanizing

The research is focused on the Hot-dip galvanizing line (HDGL), which comes after the cold rolling process. In the hot-dip galvanizing process, the cold-rolled steel strip is continuously immersed in a bath with molten zinc, where the hot liquid zinc is applied to the surface of the strip. The air-knife wiping device located just above the zinc bath and near the liquid level, as shown in Figure 3-1 controls the weight of the zinc layer. In order to solidify the zinc coating, the strip is passed through a cooling tower. Finally, the zinc coating weight is determined with the help of an X-ray device called cold coating gauge.

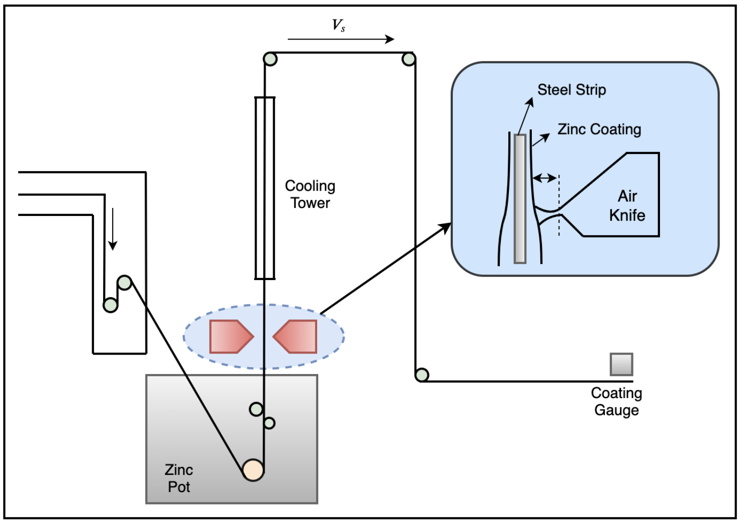

Figure 3-1: Schematic of hot-dip galvanizing process

Galvanizing is the process of applying molten zinc to the steel strip to prevent it from corrosion. The two types of galvanizing processes that have been known for a long time are hot-dip galvanizing process and electroplating. In the hot bath, the iron in the steel combines with the liquid zinc to yield a uniformly bonded alloy coating that gives corrosion resistance to the steel strip. Also, zinc has a sacrificial behavior, i.e., if the coating is damaged, then the corrosion will occur only in the zinc. The simplicity and lower cost of the hot-dip galvanizing process have more distinct advantages than electroplating [38].

3-1-2 Line Description

Tata Steel's Hot Dip Galvanizing Line 1 (HDGL) at IJmuiden is designed to supply the automotive market with galvanized steel coils of strip thickness up to 2.1 mm. The line processes steel at different speeds (60 m/min to 150 m/min) for a wide range of coating weight requirements i.e. from 45 g/m^2 up till 180 g/m^2. The wide product range implies that the air knives wiping system experiences multiple line speed and coating weights transients. One of the most important features of this galvanizing line is that almost half of the product mix is for exterior automotive panels requiring high surface quality. Therefore, the galvanizing line received major improvements to boost productivity, reliability, and quality of the product to comply with customer orders.

3-1-3 Coating Weight Control Equipment

The wiping equipment incorporated in the Hot Dip Galvanizing Line 1 (HDGL) at IJmuiden is similar to the one shown in Figure 3-2. Two parallel air knives, which move jointly and symmetrically (Figure 3-1), are mounted on a rig, as shown in the Figure 3-2. They are used to blow off excess zinc coating from both the sides of the steel strip by inducing a high-velocity and horizontally extended jet towards the moving strip. Each side is driven by two motors to control the distance to the center-line from where the strip is moving [36]. The gap between the upper and lower lip of the nozzle is kept constant at 1 mm. The two most important factors influencing the air-jet effect are the strip-to-knife distance and the wiping gas pressure.

Figure 3-2: Typical air-knife wiping equipment

3-1-4 Coating gauge

The zinc coating weight applied to the steel strip is measured by a scanning radiation gauge that utilizes the X-Ray Fluorescence (XRF) principle. A primary beam of photon radiation with adequate energy is transmitted to the coated steel strip to stimulate excitation and emission of X-rays. The excitation of iron atoms in a steel strip leads to emission with 6.4 keV of energy from fluorescent radiation.

The "iron fluorescence" radiation is attenuated when the steel strip is coated with another material. As the weight of the zinc coating increases, less radiation released by the steel will travel through the coating. Therefore, the fluorescence emission of the coating element can be used to determine the coating weight measurements [7]. The X-Ray coating gauge scans back and forth across the strip width giving periodic measurements of the deposited coating weight [29]. Figure 3-3 displays the standard zig-zag path created by scanning measurement.

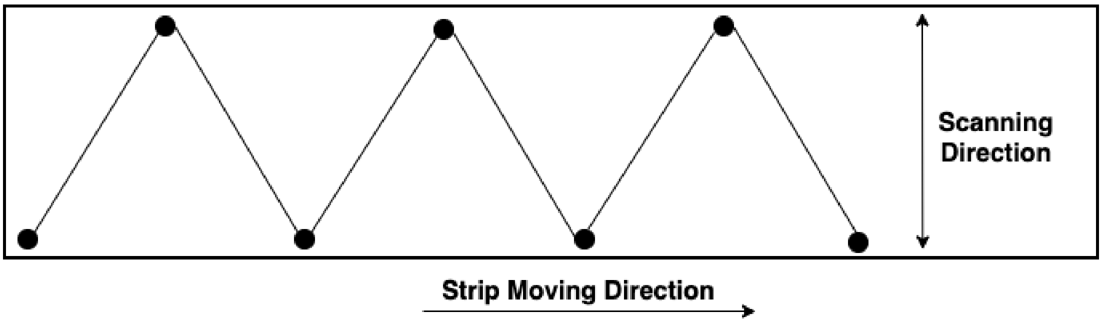

Figure 3-3: Zig-Zag scan pattern of gauge

The cold coating gauge has good accuracy but cannot operate at very high temperatures, such as that of molten zinc, and therefore, it must be placed at a considerable distance from the zinc bath, where the strip is cooler [10]. Recently, the use of hot coating gauge installed just after the air knives has also been discussed in the literature. Still, it failed because of the cost associated with maintenance and difficulties related to installation. It requires a strip vibration damping system along with the sensor to get a reliable measurement [18].

The accurate control of coating weight is of great importance as the over-deposition of zinc on the steel strip results in excessive use of zinc, which is expensive, and the under-deposition results in the product of low quality or even rejections. As already discussed, the quality of the steel strip is related to the amount of zinc deposited at the surface. The hot-dip galvanizing process has some complex characteristics, such as non-linear behavior, large time-varying delay, and unmeasured disturbances which makes the controller design difficult. The control problem is to manipulate the air-knife pressure, given the known disturbances: strip speed and strip-to-knife distance. In the following sections, a model-based approach using the first principle is discussed, for developing the coating weight model.

3-2 Coating Weight Model Assumptions

Figure 3-4 illustrates the graphical depiction of the air-knife wiping process in the hot-dip galvanizing process and the correct coordinate scheme. The coating weight model is based on the below-mentioned assumptions [46] :

1. The fluid flow in the liquid coating layer can be represented by the steady-state, two-dimensional equations of incompressible, constant viscosity creep flow.

2. With the boundary layer analysis methods, the equation representing the fluid flow within the comparatively narrow coating film can be linearized.

3. The effect of surface tension, the surface roughness of the oxidation substrate, and the formation of interface alloys can be ignored.

4. At the strip-fluid interface, there is no slip between the strip and the fluid coating.

5. Air-knife jet action exerts only a normal force on the surface of the coating.

6. It is presumed that the pressure through the thin coating film is constant as the velocity of the coating layer flow in the direction perpendicular to the strip surface is small in contrast to the flow velocity in the direction parallel to the strip.

7. The coating layer weight differs across the strip, and fluid properties, including viscosity, density, and thermal conductivity, are unchanged.

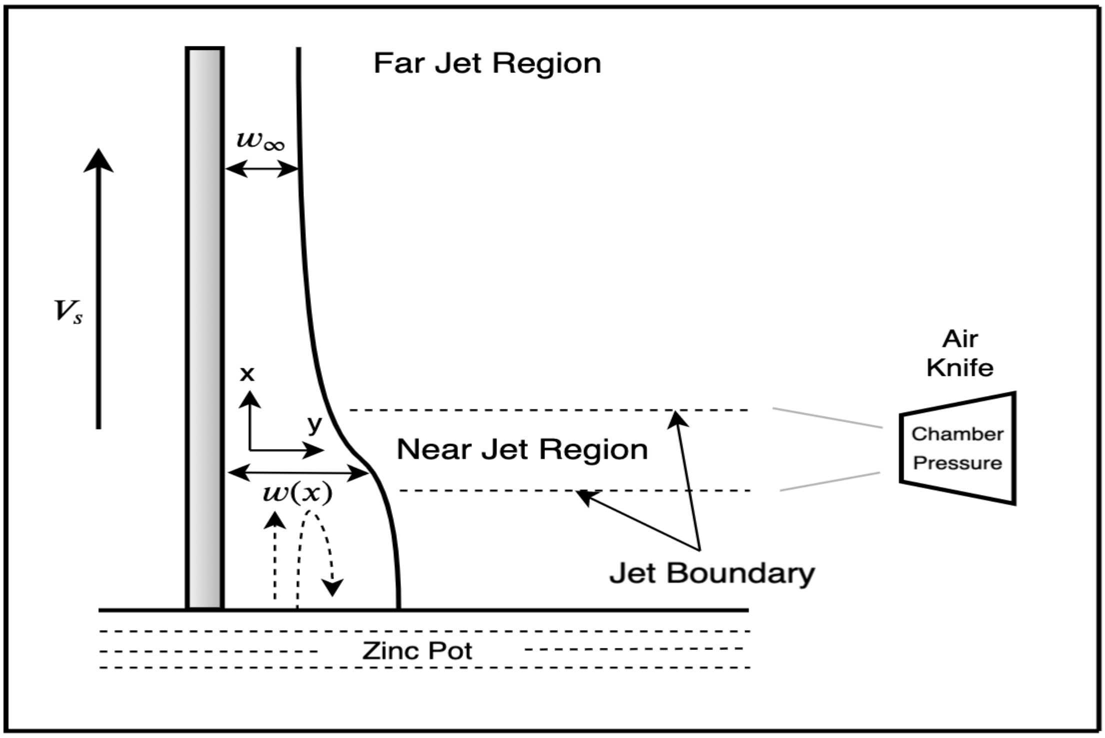

Figure 3-4: Schematic of air-knife wiping system, adapted from [16]

3-3 Coating Weight Model

In 1976, Thornton and Graff [46] developed a coating weight model on the basis of the "maximum flux" principle for the air-knife wiping process in which the jet effect was defined only by the gravity force and the pressure gradient. In their study, they ignored the effect of the wall shear stress from the wiping jet.

Later, Ellen and Tu [15] in 1984 and Tu and Wood [47] in 1996, improved the model by including surface shear stress along with the pressure gradient on the coating. The inclusion of shear stress into the concept of coating weight led to an enhanced alignment with the findings of industrial coating weight. In 2007, Elsaadawy et al. [16] further improved the model by developing new relationships for pressure and surface shear stress in the near-field of the air-knife region.

The critical stage in the coating weight model is to evaluate the liquid zinc steady-state flux, q, using a simple form of the Navier Stokes equation [15, 16]. The **Navier Stokes equation** for a thin film on a plane, with the assumptions stated in the previous section, reduces to:

$$\mu \frac{d^2u}{dy^2} = \rho g + \frac{dp}{dx} \tag{3-1}$$

where u is coating fluid velocity parallel to the strip in the vertically upward direction, x is the coordinate along the strip, y is the coordinate normal to the strip, ρ and μ are the coating fluid density and viscosity, respectively, g is the gravitational acceleration and dp/dx is the pressure gradient in the x direction.

Equation 3-1 indicates that the resultant coating fluid motion arises from an equilibrium between the viscous shear force, the gravitational force and the pressure gradient caused by the air-knives on the coating surface in the coating fluid [34].

The **boundary conditions** are:

$$\begin{aligned} u &= V_s \quad \text{at} \quad y = 0 \\ \mu \frac{du}{dy} &= \tau \quad \text{at} \quad y = w \end{aligned} \tag{3-2}$$

where V_s is the velocity of the strip, w is the coating thickness and τ is the shear stress imposed on the coating by the jet flow.

Equation 3-1 is solved subject to boundary conditions given by Equation 3-2, representing a combined **Poiseuille-Couette flow**:

$$u = V_s \left(1 + \frac{y}{w} SW - \frac{y}{w} \left(2 - \frac{y}{w} \right) \frac{GW^2}{2} \right) \tag{3-3}$$

where W, S and G are the non-dimensional coating thickness, shear stress and effective gravitational acceleration given by:

$$
\begin{aligned}
W &= w\sqrt{\frac{\rho g}{\mu V_s}} \\
S &= \frac{\tau}{\sqrt{\rho \mu V_s g}} \\
G &= 1 + \frac{1}{\rho g}\frac{dp}{dx}
\end{aligned}
\tag{3-4}
$$

According to **conservation of mass**, "the net vertical mass flow rate at any position is equal to the final coating mass multiplied by the strip velocity" [16]. So, the **withdrawal rate** of liquid zinc, q, can be expressed as:

$$
q = \int_{y=0}^{y=w} u(x,y)dy \tag{3-5}
$$

Substituting Equation 3-3 in the above equation we get:

$$
\begin{aligned}
q &= \int_{y=0}^{y=w} \left(V_s + \left(\frac{SWV_s}{w} - \frac{GW^2V_s}{w} \right) y + \frac{GW^2V_s}{2w^2} y^2 \right) dy \\
q &= V_s w + \frac{SWV_s w}{2} - \frac{GW^2V_s w}{2} + \frac{GW^2V_s w}{6} \\
\boldsymbol{q} &= \boldsymbol{V_s w \left(1 + \frac{SW}{2} - \frac{GW^2}{3} \right)}
\end{aligned}
\tag{3-6}
$$

Introducing the non-dimensional withdrawal flux, Q, Equation 3-6 transforms to:

$$
Q = W + \frac{SW^2}{2} - \frac{GW^3}{3} \tag{3-7}
$$

where

$$
Q = \frac{q}{V_s}\sqrt{\frac{\rho g}{\mu V_s}}
$$

From Equation 3-4, it is clear that G and S are known from the pressure and shear stress profile on the strip. Furthermore, under steady-state conditions, Q must remain constant when W changes its response to a changing G and S caused by the air knives. The non-dimensional coating thickness W, according to Ellen and Tu [15], corresponds to the maximum withdrawal flux, Q_{max}, and it is calculated by solving $dQ/dW = 0$.

$$
\frac{dQ}{dW} = 1 + SW - GW^2 = 0 \tag{3-8}
$$

$$
\boldsymbol{W = \frac{S \pm \sqrt{S^2 + 4G}}{2G}} \tag{3-9}
$$

Thus, for a given strip speed, the non-dimensional film thickness, W, and the corresponding maximum non-dimensional withdrawal flux, Q_{max}, would be a feature of dp/dx and τ at any coordinate of x. According to Elsaadawy et al. [16], once the coating is solidified, the coating will have the same velocity as strip velocity, V_s, and therefore, the final coating thickness, w_∞, is given by:

$$\boldsymbol{w_\infty = \frac{q}{V_s} = \frac{Q}{\sqrt{\frac{\rho g}{\mu V_s}}}} \tag{3-10}$$

The final coating weight, cw_∞, is determined by multiplying the coating thickness (w_∞) with the density of the liquid zinc (ρ).

$$\boldsymbol{cw_\infty = w_\infty * \rho} \tag{3-11}$$

It becomes clear that the coating weight at any given coordinate of x, for a particular line speed will depend on the pressure gradient (dp/dx) and the shear stress (τ). Therefore, it becomes essential to have associations for pressure and shear stress exerted by air knives depending on the experimental findings. In the following sections, different correlations developed by various researchers are discussed.

3-3-1 Pressure Correlations

In the literature, different studies performed by various authors suggest that pressure distribution is a function of the distance along the strip. Moreover, two separate pressure distribution models are considered based on the ratio of the strip-to-knife distance, Z, and the nozzle gap, d. As seen in Figure 3-5, the air-knife with nozzle gap, d, is positioned perpendicular to the steel strip, at a distance Z from the strip.

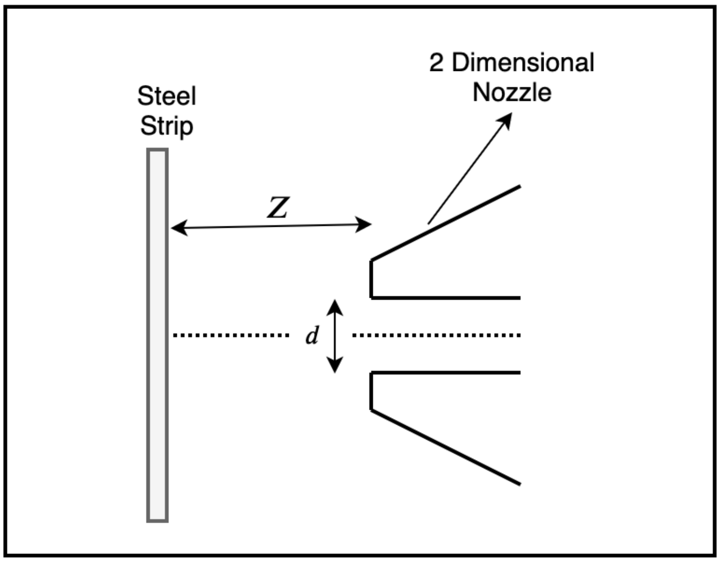

Figure 3-5: Schematic of two dimensional nozzle and steel strip

Case 1 : $\frac{Z}{d} \leq 8$

Elsaadawy et al. [16], developed correlations that best reflect the pressure distribution in the jet's near field region, where the strip-to-knife distance, Z, and nozzle gap, d, ratio is less than or equivalent to eight ($Z/d \leq 8$). The model developed to fit the data of the surface pressure of the air-knife is given by:

$$\frac{p}{p_m} = \left[1 + 0.6\xi_p^4\right]^{-1.5} \tag{3-12}$$

where p_m is the peak/maximum pressure (where x = 0), $\xi_p = x/b_p$ is the dimensionless distance and $b_p = x$ is the point where $p = p_m/2$, i.e., half width of pressure distribution, given by the expression:

$$\frac{b_p}{d} = 0.0453\left(\frac{Z}{d}\right) + 0.7921 \tag{3-13}$$

where Z is the distance from air-knife to the steel strip and d is the air-knife gap width as shown in Figure 3-5. Correlation for the pressure gradient is found by differentiating Equation 3-12:

$$\frac{d}{d\xi_p}\left(\frac{p}{p_m}\right) = -3.6\xi_p^3\left[1 + 0.6\xi_p^4\right]^{-2.5} \tag{3-14}$$

It is also important to have a correlation between the maximum pressure, p_m, and the chamber pressure or so called the wiping pressure of air-knife, P_0. Based on the experimental results, the following correlation was developed by Elsaadawy et al. [16]:

$$\frac{p_m}{P_0} = -0.0056\left(\frac{Z}{d}\right)^2 + 0.0268\left(\frac{Z}{d}\right) + 1.0108 \tag{3-15}$$

Figure 3-6 illustrates a typical pressure profile produced by the air-knife on the zinc coating for the case when $\frac{Z}{d} \leq 8$.

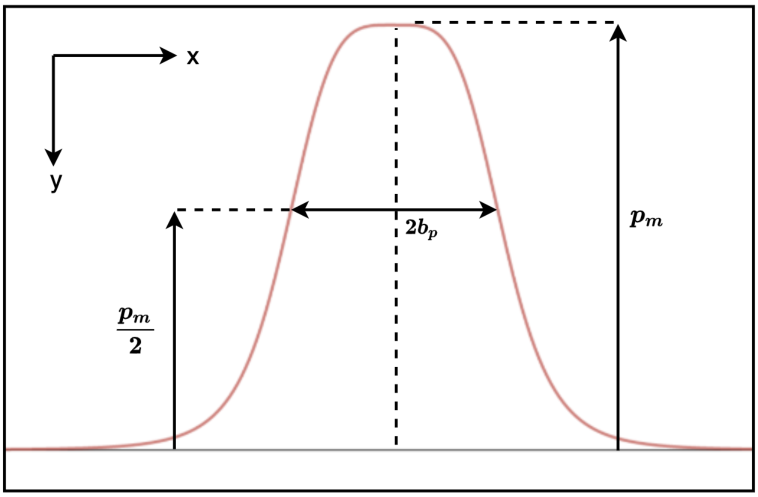

Figure 3-6: Typical air-knife pressure distribution for $Z/d \leq 8$

Case 2 : $\frac{Z}{d} > 8$

Ellen and Tu [15] developed correlations for the jet's imposed pressure based on experimental measurements such that

$$\frac{p}{p_m} = e^{-0.693\xi^2} \tag{3-16}$$

where p_m is the peak pressure (where x = 0), $\xi = x/b_p$ is the dimensionless distance and $b_p = x$ is the point where $p = p_m/2$, i.e., half width of pressure distribution, given by the expression:

$$\frac{b_p}{d} = 0.0019\left[\frac{Z}{d}\right]^2 + 0.0551\left[\frac{Z}{d}\right] + 0.4035 \tag{3-17}$$

where Z is the distance from air-knife to the steel strip and d is the air-knife gap width as shown in Figure 3-5. It has been found that using the above mentioned correlations, model estimates accurate values of coating weight for large strip-to-knife distance, Z/d > 8. Figure 3-7 illustrates a typical pressure profile produced by the air-knife on the zinc coating for the case when $\frac{Z}{d} > 8$.

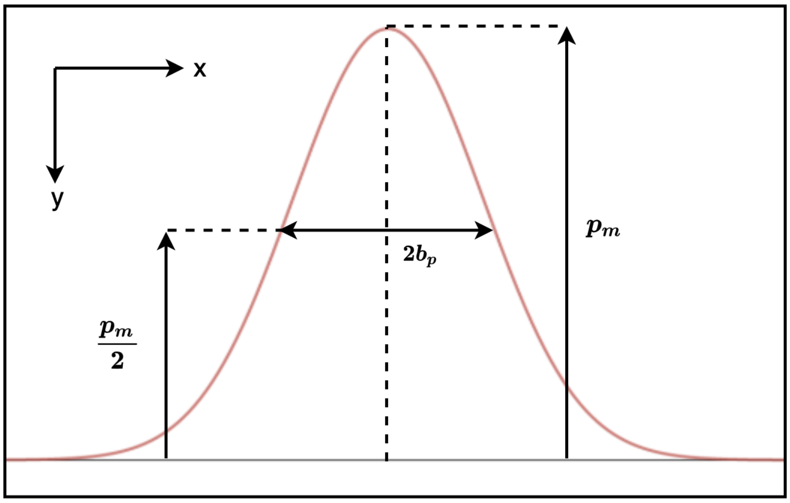

Figure 3-7: Typical air-knife pressure distribution for $Z/d > 8$

3-3-2 Shear Stress Correlations

Similar to the pressure distribution, two different shear stress models are considered based on the ratio of the strip-to-knife distance, Z, and the nozzle gap, d.

Case 1 : $\frac{Z}{d} \leq 8$

The model developed to fit the data which correlates dimensionless shear stress with dimensionless distance ξ_τ is given by [16],

$$\left.\begin{aligned} \frac{\tau}{\tau_{\max}} &= \operatorname{erf}\left(0.41\xi_\tau\right) + 0.54\xi_\tau e^{-0.22\xi_\tau^3}, && \text{for } 0 \leq \xi_\tau \leq 1.73 \\ \frac{\tau}{\tau_{\max}} &= 1.115 - 0.24\ln\left(\xi_\tau\right), && \text{for } \xi_\tau > 1.73 \end{aligned}\right\} \tag{3-18}$$

where τ_{max} is maximum shear stress, $\xi_\tau = x/b_\tau$ is the dimensionless distance and $b_\tau = x$ is the location of maximum shear stress, given by the expression:

$$\frac{b_\tau}{d} = 0.0443\left(\frac{Z}{d}\right) + 1.1687 \tag{3-19}$$

where Z is the distance from air-knife to the steel strip and d is the air-knife gap width as shown in Figure 3-5. Similar to the pressure case, a correlation between the maximum shear stress (τ_{max}) and the wiping gas pressure (P_0) was developed using the experimental results and is given by [16]:

$$\frac{\tau_{\max}}{P_0} = -0.0001\left(\frac{Z}{d}\right) + 0.0035 \tag{3-20}$$

Figure 3-8 illustrates a typical shear stress distribution produced by the air-knife on the zinc coating for the case when $\frac{Z}{d} \leq 8$.

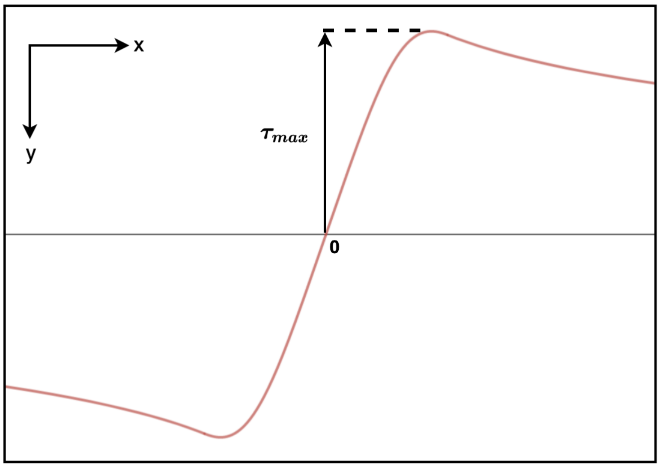

Figure 3-8: Typical shear stress distribution for $Z/d \leq 8$

Case 2 : $\frac{Z}{d} > 8$

Ellen and Tu [15] developed a model depicting shear stress imposed by the jet based on experimental measurements such that

$$\frac{\tau}{\tau_{max}} = \text{erf}\left(0.833\xi\right) - 0.2\xi e^{-0.693\xi^2} \tag{3-21}$$

where τ_{max} is maximum shear stress, $\xi = x/b_\tau$ is the dimensionless distance and $b_\tau = x$ is the location of maximum shear stress, given by the expression:

$$\frac{b_\tau}{d} = 0.0019\left[\frac{Z}{d}\right]^2 + 0.0551\left[\frac{Z}{d}\right] + 0.4035 \tag{3-22}$$

where Z is the distance from air-knife to the steel strip and d is the air-knife gap width as shown in Figure 3-5. Shear stress profile produced by the air-knife on the zinc coating for the case when $\frac{Z}{d} > 8$ is shown in Figure 3-9.

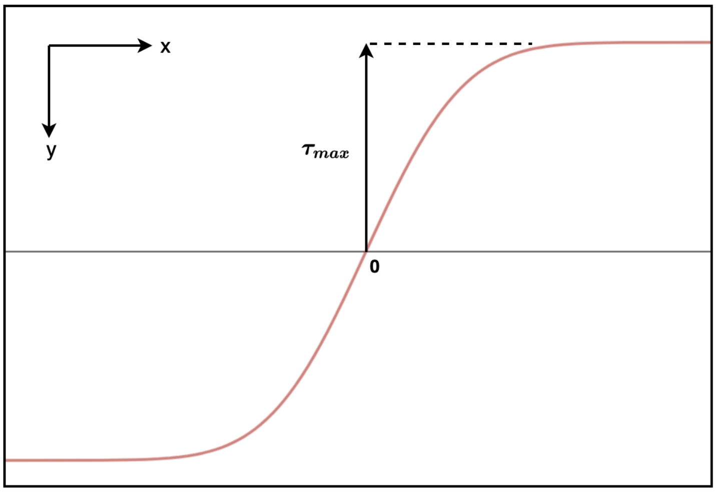

Figure 3-9: Typical shear stress distribution for $Z/d > 8$

3-4 Summary

Focusing on the coating weight model defined in Section 3-3, the coating weight can be calculated quantitatively and independently using the first principle by the effect of the three most influencing factors, i.e., the strip speed (V_s), the wiping gas pressure from the air-knife (P_0) and the strip-to-knife distance (Z). It is important to note that the air-knife jet opening (d) can not be actuated, and in general, it is pre-tuned with the air-knife setup, as discussed in Subsection 3-1-3.

For the air-knife to wipe the zinc coating in the hot-dip galvanizing process, few correlations were represented to describe the pressure (Subsection 3-3-1) and shear stress (Subsection 3-3-2) profiles as functions of strip-to-knife distance (Z) and air-knife jet opening (d) in the near-field air-knife region. Also, the peak pressure (p_m) and the maximum shear stress (τ_{max}) are directly influenced by the wiping gas pressure (P_0) of the air-knives as shown in Equation 3-15 and Equation 3-20 respectively.

This model assumes that the fan's dynamics resulting in the wiping gas pressure are very fast, and instantaneous pressure is generated, but that might not be the case in reality. Therefore, depending on the fan's dynamics, it could be concluded that the process is either static or dynamic.

Chapter 4

System Identification

4-1 Introduction

System identification methods are systematic methods that are used to build mathematical models based on the measured data and prior knowledge of the system for a specific process [27]. Generally speaking, system identification involves three main steps: data acquisition, model structure selection and parameters estimation, and model validation.

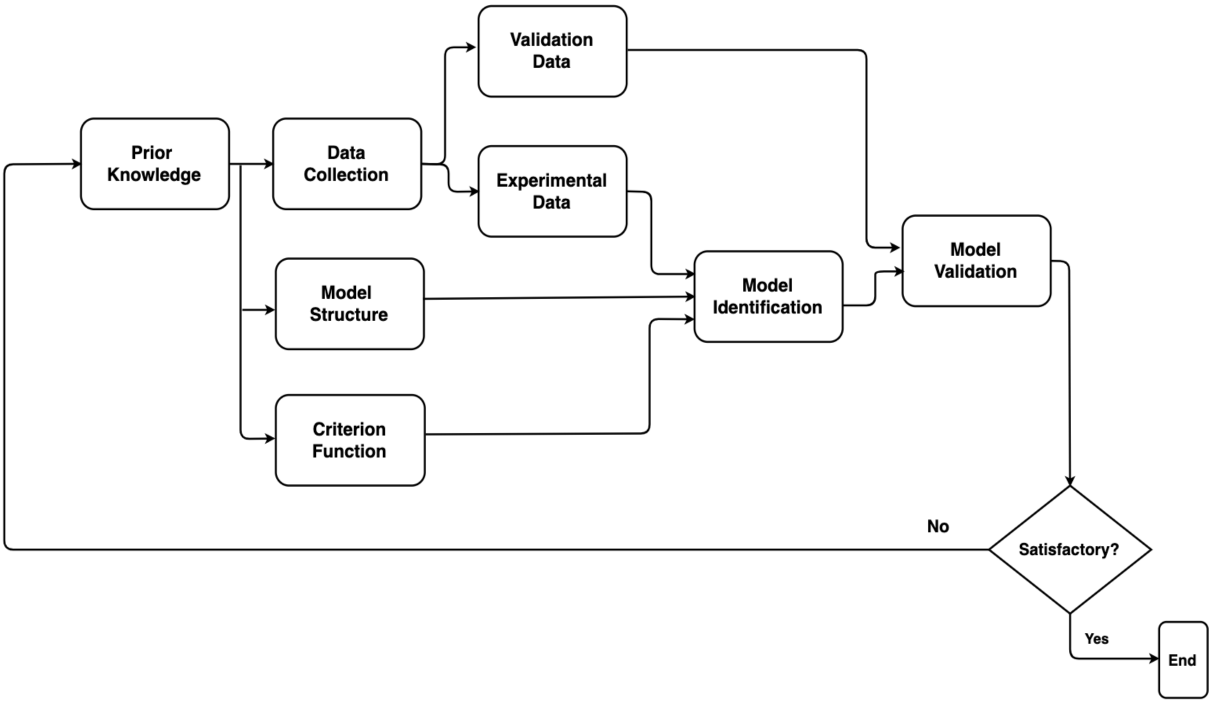

Figure 4-1: System identification loop, adapted from [27]

The data is most commonly obtained based on previous understanding of the process and modeling objectives. Without a doubt, the choice of model configuration is the most critical step in the identification framework. A logical move is to focus the model on physical laws and specific relationships with the relevant physical parameters. Nevertheless, if one of these parameters is uncertain or not specified, realistic estimates need to be made; for example, the parameters may be estimated from the data. Model sets with these customizable parameters are called grey-box models [24].

To calculate the fit between model performance and measurement data, a criterion function must be defined, and an identification technique must be selected to solve the problem of parameter estimation. Finally, a model validation step takes into account the concern if the model is valid and accurate enough for its intended usage. The system identification method to create a suitable mathematical model for a particular process is described in Figure 4-1.

At other times, when no essential information about the system is available a priori, black-box models are generally used. They become beneficial when the main emphasis is on fitting data regardless of the process knowledge. The model structures vary in complexity based on the flexibility to take into account the system's dynamics. Typically, simple linear model structures are tested first and later on advanced to more complex structures.

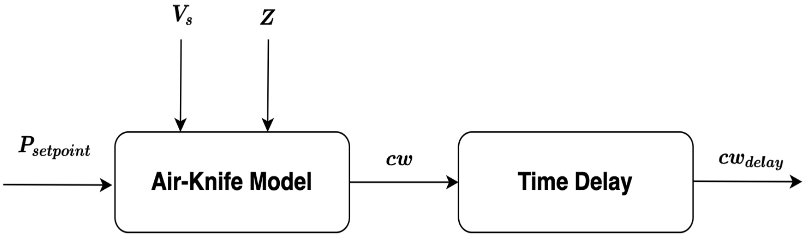

Figure 4-2: Overview of air-knife wiping process

In the first place, it is crucial to have an overview of the entire air-knife wiping process, as shown in Figure 4-2. The input to the air-knife setup is known as $\boldsymbol{P_{setpoint}}$, which experiences some dynamics due to the fan. The resulting output from the fan dynamics is called the air-knife wiping pressure $\boldsymbol{P_0}$. The static coating weight model described in Chapter 3 was developed using the first principle modeling. The entire operational range of the coating process shows the non-linear dependency of the coating weight on three main process variables:

- Wiping gas pressure, $\boldsymbol{P_0}$
- Strip Speed, $\boldsymbol{V_s}$
- Strip-to-knife distance, $\boldsymbol{Z}$

Since the cold coating gauge is located at a significant distance from the air-knives, there exists a time delay before the coating weight is actually measured. For system identification, it is essential to realize that the signals available from the production data are the control input $P_{setpoint}$, the air-knife wiping pressure P_0, the strip speed V_s, strip-to-knife distance Z, and the measured coating weight (after the time delay) cw_{delay}.

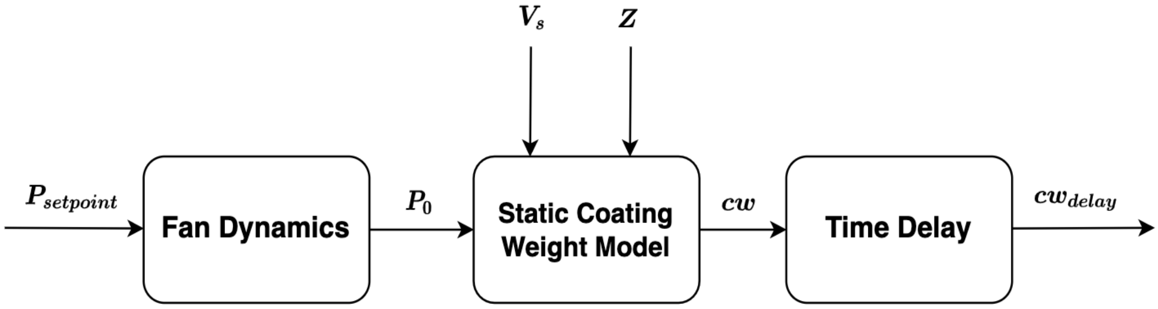

Figure 4-3: Simplified block representation of air-knife wiping process

With the simplified block representation of the air-knife wiping process (Figure 4-3), the system identification can be considered in three different sections. In the first part, the measured data of the control input $P_{setpoint}$ and the air-knife wiping pressure P_0 are used to identify the fan's dynamics.

Since the galvanizing process is highly complex and non-linear with different process variables affecting the final coating weight [6, 36, 42], many authors during the last few years have developed models based on regression analysis [3, 19, 42], which are simple exponential models whose parameters are tuned based on the input and output data. Regression models are easy to realize, but the ability to generalize concerning non-linear behavior of the system is poor [30, 36].

For the second part, the mathematical model structure of the coating weight process is already known from prior knowledge of the system. Therefore, it can be appropriately parameterized with some unknown coefficients, which define an additional set of system parameters. The next step, after having a suitable parametrized model is concerned with the estimation of the unknown parameters from the given input-output data set. However, the only available measurements for the output coating weight is after the time delay. As a result, a time delay model is identified in the third part that uses the knowledge of the strip speed to determine the delay-free coating weight values (cw) i.e., at the location immediately after the air-knives.

In this Chapter, system identification will be performed for the first two components, i.e., the fan dynamics and the static non-linear coating weight model. The time delay model is discussed separately in Chapter 5. The result obtained from the static coating weight model will be compared with the existing power-law model developed by Tata Steel Europe.

4-2 Identification of Fan Dynamics

Despite the importance of continuous hot-dip galvanizing process, the literature fails to provide the dynamics of fan in the air-knives. Therefore, a comprehensive technique is described in this section to develop a reliable model of fan dynamics.

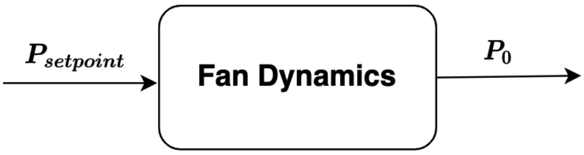

Figure 4-4: Transfer function model for fan dynamics

The so-called system identification is to approximate the input-output data with a transfer function model. The transfer function is defined as the ratio of Laplace transform of output to Laplace transform of input. The input signal to the fan is the control input $P_{setpoint}$, and the output is the air-knife wiping pressure P_0. With the objective to estimate the transfer function, it seems logical to use step response data [26].

4-2-1 Data Preparation

An ideal model for the fan dynamics must work equally well for the entire operating range of the process. However, in the production data from a running galvanizing line, it isn't easy to find a dataset with a pure step input ($P_{setpoint}$) and that too for different operating ranges. One possible dataset available to analyze the step response of the fan dynamics is shown in Figure 4-5. As described in Subsection 3-1-3, there are two identical air-knives (top and bottom) placed parallel to each other, and their response's to step input are plotted in Figure 4-5.

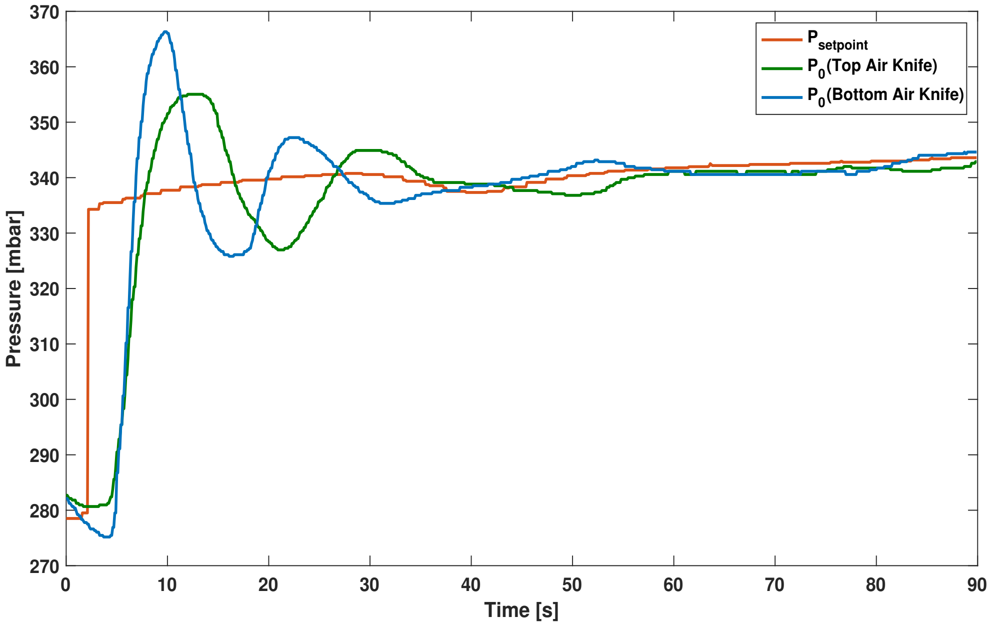

Figure 4-5: Step response for fan dynamics

It can be seen that the top and bottom air-knives behave differently, and at $t = 22s$, they are in completely opposite phases. Therefore, there is a need to find another dataset where both the air-knives perform identically such that their data can be used for identification. One such dataset is available when the galvanizing line is not operational, but the air-knives are actuated unrestrictedly. The response of both the air-knives to step input in such a case is illustrated in Figure 4-6. For the identification purpose, the step response of the top air-knife is used.

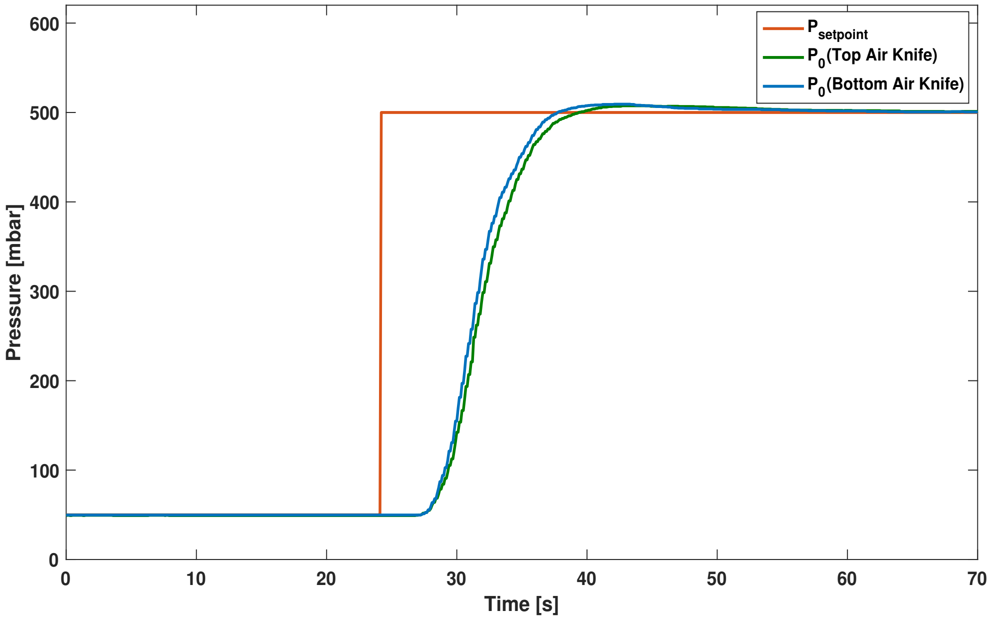

Figure 4-6: Pure step response for fan dynamics

4-2-2 Estimating Transfer Function

This section considers system identification based on the step response, as determining the time constant, and the time delay is simple. A step input of amplitude 450 mbar is applied at $t = 24.1s$ in the dataset mentioned above.

To determine which order of approximation best fits the step response, *tfest* function in MATLAB is used to estimate the transfer function for different model orders. Table 4-1 and Table 4-2 indicate the percentage fit and the Root Mean Square Error (RMSE) for different model orders in the identification and validation data set respectively.

The percentage fit indicates how well the model response matches the measured data and it is calculated using normalized root mean square squared error [28].

$$\text{fit} = 100 * \left(1 - \frac{\|y - \widehat{y}\|}{\|y - \text{mean}(y)\|}\right) \tag{4-1}$$

where y is the measurement data and $\widehat{y}$ is model output.

Table 4-1: Comparison of different order approximations for the Fan Dynamics - Percentage Fit

Model Order	Fit - Identification Data	Fit - Validation Data
First Order	90.59%	89.24%
Second Order	96.92%	96.79%
Third Order	96.92%	96.76%
Fourth Order	94.1%	94.1%

Table 4-2: Comparison of different order approximations for the Fan Dynamics - RMSE

Model Order	RMSE - Identification Data	RMSE - Validation Data
First Order	15.88 mbar	18.22 mbar
Second Order	4.65 mbar	6.19 mbar
Third Order	4.67 mbar	6.24 mbar
Fourth Order	10.95 mbar	11.18 mbar

The Root Mean Square Error (RMSE) for both the identification and validation data set is calculated using the formula given by Equation 4-2.

$$\text{RMSE} = \sqrt{\sum_{i=1}^{n} \frac{(y_i - \hat{y_i})^2}{n}} \tag{4-2}$$

where n is the number of data points, y_1, y_2,..,y_n are measured values and $\hat{y_1}$, $\hat{y_2}$,..,$\hat{y_n}$ are predicted values.

Looking at Table 4-1 and Table 4-2, it can be clearly seen that the transfer function estimated with the second order dynamics matches the best with the measurement data. Therefore, in this section, the parameters are estimated for a general second order approximation given by the equation Equation 4-3.

$$\tau_s^2 \frac{d^2y}{dt^2} + 2\zeta\tau_s \frac{dy}{dt} + y = K_p u\left(t - \theta_p\right) \tag{4-3}$$

where $y(t)$ is the output (air-knife wiping pressure, P_0), $u(t)$ is the input (pressure setpoint, $P_{setpoint}$), K_p is the system gain, ζ is called damping factor, τ_s is the second-order time constant and θ_p is the time delay. In Laplace domain, second order system can be described by:

$$\frac{Y(s)}{U(s)} = \frac{K_p}{\tau_s^2 s^2 + 2\zeta\tau_s s + 1} e^{-\theta_p s} \tag{4-4}$$

The following procedure is used to obtain graphical approximation of a step response for an under-damped (oscillating) second order system ($0 \leq \zeta < 1$):

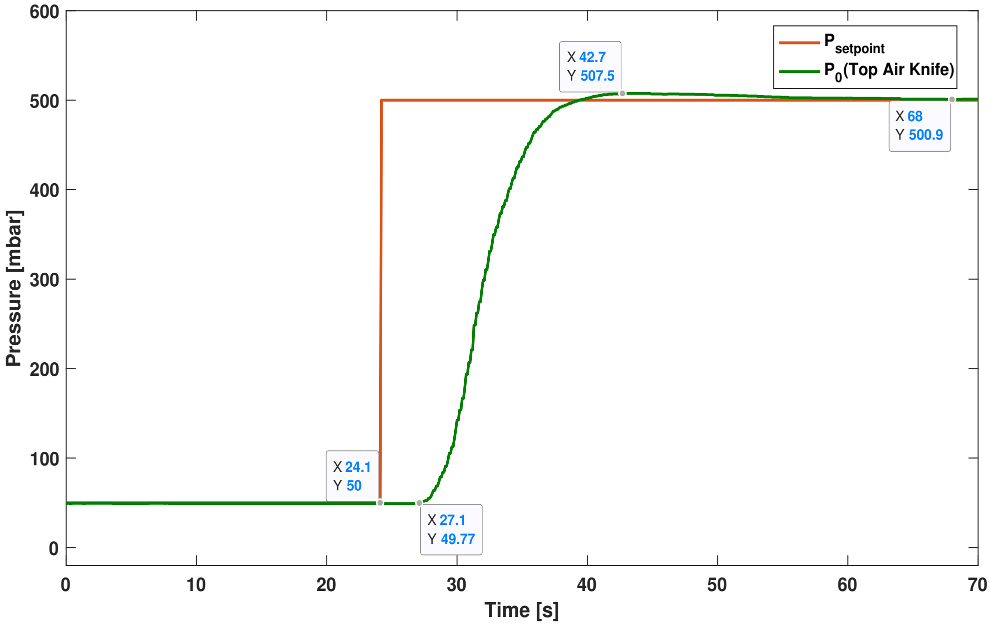

Figure 4-7: Estimation of second order system from the Step Response

- **Delay Time θ_p**: The effect of the step input is observed after θ_p =27.1s - 24.1s= $3s$
- **Peak Time t_p**: The amount of time to reach the first peak (after accounting for time delay), $t_p = 42.7s - 27.1s = 15.6s$
- **Overshoot Ratio (OS)**: The amount that the first oscillation exceeds the steady state compared to the steady state change.

$$OS = \frac{y(t_p) - y(\infty)}{y(\infty)}$$
$$OS = \frac{507.5 - 500.9}{500.9} = 0.01312$$

- **Damping Ratio ζ**: It is the mathematical means of expressing the level of damping in a system relative to critical damping.

$$\zeta = \sqrt{\frac{(\ln(OS))^2}{(\ln(OS))^2 + \pi^2}} = 0.8$$

- **Time Constant τ_s**: The time constant for a second order process is given by:

$$\tau_s = \frac{\sqrt{1-\zeta^2}}{\pi} t_p = 2.96s$$

- **Rise Time t_r**: The amount of time to cross the steady state value (after accounting for time delay).

$$t_r = \frac{\tau_s}{\sqrt{1-\zeta^2}} \left(\pi - \cos^{-1}\zeta\right) = 12.3s$$

- **System Gain K_p**: The system gain is the change in the output y induced by the change in the input u.

$$K_p = \frac{\Delta y}{\Delta u} = \frac{500.6 - 49.77}{500 - 50} = 1.0018$$

After obtaining all the parameters, they are substituted in second order system transfer function given in Equation 4-4.

$$\text{T.F.} = \frac{1.0018}{8.7616s^2 + 4.736s + 1} e^{-3s} \tag{4-5}$$

$$\boxed{\text{T.F.} = \frac{\mathbf{0.1142}}{\boldsymbol{s^2 + 0.5405s + 0.1141}} \boldsymbol{e^{-3s}}} \tag{4-6}$$

The percentage fit between the measured output pressure P_0, and estimated model output pressure is 97.15%. It indicates how well the response of this transfer function matches the measured data. It is calculated using the formula given by Equation 4-1. Figure 4-8 illustrates the match between the measurement data and the model output. The estimated model needs to validated against a validation data set. However, there is no other different size of step input ($P_{setpoint}$) available from the production data. Therefore, a different data set with the same step size of 450 mbar is used to validate the model. The match between the measured output and the model output for the validation set is illustrated in Figure 4-9. The percentage fit between the measured output pressure P_0, and estimated model output pressure is 96.3%.

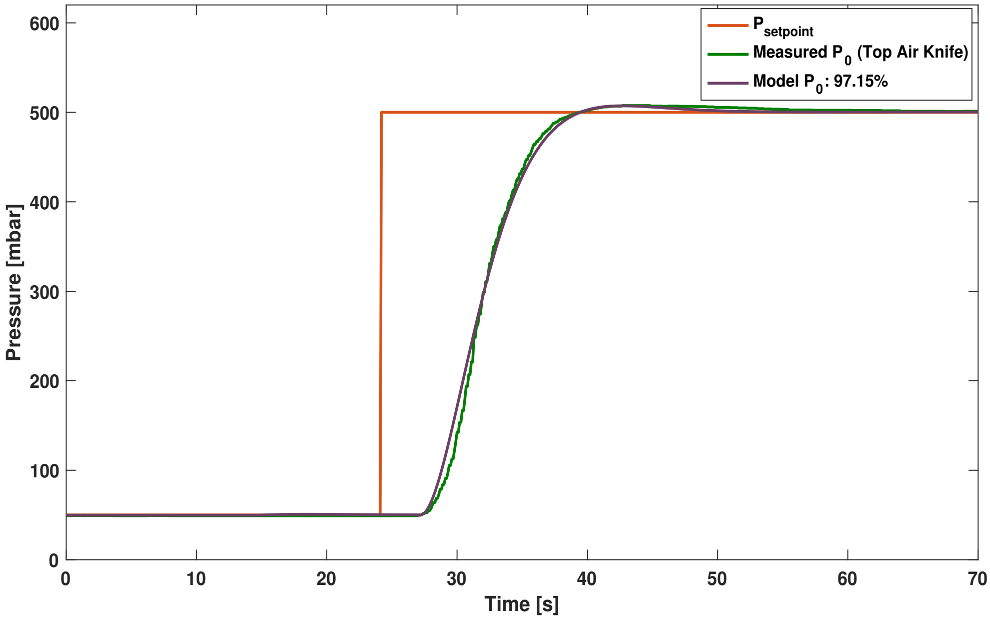

Figure 4-8: Comparing measured pressure and estimated model pressure for identification dataset

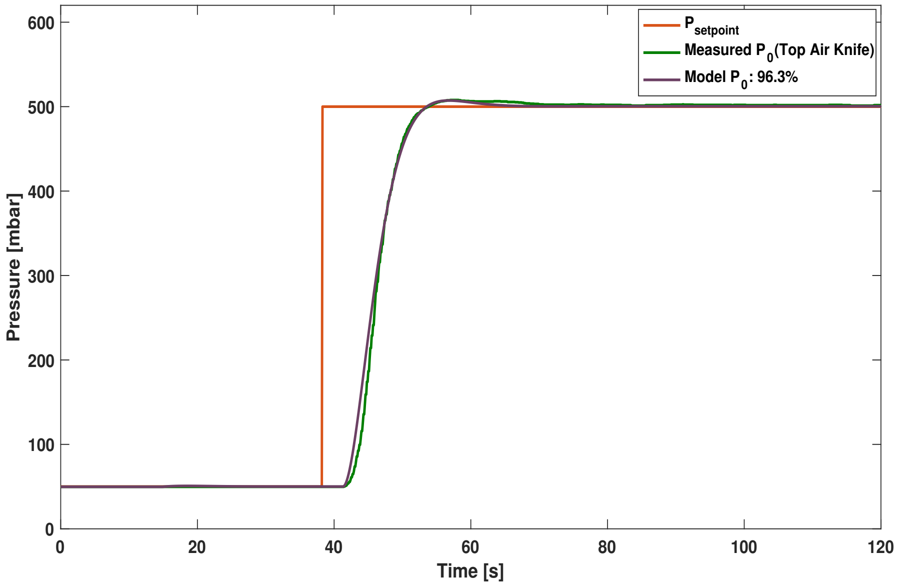

Figure 4-9: Comparing measured pressure and estimated model pressure for validation data-set

4-3 Identification of Static Coating Weight Model

Once the fan's dynamics are derived independently, the next step is to identify the static part of the coating weight model, which was developed using first principles, as discussed in Section 3-3. The coating weight in the galvanizing process is mainly affected by air-knife wiping pressure (P_0), line speed (V_s), and strip-to-knife distance (Z). In this section, a detailed procedure to form a reliable static wiping model is described. The first step in system identification is to collect the correct input-output data.

The cold coating gauge is installed at a significant distance from the air-knives. As a result, the only coating weight measurements (cw_{delay}) available are recorded after a certain time delay. In order to match the coating weight measurements with the impact factor of the other process variables, the measured coating weight values are traced back in time with the calculated time delay according to the formulation discussed in Section 5-4. Finally, all the input and output signals are available for system identification.

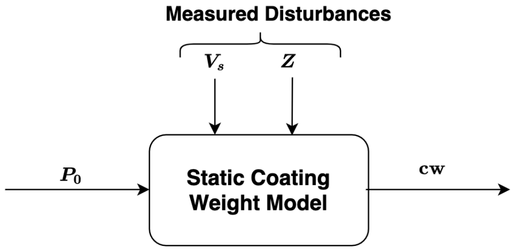

Figure 4-10: Static coating weight model

4-3-1 Data Preparation

The production data between March 2019 and January 2020 at Hot Dip Galvanizing Line 1 (HDGL1) is used to identify the parameters in the coating weight prediction model and validate the same. There are two air-knife sets (set 3 and set 4) currently being deployed at HDGL1. Both the air-knives have slightly different wiping behavior, and therefore, the production data for both the knives are separated. Furthermore, Tata Steel uses two types of zinc coatings for commercial products: Conventional galvanized coating (GI) and MagiZinc coating (MZ).

GI coating has been used in the steel industry for decades and is still a popular choice for providing sacrificial protection for steel components. In the past few decades, the automotive industry has been prioritizing weight reduction in order to reduce fuel consumption and carbon dioxide emission. Therefore, in 2005 Tata Steel introduced MZ coating, which was found to have better corrosion-resistant properties, especially for the lower coating weight specifications. Due to significant chemical and physical property differences between GI and MZ coating, the data for both the coatings are separated. Ultimately, this thesis aims to investigate the production data for the air-knife set 3 and GI coating only and develop the coating weight model for the same. The coating weight prediction model must ideally be able to work equally well for the entire operating range, as shown in Table 4-3. However, not all process conditions occur uniformly in the actual galvanizing line. For example, it can be seen in the data that for HDGL1 more than 50% of the coils are produced with 50 g/m^2 or 60 g/m^2 of coating weight on either side of the steel strip. Therefore, when using such production data to identify the model, it will be more biased towards the process variables that occur more often. Hence it becomes essential to represent the data in such a way that it allows equal weight to each different process condition.

Table 4-3: Operating range of different process variables

Process Variables	Minimum Value	Maximum Value
Wiping Gas Pressure (P_0)	0 [Pascal]	60000 [Pascal]
Line Speed (V_s)	1 [m/s]	2.5 [m/s]
Strip-to-Knife Distance (Z)	10 [mm]	25 [mm]
Coating Weight	45 [g/m^2]	180 [g/m^2]

In order to achieve appropriate data for identification, it is preprocessed as follows:

- Remove inaccurate data: If one of the two gauges (top and bottom) is not active, the coating weight value registered in the database is the target value instead of the measured value. Hence, this portion of data must be removed by checking if anyone of the gauge is not active.

- Remove unreliable data: When two different coils are welded together, the coating gauge doesn't give correct measurements for the zinc coating weight at that point. Hence, these data points must be removed for identification.

- Remove redundant data: In the production data, there is a possibility of running into a similar kind of data for each process variable. In order to keep the prediction model equally biased for the entire operating range, identical data must be removed.

- Grouping and Averaging: As discussed in Subsection 3-1-4, the coating gauge scans back and forth across the moving strip forming the zig-zag path, as shown in Figure 3-3. The most reliable coating weight measurement available in the database is the average coating weight over the length of each scan. Finally, the average coating weight is then grouped on the rest three parameters: air-knife wiping pressure (P_0), strip-to-knife distance (Z), and strip speed (V_s). Production data used to generate new fitting parameters in the model is shown in Figure 4-11. It can be seen that all the process variables have covered the complete process range (Table 4-3).

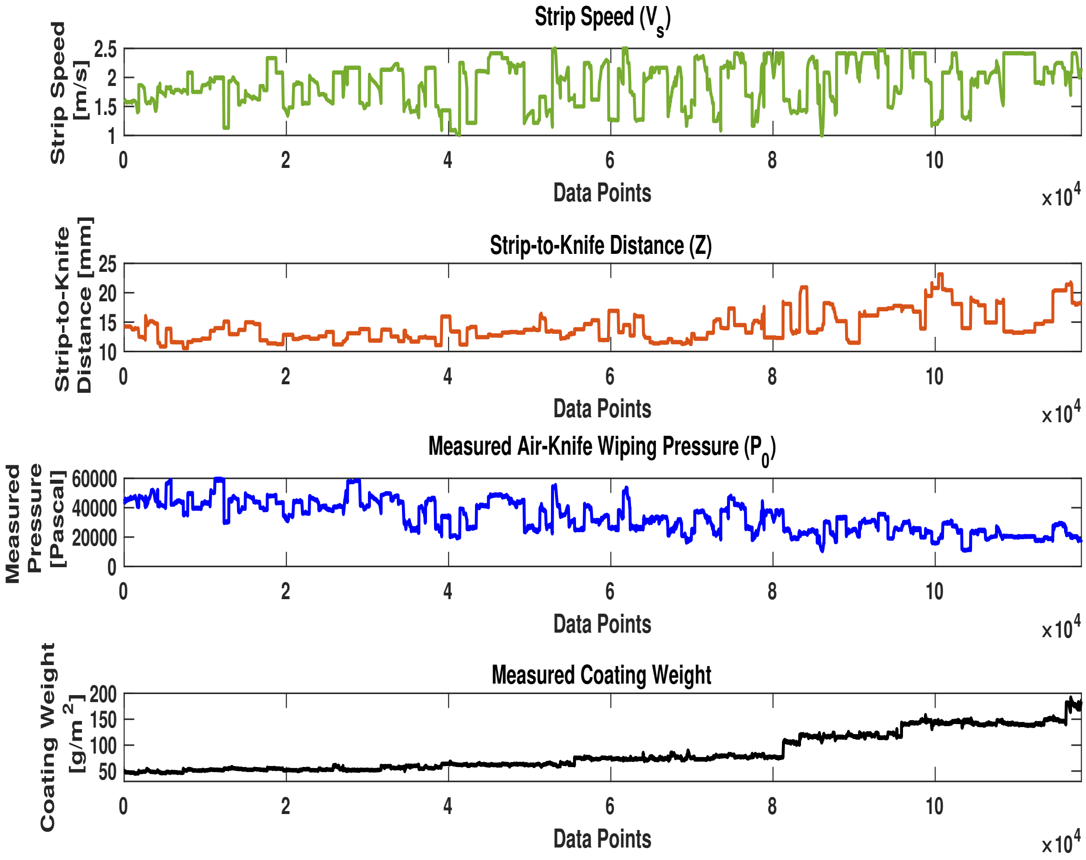

Figure 4-11: Experimental data for identification

4-3-2 Pressure Correlations

The first principle coating weight model described in Section 3-3 consists of pressure and shear stress correlations that were developed by various researchers using the experimental results. These correlations vary for different air-knife setups depending on their internal piping structure and the blower used. Therefore, in this section, the existing relationships will be appropriately parameterized and based on the pressure distribution measurements, the new fitting parameters will be determined.

In order to realize pressure distribution measurements, various experiments were performed by Tata Steel using an air-knife with a nozzle opening, d, of 1 mm that supplied air on one side of the strip by means of a blowing device. As seen in Figure 3-5, the air-knife was placed perpendicular to the strip at a distance Z from the strip. The strip was a aluminum rectangular plate positioned on a manual traverse that had the capability to move in all directions.

The air-knife was held constant, and the strip was moved for all the experiments. The pressure measurements were taken by a pressure transducer fitted behind a 0.5 mm hole in the plate. The pressure profiles, $p(x)$, were evaluated for strip-to-knife distances of Z = 10, 12, 14, 16, 18, 20, 22, and 24 mm and air-knife wiping pressure P_0 = 100, 150, 200 and 500 mbar. The pressure profiles along the strip, $p(x)$ were measured in the range of 6 mm from the center in an interval of ± 0.01 mm such that $x = \pm$ 0.01, 0.02, ..., 6 mm. For a strip-to-knife distance, Z = 10 mm, the pressure profiles corresponding to various wiping pressures (P_0) is plotted in Figure 4-12.

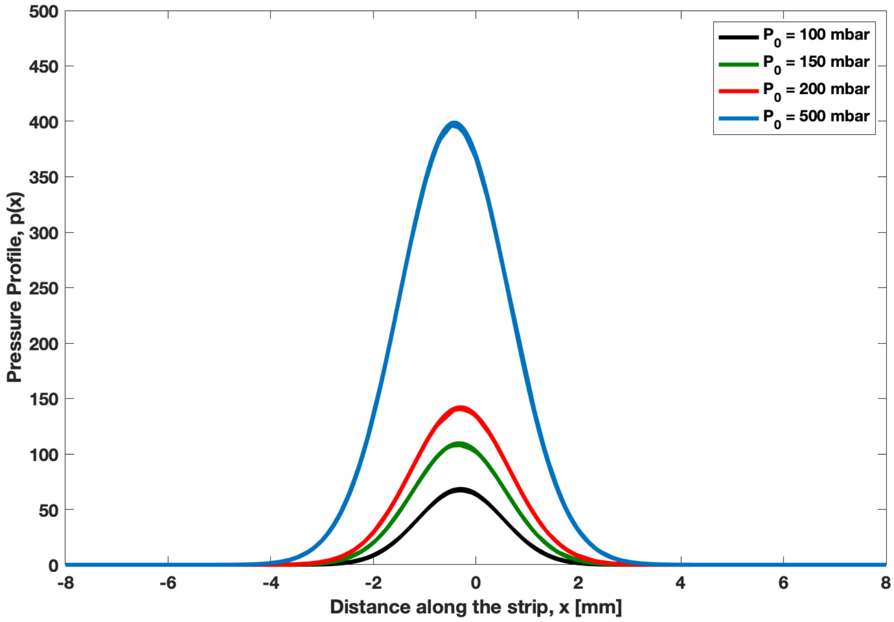

Figure 4-12: Experimental pressure distribution along center of the strip for Z = 10 mm

From the production data shown in Figure 4-11, it is clear that the ratio of strip-to-knife distance, Z to nozzle gap, $d = 1$ mm, is greater than 8. Therefore, pressure correlations developed by Ellen and Tu [15], must be used to parameterize the pressure profiles as given by Equation 4-7 and Equation 4-8.

$$\frac{p_m}{P_0} = p1\,(Z)^2 + p2\,(Z) + p3 \tag{4-7}$$

$$b_p = p4\,(Z)^2 + p5\,(Z) + p6 \tag{4-8}$$

where P_0 is the air-knife wiping pressure, p_m is the peak pressure, $b_p = x$ is the point where $p = p_m/2$, i.e., half width of pressure distribution, and Z is the distance from air knife to the steel strip. $p1$, $p2$, $p3$, $p4$, $p5$ and $p6$ are the six parameters that need to be identified using the pressure distribution measurements. It is important to note that the air-knife nozzle gap, d, has been substituted equal to 1 mm in the above equations.

Based on the experimental pressure distribution data, the ratio of the maximum pressure (p_m) to the air-knife wiping pressure (P_0) is plotted against the impingement distance (Z) in the Figure 4-13. According to the literature, the pressure ratio must be a function of strip-to-knife distance. However, in Figure 4-13, it can be seen that the pressure ratio not only depends on the strip-to-knife distance but also on the air-knife wiping pressure (P_0).

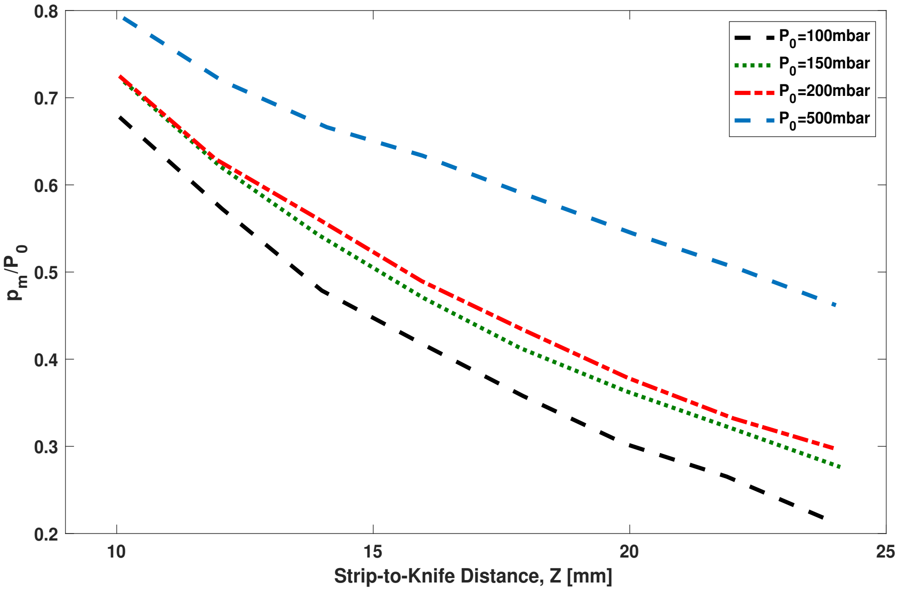

Figure 4-13: Correlation of the pressure ratio ($\frac{p_m}{P_0}$) with strip-to-knife distance (Z)

To begin with, the pressure ratio (p_m/P_0) and the strip-to-knife distance (Z) were fitted to the polynomial given by Equation 4-7 for all the independent air-knife wiping pressures. Four different polynomial fits were achieved as shown in figure Figure 4-14.

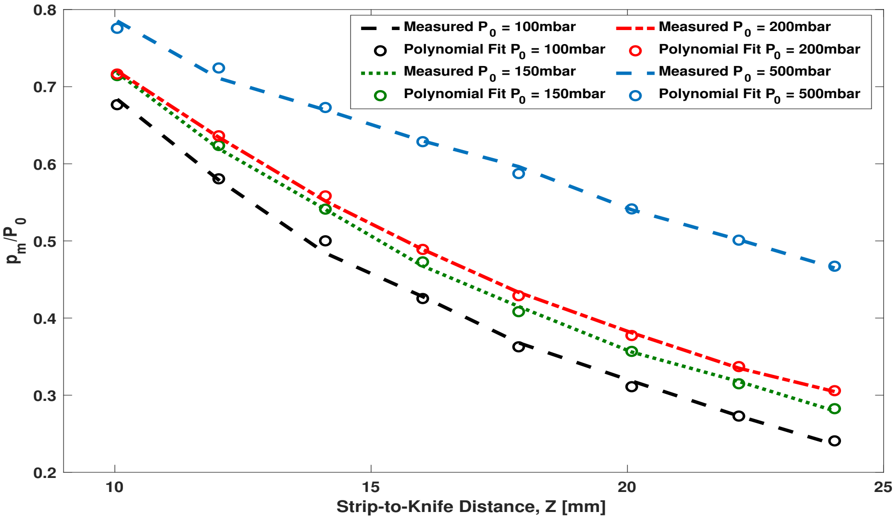

Figure 4-14: Fit of the pressure ratio ($\frac{p_m}{P_0}$) with strip-to-knife distance (Z)

In the next step, the estimated parameters corresponding to different wiping pressures were investigated to see if there was any kind of relation between them. It was interesting to find out that these parameters $p1$, $p2$ and $p3$ can be approximated with a linear dependence on the air-knife wiping pressure (P_0). The three parameters for different wiping pressures are plotted in Figure 4-15. The solid line in the figure illustrates the estimated parameters from the fit obtained in Figure 4-14. The dotted line in the figure indicates the linear fit of these parameters with respect to wiping pressure.

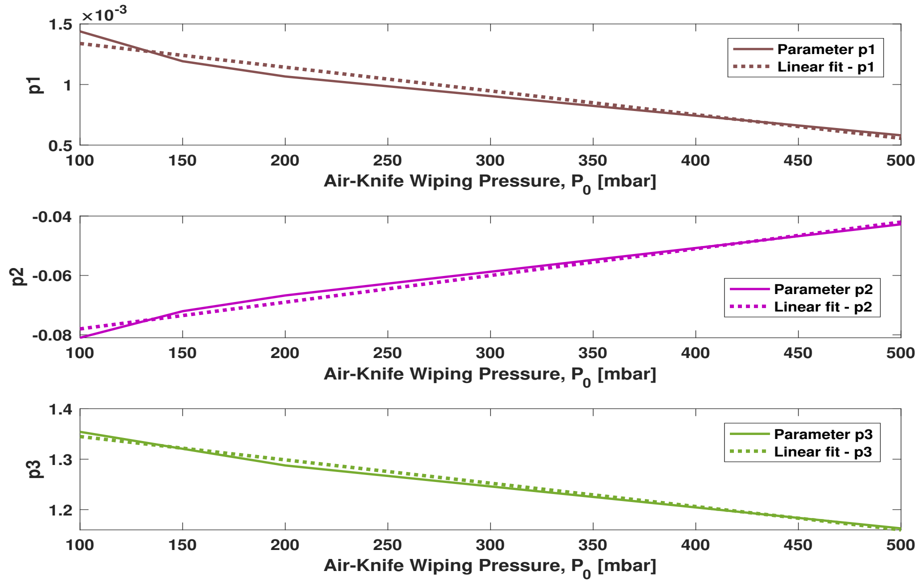

Figure 4-15: Linear fit of the pressure ratio model parameters

Finally, the linear dependence of the parameters $p1$, $p2$ and $p3$ with respect to the air-knife wiping pressure (P_0) is given by Equation 4-9.

$$\begin{aligned} p1 &= -1.9572 \times 10^{-8} P_0 + 0.0015 \\ p2 &= 8.9929 \times 10^{-7} P_0 - 0.0870 \\ p3 &= -4.6233 \times 10^{-6} P_0 + 1.3911 \end{aligned} \tag{4-9}$$

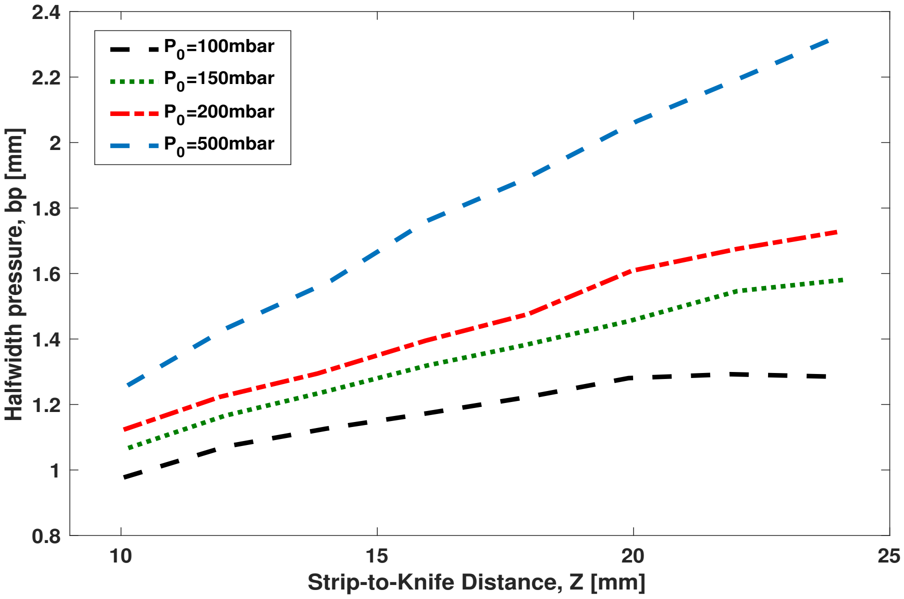

Figure 4-16: Correlation of the half-width of pressure profiles (b_p) with strip-to-knife distance (Z)

Besides the pressure ratio, the half width of pressure distribution (b_p) also needs to be calculated in order to model the complete pressure profile ($p(x)$) given by Equation 3-16. Based on the experimental data, the half width of pressure distribution (b_p) is plotted against the strip-to-knife distance (Z) as shown in Figure 4-16. Analogous to the case of pressure ratio, the half width of pressure distribution is not only a function of strip-to-knife distance (Z) but also of the air-knife wiping pressure (P_0).

In a similar way to that of the pressure ratio, the half width of pressure distribution (b_p) and the strip-to-knife distance (Z) were fitted to the polynomial given by Equation 4-8 for all the independent air-knife wiping pressures. Four different polynomial fits achieved are shown in Figure 4-17.

As a next step, the estimated parameters corresponding to various wiping pressures were studied to see if there is any relation that could be derived from them. Similar to the pressure ratio case, it was found that the parameters $p4$, $p5$ and $p6$ can be approximated with a linear dependence on the air-knife wiping pressure (P_0). Figure 4-18 demonstrates how the three parameters vary with different wiping pressures. The solid line in the figure specifies the estimated parameters that were obtained from the fit in Figure 4-17 and the dotted line indicates the linear fit of these parameters with respect to the wiping pressure.

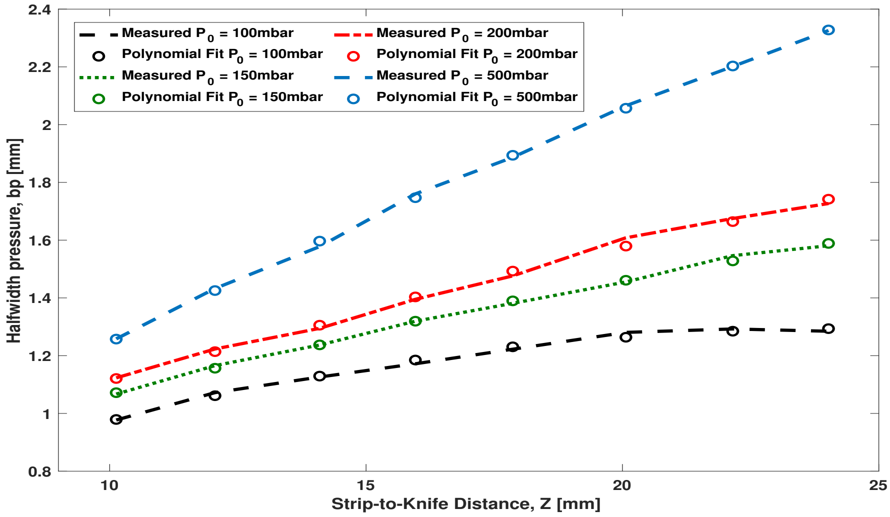

Figure 4-17: Fit of the half-width of pressure profiles (b_p) with strip-to-knife distance (Z)

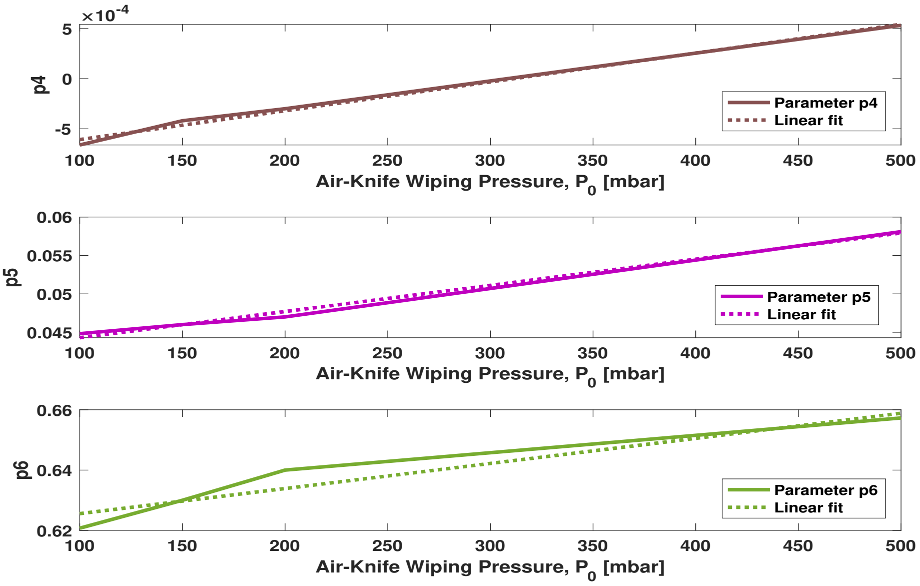

Figure 4-18: Linear fit concerning half-width of pressure distribution model parameters

Finally, the linear dependence of the parameters $p4$, $p5$ and $p6$ with respect to the air-knife wiping pressure (P_0) is given by Equation 4-10.

$$\begin{aligned} p4 &= 2.9816 \times 10^{-8} P_0 - 0.00095 \\ p5 &= 3.3192 \times 10^{-7} P_0 + 0.0415 \\ p6 &= 9.1357 \times 10^{-7} P_0 + 0.6116 \end{aligned} \tag{4-10}$$

4-3-3 Shear Stress Correlations

Since the experimental equipment to measure the wall shear stress was not available, a non-linear grey-box system identification approach was used to model the wall shear stress exerted on the steel strip by the air-knife wiping phenomenon. To evaluate the parameters in the model, the Matlab System Identification Toolbox was used.

As discussed in Subsection 3-3-2, the shear stress model developed by Ellen and Tu [15] for the production data of strip-to-knife distance greater than 8 mm is given by Equation 4-11, Equation 4-12 and Equation 4-13.

$$\frac{\tau}{\tau_{max}} = \operatorname{erf}\left(0.833\xi\right) - 0.2\xi e^{-0.693\xi^2} \tag{4-11}$$

where τ_{max} is maximum shear stress, $\xi = x/b_\tau$ is the dimensionless distance and $b_\tau = x$ is the location of maximum shear stress, given by the parameterized expression:

$$\frac{\tau_{max}}{P_0} = p7\left(Z\right) + p8 \tag{4-12}$$

$$b_\tau = p9\left(Z\right)^2 + p10\left(Z\right) + p11 \tag{4-13}$$

where P_0 is the air-knife wiping pressure and Z is the distance from air knife to the steel strip. p7, p8, p9, p10, and p11 are the five parameters that need to be determined using the non-linear grey-box system identification. It is important to note that the air-knife nozzle gap, d, has been substituted equal to 1 mm in the above equations.

According to Ellen and Tu [15] and Beltao et al. [4], the position of half-width of pressure distribution and the maximum shear stress are the same i.e. $b_p = b_\tau$. Substituting the parameters obtained in Equation 4-10 into Equation 4-13 results in:

$$\begin{aligned} p9 = p4 &= 2.9816 \times 10^{-8} P_0 - 0.00095 \\ p10 = p5 &= 3.3192 \times 10^{-7} P_0 + 0.0415 \\ p11 = p6 &= 9.1357 \times 10^{-7} P_0 + 0.6116 \end{aligned} \tag{4-14}$$

As the mathematical model of the shear stress is known, with two parameters still remaining to be determined from the measured data, it makes sense to use grey-box system identification. To begin with, an *idnlgrey* object is defined to create a non-linear grey-box model, which consists of the first principle model discussed in Section 3-3. The model is updated with the new pressure correlation parameters found in Subsection 4-3-2, and the only unknown parameters remaining are p7 and p8 (Equation 4-12).

Next, these model parameters are estimated using *nlgreyest* function in Matlab. The data used for identification contains 118,020 input-output samples of the galvanizing process as shown in Figure 4-11. The three inputs to the system are the strip speed (V_s), strip-to-knife distance (Z), and air-knife wiping pressure (P_0). The output of the system is the coating weight.

Since the non-linear optimization to be performed is unconstrained, a widely accepted method, namely the **nonlinear least-squares approach**, is used. It tries to minimize the difference between two signals, or the energy of a signal. The non-linear coating weight model function f is parameterized with parameters θ; then, an optimization problem is run to minimize the total error so as to be able to predict the system output correctly.

$$\min_{\theta \in \Theta} E_k(\theta), \quad E_k(\theta) = \sum_{i=1}^{k} ||\epsilon_i||^2 = \sum_{i=1}^{k} ||\left(y_i - f\left(\theta\right)\right)||^2 \tag{4-15}$$

where E_k is the total error as a function of prediction error, y is the measured output, and $\epsilon(\theta)$ is the prediction error vector given by:

$$\epsilon(\theta) = [\epsilon_1(\theta) \quad \epsilon_2(\theta) \quad ..... \quad \epsilon_k(\theta)]^T \tag{4-16}$$

The desired output of the non-linear coating weight model is known, making this as a supervised learning problem. Let us take θ^* to be an optimal solution of the Equation 4-15 obtained from the nonlinear least squares optimization problem.

$$\theta^* = \arg\min \sum_{i=1}^{k} ||\left(y_i - f\left(\theta\right)\right)||^2 \tag{4-17}$$

In general, the most common approach is to solve an optimization at each iteration step along the direction where the total error function E_k is minimized. In this kind of approach, the parameter vector θ will be updated at each iteration such that the error decreases.

$$\theta_{k+1} = \theta_k + d_k \tag{4-18}$$

where d_k is the search direction. The search direction, d_k, is obtained at each iteration using **Levenberg-Marquardt algorithm** [41].

$$d_k = -\left(\lambda I + H\right)^{-1}(\theta_k)\nabla E_k(\theta_k) \tag{4-19}$$

The iterative efficiency of the procedure is improved by exploiting the special structure of the gradient and hessian matrix. Since $E_k(\theta) = ||\epsilon(\theta)||_2^2 = \epsilon^T(\theta)\epsilon(\theta)$, the gradient of E_k is given by:

$$\nabla E_k(\theta) = 2\nabla\epsilon(\theta)\epsilon(\theta) \tag{4-20}$$

and the Hessian is approximated as:

$$H(\theta) = 2\nabla\epsilon(\theta)\nabla^T\epsilon(\theta) \tag{4-21}$$

In our case, the Jacobian of $\epsilon(\theta)$ is given by:

$$\nabla\epsilon(\theta) = \begin{bmatrix} \frac{\partial\epsilon_1}{\partial\theta_1} & \frac{\partial\epsilon_2}{\partial\theta_1} & \cdots & \frac{\partial\epsilon_k}{\partial\theta_1} \\ \frac{\partial\epsilon_1}{\partial\theta_2} & \frac{\partial\epsilon_2}{\partial\theta_2} & \cdots & \frac{\partial\epsilon_k}{\partial\theta_2} \\ \vdots & \vdots & \ddots & \vdots \\ \frac{\partial\epsilon_1}{\partial\theta_k} & \frac{\partial\epsilon_2}{\partial\theta_k} & \cdots & \frac{\partial\epsilon_k}{\partial\theta_k} \end{bmatrix}$$

Using the Hessian derived from Equation 4-21, and substituting it in the **Levenberg-Marquardt algorithm** we get the following relation:

$$\theta_{k+1} = \theta_k - \left(\lambda I + \nabla\epsilon\left(\theta_k\right)\nabla^T\epsilon\left(\theta_k\right)\right)^{-1}\nabla\epsilon\left(\theta_k\right)\epsilon\left(\theta_k\right) \tag{4-22}$$

The number of iterations in the optimization problem depends on the stopping criterion. The most important and widely used criterion is the function tolerance. It is the lower bound on the change in the value of the objective function during an iteration. So essentially, if the change in the cost function is less than the function tolerance, the iteration ends. In our case, the function tolerance is kept to it's default value of 1×10^{-6}.

For non-linear grey box system identification, an initial guess of parameters $p7$ and $p8$ is required. The experimental correlation developed by Elsaadawy et al. [16] (Equation 3-22) is considered for the initial guess of the parameters. Finally, the *nlgreyest* function returns the estimated parameters given by Equation 4-23.

$$\begin{aligned} p7 &= -4.0116 \times 10^{-4} \\ p8 &= 0.0136 \end{aligned} \tag{4-23}$$

The percentage fit between the measured coating weight and the estimated model coating weight is 89.56%. The fit indicates how well the model output matches the measured data and it is calculated using **normalized root mean square squared error** [28].

$$\text{fit} = 100 * \left(1 - \frac{\|y - \widehat{y}\|}{\|y - \text{mean}(y)\|}\right) \tag{4-24}$$

where y is the measurement output and $\widehat{y}$ is model output. Figure 4-19 illustrates the match between the measurement data and the model output.

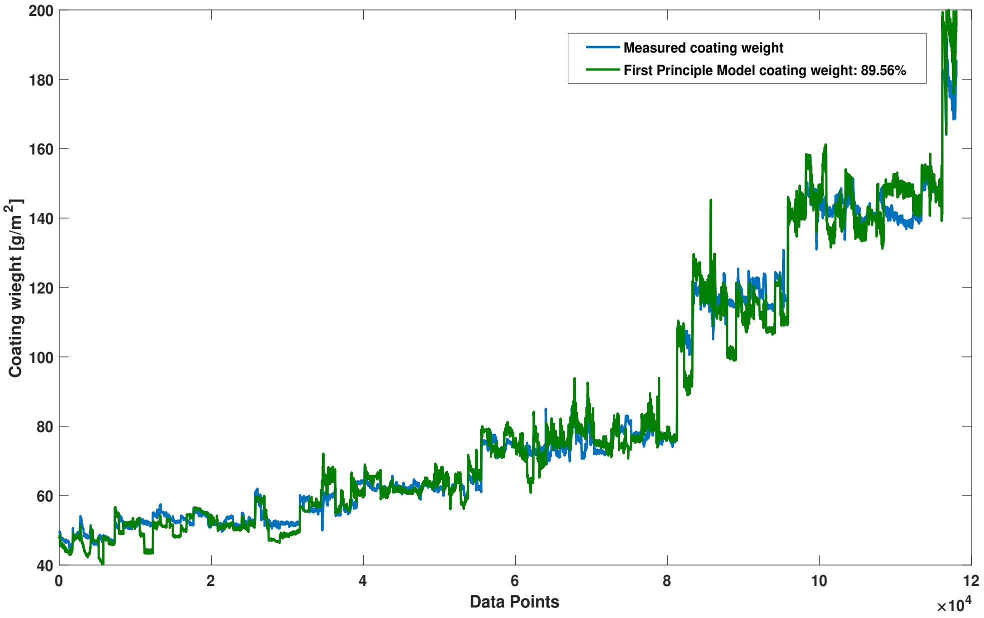

Figure 4-19: Comparison of measured and model coating weight for identification set

The first principle coating weight model with the new estimated parameters is then validated against a validation data set comprising of 47,880 input-output samples. The percentage fit between the measured coating weight data and the estimated model coating weight (illustrated in Figure 4-20) is 83.31%. The fit is calculated using normalized root mean squared error given by the formula in Equation 4-24. The histogram of the percentage in modeling error corresponding to the validation data set is shown in Figure 4-21. It can be noted that the percentage modeling error lies in the range of 0% to 16%.

$$\%\text{Modeling Error} = \frac{\text{Measured cw - Model cw}}{\text{Measured cw}} \times 100 \tag{4-25}$$

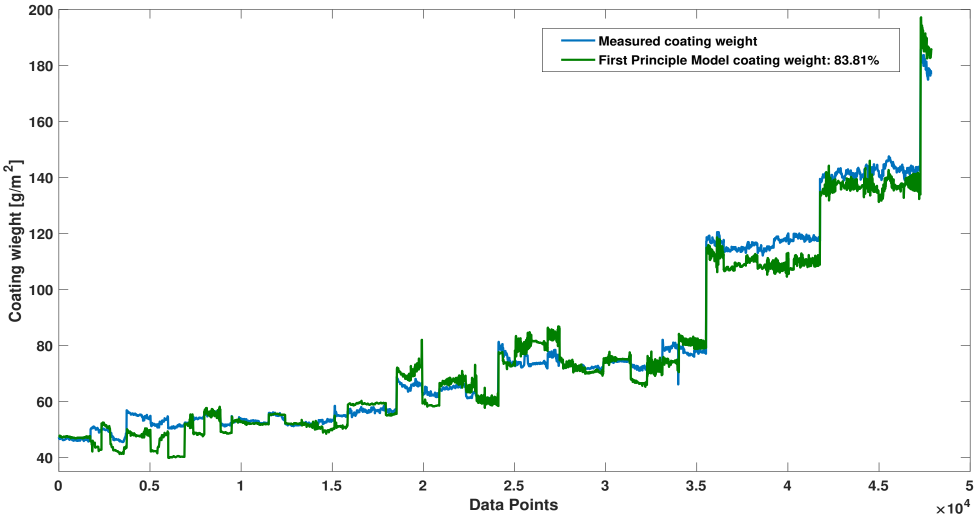

Figure 4-20: Comparison of measured and model coating weight for validation set

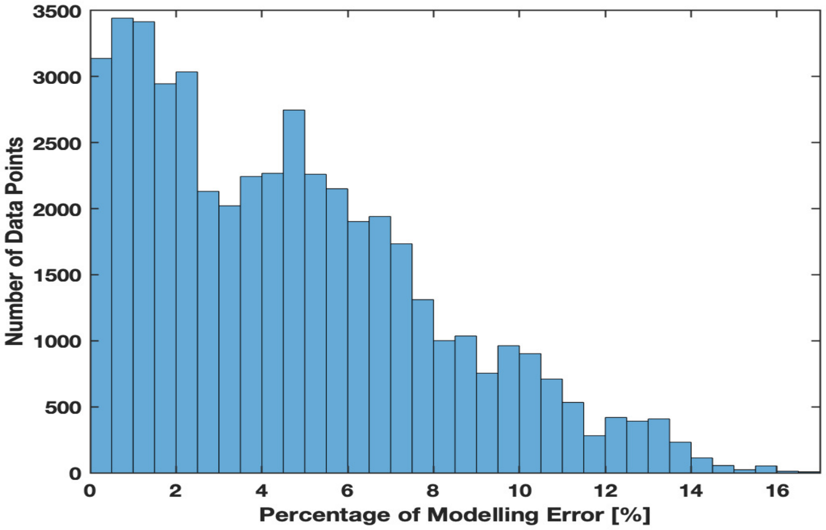

Figure 4-21: Histogram of percentage modeling error in validation set

4-3-4 Improving Model

So far, in the previous two subsections, the parameters in the pressure and shear stress correlations were estimated using the pressure distribution data and the nonlinear grey-box system identification, respectively. The measured coating weight and the first principle model coating weight (with new parameters) observed a percentage fit of 89.56% in the identification data set and 83.31% in the validation data set. In this subsection, the possibility to further improve the coating weight model is discussed.

Figure 4-22 illustrates the modeling error i.e., the difference between the measured coating weight and the model coating weight for the identification data set. The mean of this modeling error is 0.48 g/m^2. It is known that the zinc coating weight is dependent on the three input variables - strip speed (V_s), strip-to-knife distance (Z), and air-knife wiping pressure (P_0). Therefore, an attempt is made to fit a polynomial curve on this error signal with the three input variables using *polyfitn* function in Matlab. This function solves for the coefficients of the polynomial model using the linear least-squares technique. Various orders of polynomial fits were performed on this error signal. For both the identification and validation data set, Table 4-4 indicates the normalized cross-correlation, which is used to measure the similarity between the polynomial fit and the modeling error.

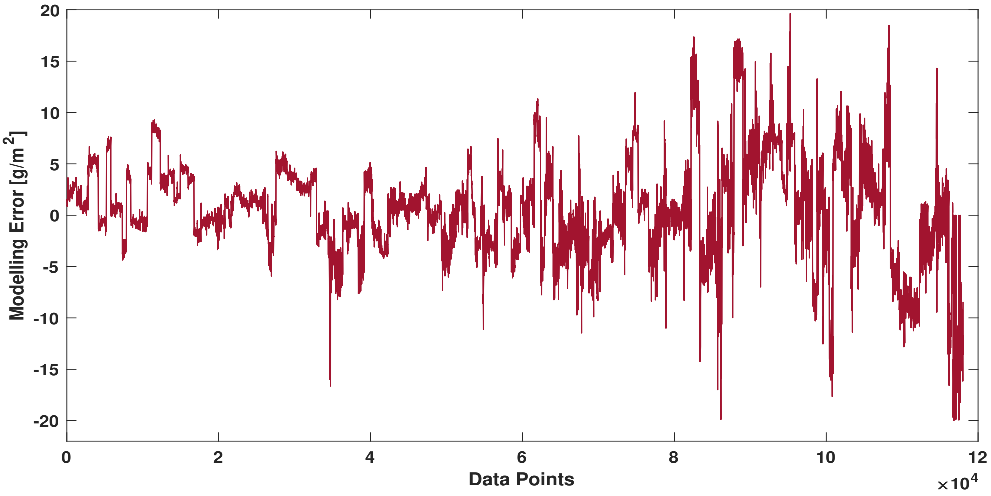

Figure 4-22: Modeling error for identification data set

Polynomial Order	Normalized Cross-Correlation Identification Data	Normalized Cross-Correlation Validation Data
Second	0.272210	0.166259
Third	0.793059	0.756994
Fourth	0.831192	0.715948

Table 4-4: Normalized cross-correlation for various order of polynomial fits

It can be seen from Table 4-4 that higher the order of the polynomial fit, the better is the cross-correlation between the fit and the modeling error in case of identification data. However, in the real sense, the cross-correlation obtained from the validation data indicates the fit's reliability. It can be seen that for the fourth-order polynomial fit, the cross-correlation is better than the third-order polynomial fit in the case of identification data, but at the same time, it is worse for the validation data. It suggests that the fourth-order polynomial fit might be over-fitting the data. Therefore, the fit obtained from the third-order polynomial is more reliable and is given by Equation 4-26.

$$\begin{aligned} cw_{fit} = {} & (6.626 \times 10^{-13})P_0^3 - (9.9054 \times 10^{-9})P_0^2 \cdot Z - (5.3060 \times 10^{-8})P_0^2 \cdot V_s \\ & + (1.7049 \times 10^{-7})P_0^2 - (6.2508 \times 10^{-6})P_0 \cdot Z^2 + (3.5423 \times 10^{-4})P_0 \cdot Z \cdot V_s \\ & + (1.4484 \times 10^{-4})P_0 \cdot Z + (0.0015)P_0 \cdot V_s^2 - (0.0073)P_0 \cdot V_s + (3.9637 \times 10^{-4})P_0 \\ & - (0.0455)Z^3 + (0.002)Z^2 \cdot V_s + (2.1167)Z^2 - (2.7195)Z \cdot V_s^2 + (0.087)Z \cdot V_s \\ & - (31.2670)Z - (13.9735)V_s^3 + (69.2913)V_s^2 - (21.1544)V_s + 143.6011 \end{aligned} \tag{4-26}$$

The coating weight realized from the polynomial fit (cw_{fit}) in Equation 4-26 is then added to the already identified coating weight (cw_{fp}) from the first principle model as shown in Equation 4-27. The normalized histogram of the percentage in modeling error (Equation 4-25) for the model with and without the polynomial fit is plotted in Figure 4-23. By adding the polynomial fit to the model, it is clear that the number of data points for the percentage error from 5% to 16% have dropped significantly. Moreover, with the polynomial fit, the mean of the modeling error has also dropped to zero.

$$\boxed{\boldsymbol{cw = cw_{fp} + cw_{fit}}} \tag{4-27}$$

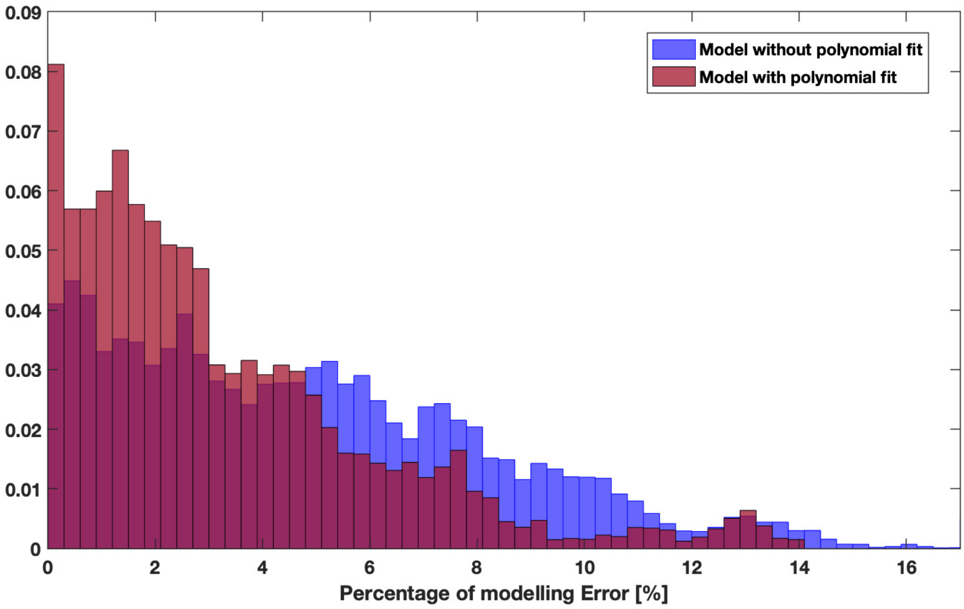

Figure 4-23: Comparison: Normalized histogram of percentage in modeling error with and without polynomial fit

4-3-5 Comparison between different prediction model

At present, Tata Steel makes use of a statistical power-law model to predict the coating weight that depends on the three process parameters, namely the strip speed (V_s), strip-to-knife distance (Z), and air-knife wiping pressure (P_0). The power-law model is given by Equation 4-28.

$$\mathrm{cw} = \left[\frac{P_0}{c_1 \cdot (Z)^{c_2} \cdot (V_s)^{c_3}}\right]^{\frac{1}{c_4}} \tag{4-28}$$

where c_1, c_2, c_3, and c_4 and the four parameters estimated for each set of air-knives. The parameters corresponding to the air-knife set-3 are given by Equation 4-29.

$$\begin{aligned} c_1 &= 29.4127 \\ c_2 &= 0.9727 \\ c_3 &= 1.0657 \\ c_4 &= -1.1715 \end{aligned} \tag{4-29}$$

In this subsection, the results given by the first principle model (with the polynomial fit) and the power-law model are compared. The model with better accuracy will be incorporated into the control system of the air-knife wiping process. Figure 4-24 illustrates the match between the measured coating weight and the output from both the prediction models: first principle model and power-law model for the identification data set. A similar plot between the measurement data and the prediction models is shown in Figure 4-25 for the validation data set. The results from both models are used to perform qualitative analysis using Root Mean Square Error (RMSE).

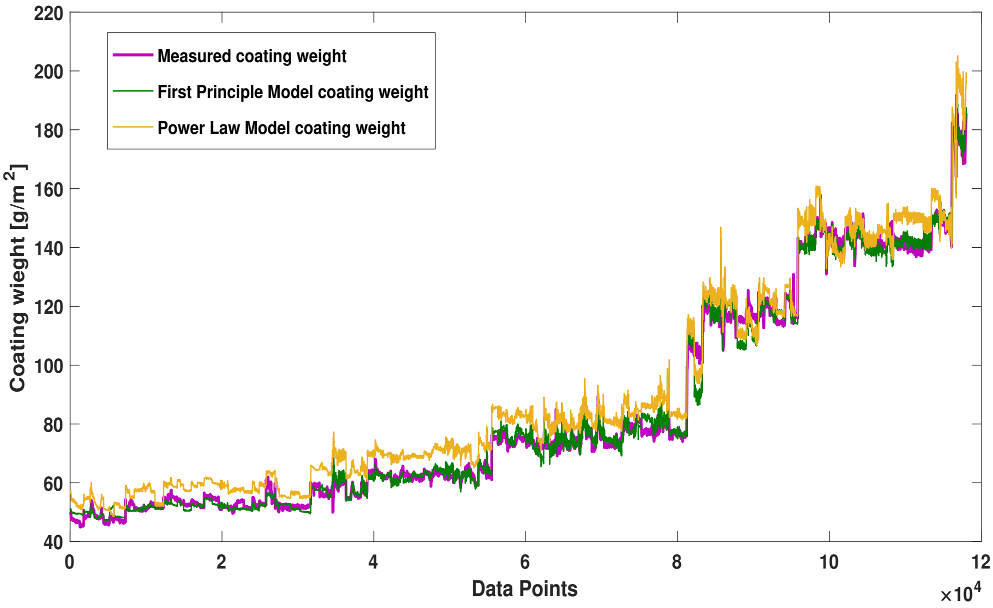

Figure 4-24: Comparison between first principle and power law model - Identification Set

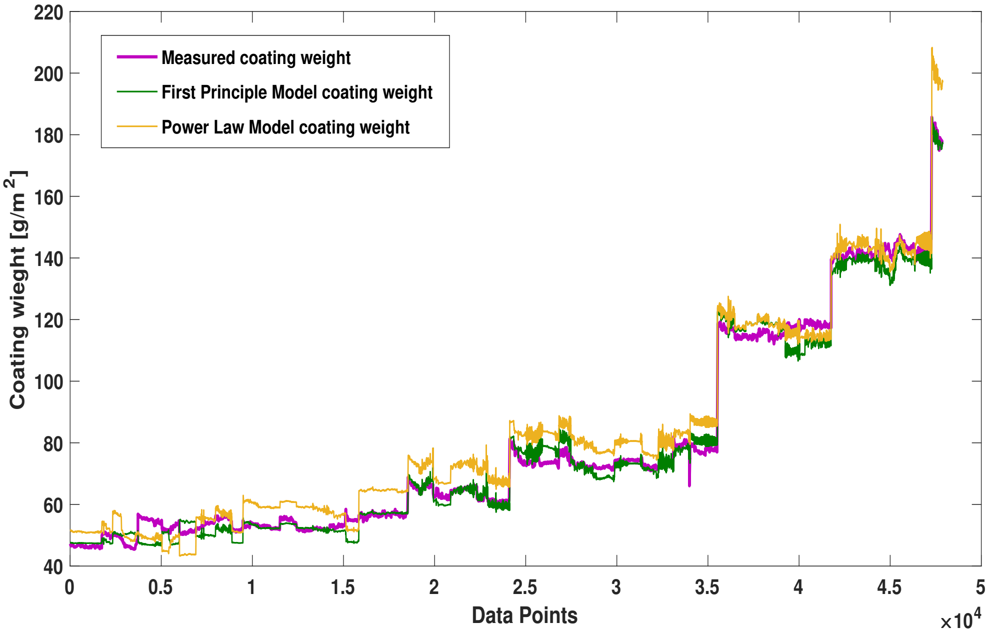

Figure 4-25: Comparison between first principle and power law model - Validation Set

First, the fit indicating how well the model output matches the measured data is specified in Table 4-5. The fit is calculated for both the identification and the validation data set using normalized root mean square squared error given by formula in Equation 4-24. It is quite apparent that the first principle model with estimated parameters offers better accuracy than the power-law model.

Model	Fit - Identification Data	Fit - Validation Data
Power Law	80.20%	80.51%
First Principle	93.80%	89.13%

Table 4-5: Comparison of Power Law Model and First Principle Model - Percentage Fit

Next, the Root Mean Square Error (RMSE) indicating the standard deviation of the difference between the model output and measured data is specified in Table 4-6. The RMSE is calculated for both the identification and validation data set using the formula given by Equation 4-30.

$$\text{RMSE} = \sqrt{\sum_{i=1}^{n} \frac{(y_i - \hat{y}_i)^2}{n}} \tag{4-30}$$

where n is the number of data points, y_1, y_2,..,y_n are measured values and $\hat{y_1}$, $\hat{y_2}$,..,$\hat{y_n}$ are predicted values. It becomes evident that the first-principles model output (with polynomial fit) is closer to the measured data.

Model	RMSE - Identification Data	RMSE - Validation Data
Power Law	6.96 g/m^2	6.39 g/m^2
First Principle	2.92 g/m^2	3.52 g/m^2

Table 4-6: Comparison of Power Law Model and First Principle Model - RMSE

4-4 Estimating Noise Model

As anticipated, it is really difficult to estimate the accurate model parameters in order to match the input-output of the production data. In real life, it is very challenging to eliminate the model errors. Most of the time there are some additional variables or combination of variables that cannot be accounted in the model. Therefore, a noise term is included in the process model that explains the mismatch between the measurements and the model output. It can also include measurement noise and random disturbances. This noise signal has a stochastic nature and can be represented by Auto-regressive (AR) model for the time series. It views a random signal as the output of a linear time invariant system in response to white noise input. For auto regressive case, the linear time invariant system is an all pole system.

$$\sum_{j=0}^{N} a_j n[k-j] = e[k], \quad a_0 = 1 \tag{4-31}$$

where, $n[k]$ is the random noise, $e[k]$ is the zero mean white noise, a_j are the auto-regressive parameters, and N is the model order. The random noise to be modeled using an auto-regressive model is shown in Figure 4-26. This noise signal is obtained as the difference between the measured coating weight and the model coating weight. In order to determine the auto-regressive model, the auto-regressive parameters need to be estimated along with the variance of the input white noise.

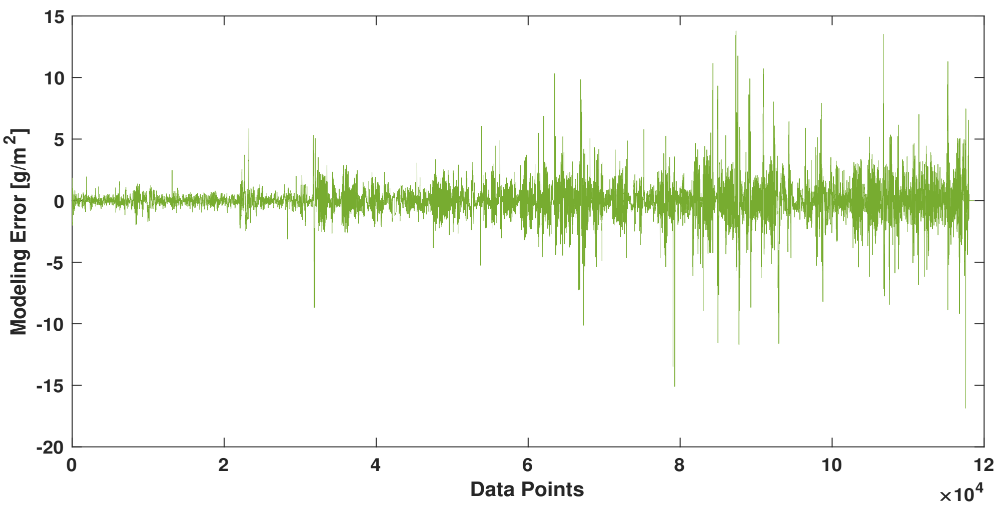

Figure 4-26: Noise Signal

The Yule-Walker approach is employed to determine the parameters of the AR model such that when excited with white noise it will result in an AR signal whose statistics are similar to that of the signal shown in Figure 4-26. In Yule-Walker method, a set of linear equations are solved that relate the auto-correlations of the signal to the auto-regressive parameters $(a_1, a_2, .., a_N)$ of the model with N equations and N unknown parameters. The Matlab function *aryule* is used to compute the parameters of the AR model. This function uses the Durbin-Levinson recursion on the biased estimate of the auto-correlation sequence to compute the parameters.

The first step is to determine the order of the AR model and the partial auto-correlation function (PACF) is used for the identifying the same. With the essentially ideal AR model order, the partial auto-correlation function will decay to zero. Therefore, the partial auto-correlation sequence is plotted against different time lags as shown in Figure 4-27. A 95% confidence interval is defined to help determine when the PACF values are not significantly different from zero. The confidence interval is defined by:

$$\Delta = 0 \pm \frac{\sqrt{2}\mathrm{erf}^{-1}(0.95)}{\sqrt{L}}$$

where, L is the length of the time series. It can be seen that the PACF values are outside the 95% confidence bounds at lag 1, 2 and 3. This shows that the appropriate choice for the model order is 3.

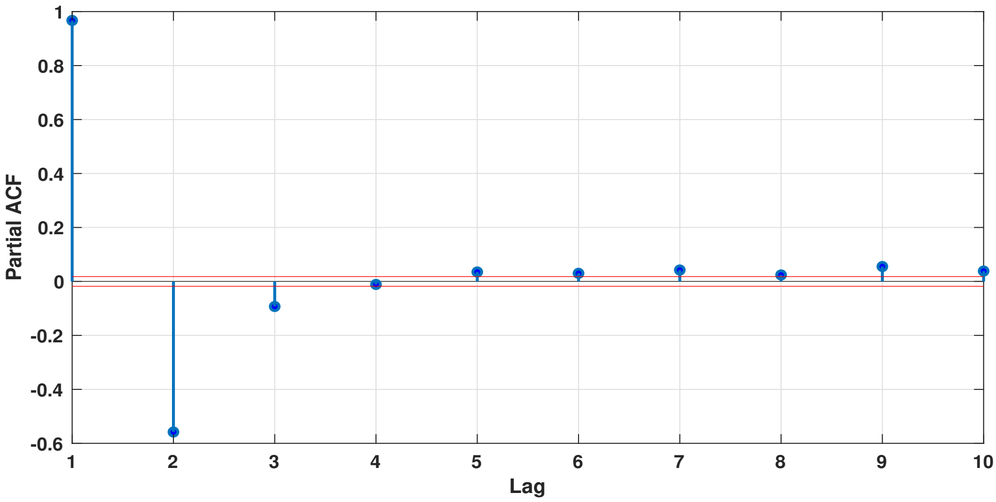

Figure 4-27: Partial Auto-correlation Sequence

The Matlab function *aryule* returns the auto-regressive parameters for a third order AR model (Equation 4-32) along with estimated variance (σ^2=0.07) of the input white noise .

$$n[k] - 1.4551 \cdot n[k-1] + 0.4181 \cdot n[k-2] + 0.0928 \cdot n[k-3] = e[k] \tag{4-32}$$

Rewriting the above equation using shift operator results in:

$$n[k] = \frac{1}{1 - 1.4511q^{-1} + 0.4181q^{-2} + 0.0928q^{-3}} e[k] \tag{4-33}$$

In order to compare how well the AR model has been identified, the power spectral density of the estimated model is overlaid on the power spectral density of the noise signal as shown in Figure 4-28. It can be seen that the noise is mostly concentrated at low frequencies and a good match is obtained in the power spectral density of both the noise signal and the estimated AR model.

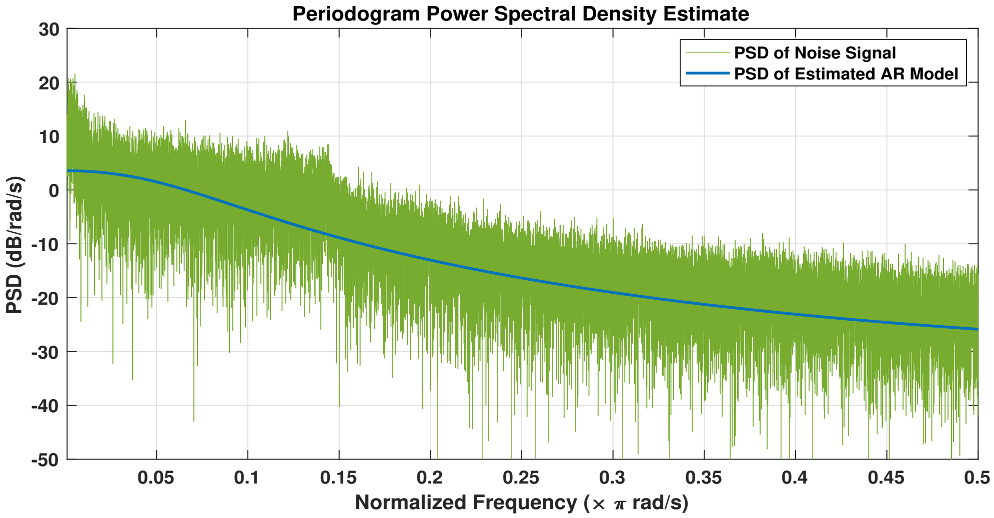

Figure 4-28: Comparison of power spectral density

4-5 Summary

In this chapter, system identification was performed to estimate the second order linear dynamics of fan and the static first-principle coating weight model. The result from the estimated dynamics of fan indicate a good fit between the data and the model.

In the interest of determining the coating weight from the first-principle model, the pressure and shear stress correlations were appropriately parameterized with a set of parameters. The parameters in the pressure correlations were determined based on the experiments performed to realize pressure distribution measurements. However, due to unavailability of experimental equipment to measure the wall shear stress, the parameters in the shear stress were determined using non-linear grey box system identification.

The first-principle coating weight model with the estimated parameters resulted in a fit of 83.1% for the validation data set. Still the mean of the modeling error i.e., the difference between measured coating weight and the model coating weight was found to be 0.5 g/m^2. Therefore, a third-order polynomial was fitted to the error signal and then added to the already identified first-principle coating weight model. By doing so, the mean of the modeling error dropped to zero.

In the coating process, it is difficult to remove all the modeling errors because there are some or the other external factors or combination of factors that are not accounted for in the model. As a result, a noise term is added in the process model that explains the mismatch between measured data and the model output.

Chapter 5

Time Delay

5-1 Introduction

As discussed in Chapter 3, the X-ray coating gauge used to measure the coating weight is installed at a significant distance from the air knife, as shown in Figure 5-1. This distance induces a substantial time-varying measurement delay because of the varying strip speed. In this Chapter, the formulation of the time-varying measurement delay is discussed. Moreover, to identify the static non-linear coating weight model presented in Section 4-3, it is essential to deal with the difficulty of the measurement delay. As the coating weight measurements are delayed, they need to be traced back to the point where it matches the impact of the process variables.

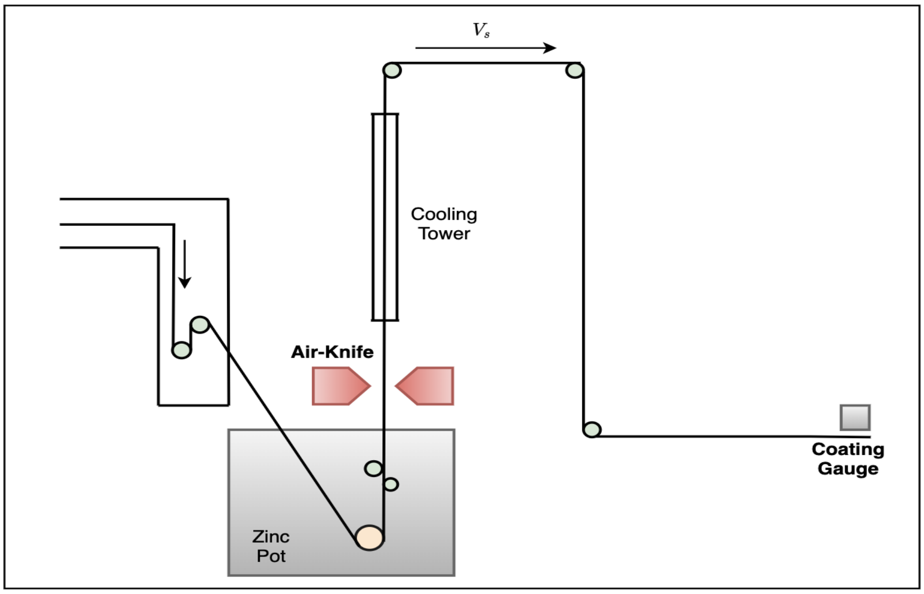

Figure 5-1: Schematic representing the distance between Air-knife and Coating gauge

5-2 Properties of Time Delay Systems

In this section, the representation of time-delays in continuous and discrete time is discussed along with some of their properties. The system with time delays are represented by the form:

$$\begin{aligned} \bar{F}(s) &= \bar{F}_r(s) \cdot e^{-s\tau_d} \quad \text{(continuous-time)} \\ F(z) &= F_r(z) \cdot z^{-N_d} \quad \text{(discrete-time)} \end{aligned} \tag{5-1}$$

where τ_d is the time delay, N_d is the number of sample periods during the delay, $\bar{F}_r(s)$ and $F_r(z)$ are the transfer functions without time delay.

5-2-1 Continuous-Time System

Pure time delay with the transfer function $F(s) = e^{-s\tau_d}$ is of infinite order because, at any point in time, an infinite number of values are necessary to define the state of the system. The main challenge in handling continuous time delays is not the modeling aspect, but the problem lies in the fact that this delay is not a rational function of s [5]. Therefore, there is a need of approximating time delays that have rational function forms $F(s) = \frac{N(s)}{D(s)}$ using different approaches, some of these are:

- Taylor Series Expansion (All zero approximations): The Taylor series expansion of time delay $e^{-s\tau_d}$ is given by Equation 5-2. Considering the first two terms and truncating the rest will result in first order Taylor series.

$$e^{-s\tau_d} = 1 - \frac{s\tau_d}{1!} + \frac{(s\tau_d)^2}{2!} - \frac{(s\tau_d)^3}{3!} + \dots \tag{5-2}$$

- Taylor Series Expansion (All pole approximations): It is important in many applications to make the numerator order equal to or less than that of the denominator. This approximation, therefore, only consists of poles by putting the exponential term in the denominator.

$$e^{-s\tau_d} = \frac{1}{e^{s\tau_d}} = \frac{1}{1 + \frac{s\tau_d}{1!} + \frac{(s\tau_d)^2}{2!} + \frac{(s\tau_d)^3}{3!} + \dots} \tag{5-3}$$

- Pade Approximation: It is an even better approximation of the exponential term, as it is represented as a ratio of polynomials [32]. Depending on the number of terms considered, the order of the approximation is determined.

$$e^{-s\tau_d} = \frac{1 - s\left(\frac{\tau_d}{2}\right) + s\left(\frac{\tau_d}{2}\right)^2 - \dots}{1 + s\left(\frac{\tau_d}{2}\right) + s\left(\frac{\tau_d}{2}\right)^2 + \dots} \tag{5-4}$$

5-2-2 Discrete-Time System

On discretizing the system, if the sampling period is unchanged and the delay is an integer multiple of sampling time, then a set of pure differential equations in the state space format can describe the discrete time-delay. Also, time delays in discrete-time $F(z) = z^{-N_d}$ are of finite dimension [5] and can be expressed as a rational functional function of z. It is easy to deal with time delays in discrete time as it becomes a shift in the state variable vector.

5-3 Formulation of Time-Varying Measurement Delay

The concept of time-varying measurement delay is best explained, as shown in Figure 5-2, where cw is the coating weight developed just after the air knife and cw_{delay} is the coating weight measured at a constant distance L from the air knife by the cold-coating gauge. The zinc coating travels with the same speed as the strip speed $V_s(t)$. Assuming no dynamics in the way, the thickness at the measurement point will be given by:

$$cw_{delay}(t) = cw(t - \tau_d(t)) \tag{5-5}$$

where $\tau_d(t)$ is the time-varying measurement delay. It is not known explicitly and, therefore, is computed from the length L and the speed of the strip $V_s(t)$. Then, Equation 5-5 can be written as:

$$cw_{delay}(t) = cw(t - \tau_d(L, V_s(t))) \tag{5-6}$$

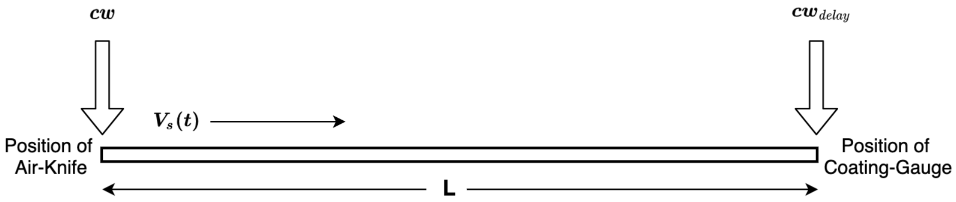

Figure 5-2: Formulation of time-varying measurement delay

The delay introduced in the equation Equation 5-5 could have been given by Equation 5-7 if the strip travelled the whole distance at a constant speed.

$$\tau_d = \frac{L}{V_s} \tag{5-7}$$

Although in our process, that is not the case. During each sample time T_s, the strip moves at a particular velocity and thus covers only a fraction of the overall distance L. Therefore, the speed of the strip may differ in the next sampling period, covering another fraction of the total distance. After a few sampling periods, say N_d, the coating thickness will be measured by the coating gauge. Figure 5-3 illustrates how the varying strip speed affects the position of coating weight at each sampling period.

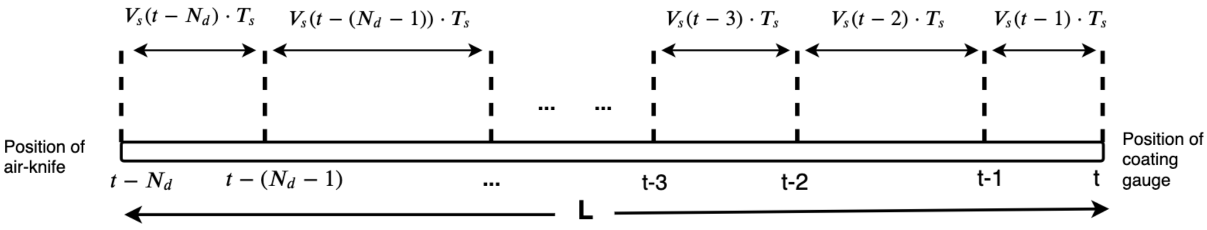

Figure 5-3: Position at each sampling time of coating weight

It is important to emphasize that the measurement delay depends not only on the current strip speed $V_s(t)$, but also on the previous strip speeds. In continuous time, the measurement delay is given by the following expression:

$$\boldsymbol{\tau_d = \frac{L}{V_{avg}}} \tag{5-8}$$

where $V_{avg} = \frac{1}{\tau_d}\int_{t-\tau_d}^{t} V_s(T)dT$ is the average speed that the coating thickness experiences starting from the air knife till the coating gauge. Equation 5-8 can be rewritten as:

$$\boldsymbol{L = \int_{t-\tau_d}^{t} V_s(T)dT} \tag{5-9}$$

Translating this measurement delay in discrete time, with a sampling period of T_s is given by:

$$\boldsymbol{L = T_s \sum_{i=1}^{N_d} V_s(t-i)} \tag{5-10}$$

where N_d is the discrete-time delay, and t denotes the discrete-time index. N_d is calculated at each sampling instant as the number of the speeds to be summed before the overall sum exceeds $\frac{L}{T_s}$.

5-4 Calculation of Time-Varying Measurement Delay

The data was collected from the production line at a sampling interval of 1 sec. On inspecting the relevant signals from the IBA Analyzer (a tool used by Tata Steel), the distance between the air-knife and the coating gauge was found to be 153.5 meters. Since the minimum strip speed is 60 m/min (1 m/s), the maximum measurement delay possible is 153.5 seconds. Therefore, the data was collected for an additional time of 154 seconds.

As the strip speed (V_s) is already known to us from the production data, the delay is calculated as the number of strip speeds [m/s] to be summed before the total sum exceeds 153.5 meters. Once the time delay is calculated, the measured coating weight value is shifted back by that amount in the database. After determining the coating weight values at the position of the air-knife, the additional data of 154 seconds is removed from all the process variables. The step by step procedure of this process is explained in Appendix A.

Once the database is corrected for the time delay present in the static system, the measured coating weight values correspond to the correct impact of the process variables. Subsequently, different data files were examined in order to verify the results. The most appropriate signal to investigate the accuracy of the calculated time delay is a step-change in the reference coating weight. The relevant signals from one of the corrected data files are plotted in Figure 5-4. The coating weight reference change from 70 g/m^2 to 60 g/m^2 occurs at t = 1262 sec. At the same instant, a step increase in $P_{setpoint}$ (control input to the fan) is observed. As already derived in Subsection 4-2-2, a delay of three seconds can be noticed in the fan's dynamics. The air-knife wiping pressure (P_0) begins to increase at t = 1265 sec. It can be clearly perceived that the measured coating value begins to decrease at the same time instant the air-knife wiping pressure (P_0) begins to increase. Thus, it proves that the measured coating weight values are shifted back in time with the correct time delay values.

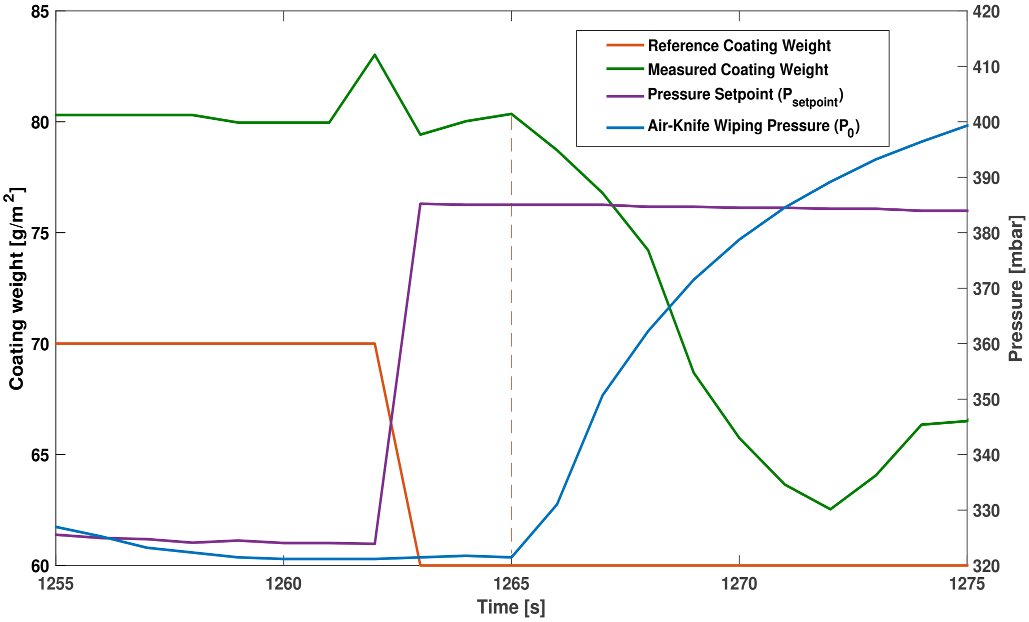

Figure 5-4: Data-set depicting the accuracy of the calculated time delay

Chapter 6

Model Discretization

6-1 Selection of Sampling Time

In control systems, the controller operation is implemented digitally. Therefore, a sampling time T_s must be selected before any control takes into action. A drawback of digital control is that aliasing may occur. Hence, the sampling frequency must be chosen per the guidelines offered by the Nyquist-Shannon sampling theorem to avoid aliasing.

The **Nyquist-Shannon theorem** describes how to sample a signal such that no information is lost. It states that "a band limited signal with frequency content in the band [-ω_B,ω_B] (rad/s) must be sampled with a sampling frequency $\boldsymbol{\omega_s \geq 2\omega_B}$ in order to reconstruct the signal from the recorded samples" [48].

The only dynamics present in the system are those of the fan in the air-knives given by the following transfer function:

$$T.F. = \frac{0.1142}{s^2 + 0.5405s + 0.1141}e^{-3s} \tag{6-1}$$

In general, the frequency band of interest of the signals involved is majorly dominant by the bandwidth of the system. The bandwidth of this linear, time-invariant system is defined as "the frequency ω_B at which the magnitude of the frequency response function first drops below -3 dB from its DC value" [44]. Figure 6-1 illustrates the magnitude plot of the dynamics in the fan. The vertical dotted line depicts the frequency at which the magnitude of the frequency response function crosses the -3 dB mark. Therefore, the bandwidth of the system is given as:

$$\boldsymbol{\omega_B = 0.2937 \text{ rad/s} = 0.0467 \text{ Hz}} \tag{6-2}$$

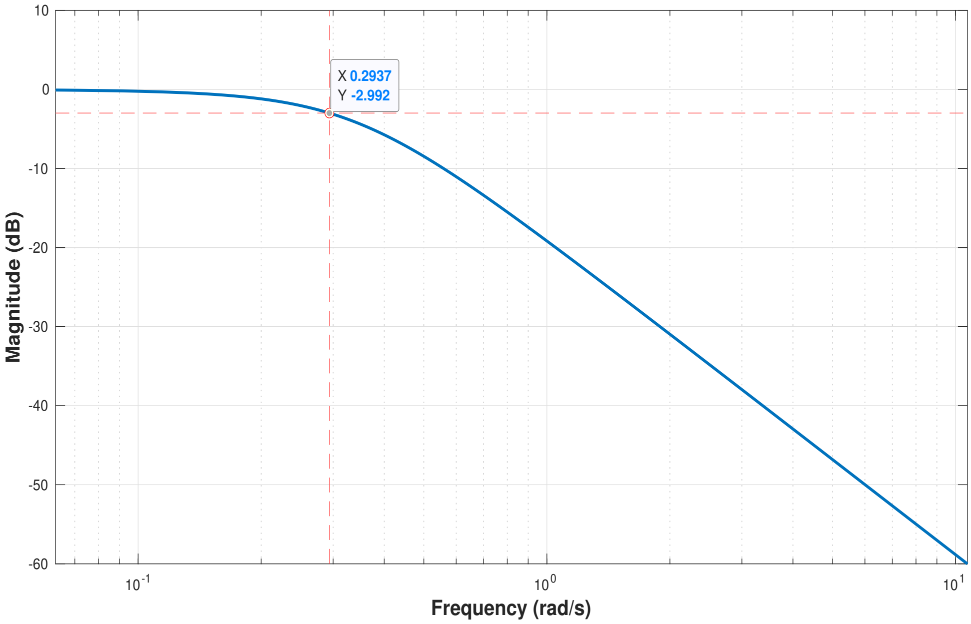

Figure 6-1: Bode magnitude plot of fan dynamics

As discussed, according to the Nyquist-Shannon theorem, the sampling frequency must be greater than twice the system bandwidth, indicating that the sampling time T_s must be less than equal to 10.7 seconds.

$$\begin{aligned} \omega_s &\geq 2\omega_B \\ \omega_s &\geq 0.5847 \ \text{rad/s} \\ f_s &\geq 0.0934 \ \text{Hz} \\ T_s &\leq 10.7 \ \text{seconds} \end{aligned} \tag{6-3}$$

If the sampling time T_s is picked too large, it will restrict the controller's freedom to swiftly change the input to get the coating weight to the reference as quickly as possible. On the other hand, if the T_s picked is too small, it will needlessly increase the computation load. Therefore, a pragmatic choice would be to take the sampling time **T_s to be equal to 1 second** such that the optimization required in Non-linear Extended Prediction Self-Adaptive Control (NEPSAC) is solvable in the sampling interval.

6-2 Discretization

Discretization must be introduced in order to prepare an appropriate model for the evaluation and implementation of a digital system. In the entire coating weight model, only the dynamical part i.e. the fan dynamics (Equation 6-1) requires discretization. The dynamics include three seconds of time delay, which is the time it takes for the output (P_0) to react to the input ($P_{setpoint}$). Therefore, the transfer from the input to output must be extended with the three-second delay.

As discussed in Section 5-2, if the sampling time is constant and the time delay is an integral multiple of sampling time, it becomes easy to represent time delay in discrete time as it becomes a shift in the state variable vector. Therefore, it is wise to discretize the fan dynamics without the three-second delay and then later extend the state space by the same amount as the time delay.

The first step is to obtain a linear continuous-time state-space representation of the delay-free transfer function given in Equation 6-1. In control engineering, the state space representation for a process is used to describe a system as a set of state, input, and output variables. The following form gives the most general linear state space representation:

$$\begin{aligned} \dot{x}(t) &= Ax(t) + Bu(t) \\ y(t) &= Cx(t) + Du(t) \end{aligned} \tag{6-4}$$

where x, u and y are the state, input ($P_{setpoint}$) and output (P_0) variables. A, B, C, and D are called the state matrix, input matrix, output matrix, and feed-through matrix. The transfer function representation (excluding time delay) is converted into an equivalent continuous-time state-space representation by using *tf2ss* function in MATLAB. The state-space matrices obtained are as follows:

$$A = \begin{bmatrix} -0.5405 & -0.1141 \\ 1 & 0 \end{bmatrix} \qquad B = \begin{bmatrix} 1 \\ 0 \end{bmatrix}$$

$$C = \begin{bmatrix} 0 & 0.1142 \end{bmatrix} \qquad D = \begin{bmatrix} 0 \end{bmatrix}$$

Next step is to convert these continuous-time state equations into discrete-time state equation by transforming the matrices $(A, B, C, D) \rightarrow (A_d, B_d, C_d, D_d)$. The most common method that provides a discretization in the time domain for staircase inputs, known as zero-order hold, is used to discretize the system. The zero-order hold system holds each sample input value constant over one sample period, i.e., the input control signal stays constant until the next sample time.

Given the sampling time $T_s = 1$ second, the continuous-time state-space model is transformed into discrete-time state-space representation given by the following form:

$$\begin{aligned} x[k+1] &= A_d x[k] + B_d u[k] \\ y[k] &= C_d x[k] + D_d u[k] \end{aligned} \tag{6-5}$$

A detailed derivation of the zero-order hold discretization is described in Appendix B. The discrete-time state-space matrices are given by:

$$\begin{aligned} \boldsymbol{A_d} &= \mathbf{e}^{\boldsymbol{AT_s}} \\ \boldsymbol{B_d} &= \boldsymbol{A}^{-\mathbf{1}} \left(\mathbf{e}^{\boldsymbol{AT_s}} - \boldsymbol{I} \right) \boldsymbol{B} \\ \boldsymbol{C_d} &= \boldsymbol{C} \\ \boldsymbol{D_d} &= \boldsymbol{D} \end{aligned} \tag{6-6}$$

Using the *c2d* function in MATLAB, the discretized matrices are calculated to be as follows:

$$A_d = \begin{bmatrix} 0.5427 & -0.0865 \\ 0.7580 & 0.9524 \end{bmatrix} \qquad B_d = \begin{bmatrix} 0.7580 \\ 0.417 \end{bmatrix} \tag{6-7}$$

$$C_d = \begin{bmatrix} 0 & 0.1142 \end{bmatrix} \qquad D_d = \begin{bmatrix} 0 \end{bmatrix} \tag{6-8}$$

Momentarily, the fan dynamics have been discretized without the time delay. At this stage, it makes sense to extend the state-space from the input ($P_{setpoint}$) to output (P_0) with three seconds of delay. With the sampling time $T_s = 1$ second, three additional states are added to the state-space description. Finally, the discrete-time state matrices are updated, and the following state-space representation for the fan dynamics is obtained:

$$\begin{aligned} x[k+1] &= \underbrace{\begin{bmatrix} 0.5427 & -0.0865 & 0 & 0 & 0 \\ 0.7580 & 0.9524 & 0 & 0 & 0 \\ 0 & 0.1142 & 0 & 0 & 0 \\ 0 & 0 & 1 & 0 & 0 \\ 0 & 0 & 0 & 1 & 0 \end{bmatrix}}_{A_d} x[k] + \underbrace{\begin{bmatrix} 0.7580 \\ 0.417 \\ 0 \\ 0 \\ 0 \end{bmatrix}}_{B_d} u[k] \\ y[k] &= \underbrace{\begin{bmatrix} 0 & 0 & 0 & 0 & 1 \end{bmatrix}}_{C_d} x[k] \end{aligned} \tag{6-9}$$

6-3 Process Model Representation

In this section, a single state-space representation to describe the entire coating weight process model is presented, which is a combination of linear dynamics of the fan, nonlinear static model, time delay, and the noise model, as shown in Figure 6-2. $P_{setpoint}$ is the only control input to his model, along with two measured disturbances: V_s (strip speed) and Z (strip-to-knife distance). The final output of the system is the coating weight (cw_{final}).

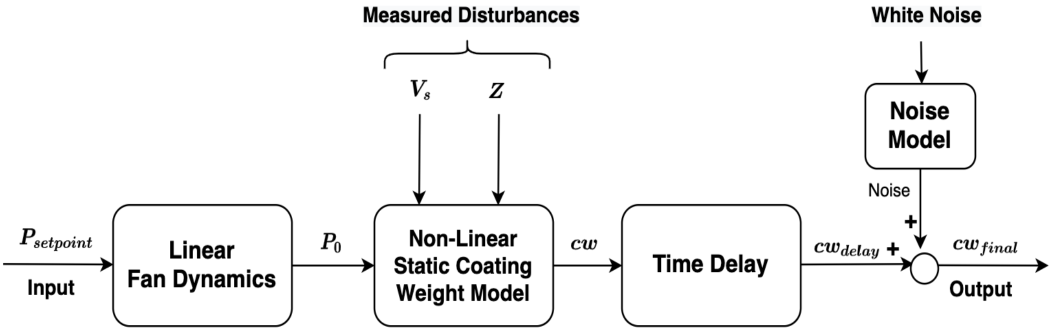

Figure 6-2: Process Model

It is essential to realize that the air-knife wiping pressure (P_0) is an intermediate variable that is determined by the value of the last state in the state variable vector (Equation 6-9). For simplicity, all the variables are defined in the standard format as:

$$u = (P_{setpoint}) \quad x = \begin{pmatrix} x_1 \\ x_2 \\ x_3 \\ x_4 \\ x_5 \end{pmatrix} \quad w = \begin{pmatrix} V_s \\ Z \end{pmatrix} \quad y = (cw_{final}) \tag{6-10}$$

where u, x, w, and y represent the input, state, measured disturbances, and output of the system respectively. Finally, the entire process model can be represented by the discrete-time state-space representation given by Equation 6-11.

$$\begin{aligned} x[k+1] &= A_d x[k] + B_d u[k] \\ y[k+N_d] &= f\left(x[k], w[k]\right) + n[k] \end{aligned} \tag{6-11}$$

where, A_d and B_d are the discrete-time state and input matrices given by Equation 6-9. f is the static non-linear function (described in Section 3-3) that depends on the air-knife wiping pressure P_0 ($P_0 = x_5[k]$) and the measured disturbances V_s and Z ($w[k]$) to calculate the coating weight. As a consequence of the distance between the air-knife and the coating gauge, there exists a large time-varying measurement delay. N_d is the discrete time delay calculated using the formulation given by Equation 5-10. In the end, $n[k]$ represents the estimated noise signal obtained using the noise model identified in Section 4-4.

Chapter 7

Smith Predictor with PI Controller

This chapter focuses on one of the most popular dead-time compensation methods known as the Smith predictor. It is the industry's best-recognized and most often used dead-time compensation method. In the view of this chapter, certain controller tuning approaches will be studied in-depth, and the key benefits and disadvantages of the smith predictor will also be addressed.

7-1 Introduction

The coating weight's ideal control could have been achieved if the coating gauge was installed just after the air-knives. The plant output could have been immediately fed back with no time-delay, and a simple PI controller could've be tuned to achieve satisfactory performance. The real implementation of this approach is not feasible primarily because the sensor cannot be mounted at the desired location [18].

The idea of a process model is an easy way of solving this problem. If the dead-time-free model of the process is available, the model output may be fed-back back to the controller. In this framework, the controller may be tuned based on the process model, and the output of the closed-loop will depend on how reliable the model is. It is important to note that this approach cannot be used in practice because the controller won't be able to account for the disturbances and the model mismatch. Therefore, all the valuable properties of feedback control are lost. An improved version of this solution was suggested by Smith based on a closed-loop prediction structure.

Otto Smith, in 1957 [31], introduced the plan of action for Smith predictor. Basically, a mathematical model of the process is developed and decoupled from the time delay. The real process output is then compared with the output of the developed model (with time delay) in order to estimate the disturbances and unmodeled dynamics. The difference is then passed through to a low-pass filter and then added to the delay-free model output. The outcome is fed-back and compared to the target or the reference point. So the error is sent through a controller, which further minimizes the error to zero. Figure 7-1 illustrates the layout of the Smith predictor.

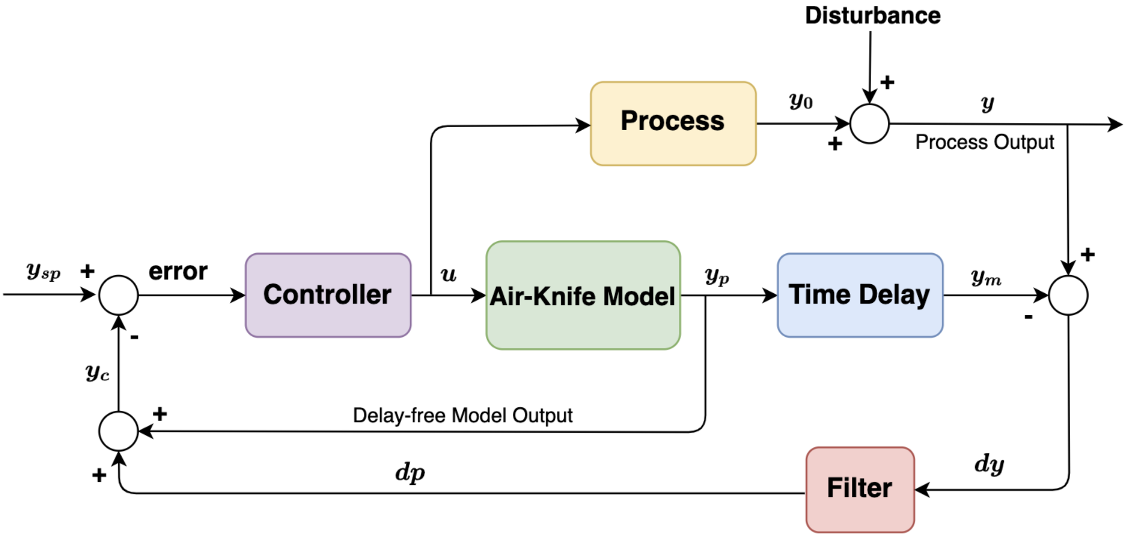

Figure 7-1: Schematic representation of Smith Predictor

Since the PI controller is the most frequently encountered controller in the process industry, it is implemented in the control-loop configuration of the Smith predictor. In addition, the Smith predictor may be regarded as an advanced control method since it uses a process model to evaluate the output. This enables the internal PI controller to manage the process as if there is no delay. This feedback loop will significantly increase the performance of the controller if the process model is appropriately identified.

A few of the PI controller tuning methods used to monitor time-delay processes are Cohen and Coon tuning algorithm, Frequency response method by Ziegler and Nichols, and Tavakoli-Fleming tuning rule. All these methods are mostly used when there is no knowledge about the process. However, in our case, utilizing the model's information to tune the PI controller based on the frequency response makes more sense. As the coating weight process is non-linear, it is crucial to choose an operating point to linearize the process before utilizing the frequency response method.

7-2 Linearization

It is known that a linear transfer function represents the dynamics of fan in the air-knives. Thus, the only part of the model that includes non-linear behavior is the static coating weight model. Therefore, there is a need to linearize the static model around an operating point. As the operating range of all the process variables is quite huge, it is logical to linearize it around more than one operating point. Five operating points were chosen to cover the maximum possible range of all the three process variables and the coating weight values obtained from them.

- $P_0 = 48300$ [Pascal] , $V_s = 2.02$ [m/s] , $Z = 12.21$ [mm] , $cw = 50.81$ [g/m^2]
- $P_0 = 36600$ [Pascal] , $V_s = 2.01$ [m/s] , $Z = 14.68$ [mm] , $cw = 75.15$ [g/m^2]
- $P_0 = 24300$ [Pascal] , $V_s = 1.61$ [m/s] , $Z = 18.02$ [mm] , $cw = 109.11$ [g/m^2]
- $P_0 = 28670$ [Pascal] , $V_s = 2.59$ [m/s] , $Z = 17.23$ [mm] , $cw = 141.66$ [g/m^2]
- $P_0 = 21390$ [Pascal] , $V_s = 2.08$ [m/s] , $Z = 21.39$ [mm] , $cw = 200.28$ [g/m^2]

The following state-space representation represents the non-linear static model:

$$y = f(x, w) \tag{7-1}$$

where f is the static non-linear function (described in Section 3-3) that depends on the air-knife wiping pressure P_0 ($P_0 = x_5$) and the measured disturbances V_s and Z (w) to calculate the coating weight. The non-linear model is linearized by using the first-order Taylor expansion, given as:

$$f(x, w) \approx f(x_{5s}, w_s) + \left.\frac{\partial f}{\partial x_5}\right|_{x_{5s}, w_s} (x_5 - x_{5s}) + \left.\frac{\partial f}{\partial w}\right|_{x_{5s}, w_s} (w - w_s) \tag{7-2}$$

where x_{5s} and w_s are state (P_0) and measured disturbances (V_s,Z) at the operating points. Since the model is not linearized in steady-state but in an operating point, an additional term $f(x_{5s}, w_s)$ appears in the state-space description. The value of this offset term is determined using the non-linear model. Finally, linearized equations depicting the static coating weight model at five operating points are given as:

$$\begin{aligned}
y &= 50.81 + \begin{bmatrix} -0.0010 & 25.1135 & 2.3350 \end{bmatrix} \begin{bmatrix} x_5 - 48300 \\ w(1) - 2.02 \\ w(2) - 12.21 \end{bmatrix} \\
y &= 75.15 + \begin{bmatrix} -0.0020 & 37.2593 & 3.8827 \end{bmatrix} \begin{bmatrix} x_5 - 36600 \\ w(1) - 2.01 \\ w(2) - 14.68 \end{bmatrix} \\
y &= 109.11 + \begin{bmatrix} -0.0044 & 67.1596 & 6.7464 \end{bmatrix} \begin{bmatrix} x_5 - 24300 \\ w(1) - 1.61 \\ w(2) - 18.02 \end{bmatrix} \\
y &= 141.66 + \begin{bmatrix} -0.0048 & 54.1787 & 8.3368 \end{bmatrix} \begin{bmatrix} x_5 - 28670 \\ w(1) - 2.59 \\ w(2) - 17.23 \end{bmatrix} \\
y &= 200.28 + \begin{bmatrix} -0.0089 & 94.0752 & 15.271 \end{bmatrix} \begin{bmatrix} x_5 - 21390 \\ w(1) - 2.08 \\ w(2) - 21.39 \end{bmatrix}
\end{aligned} \tag{7-3}$$

To see if these linearized equations describe the static non-linear model correctly around the operating point, coating weight values obtained from both the linearized and non-linear models are compared. In order to do so, 30 data points covering a wide range of all the process variables are picked from the production data, as shown in Figure 7-2.

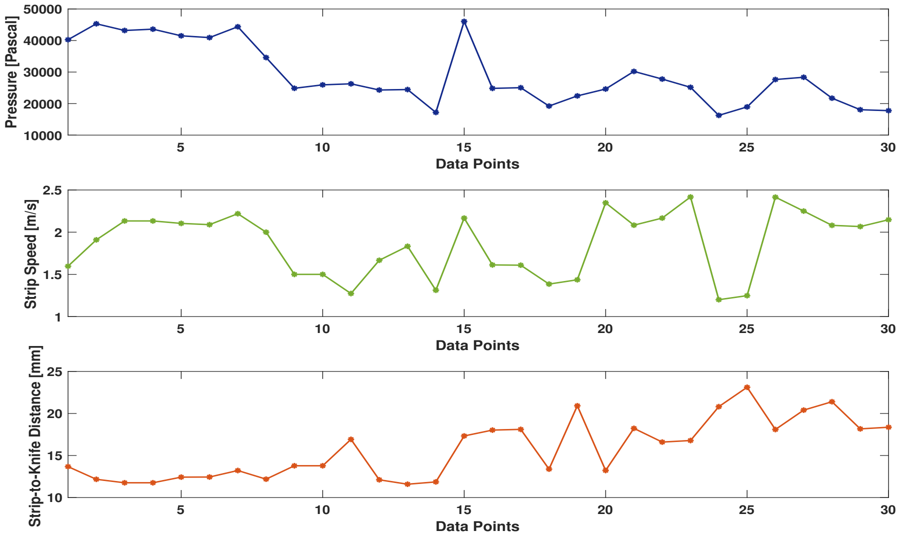

Figure 7-2: Data set for comparing linearized and non-linear model

Figure 7-3 illustrates the coating weight values obtained from the non-linear model and the linearized model with the first operating point. It is evident that the first linearized model (Equation 7-3) approximates well for the process variables resulting in coating weight values of around 50 g/m^2.

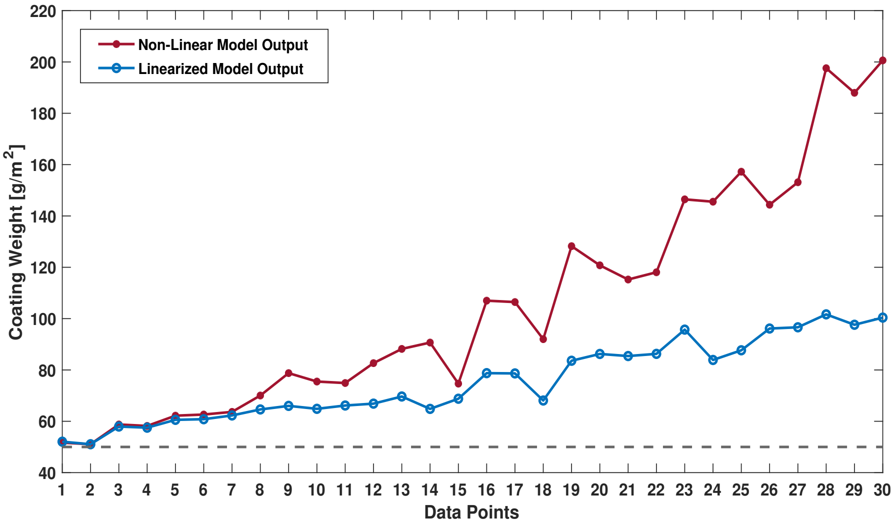

Figure 7-3: Comparison of non-linear model and linearized model around first operating point

Figure 7-4, Figure 7-5, Figure 7-6, and Figure 7-7 illustrate the coating weight values obtained from the non-linear static model and the linearized model around the second, third, fourth, and fifth operating point respectively. It can be seen that the linearized models (Equation 7-3) approximate well for the process variables resulting in coating weight values of around 75 g/m^2, 110 g/m^2, 140 g/m^2, and 200 g/m^2 respectively.

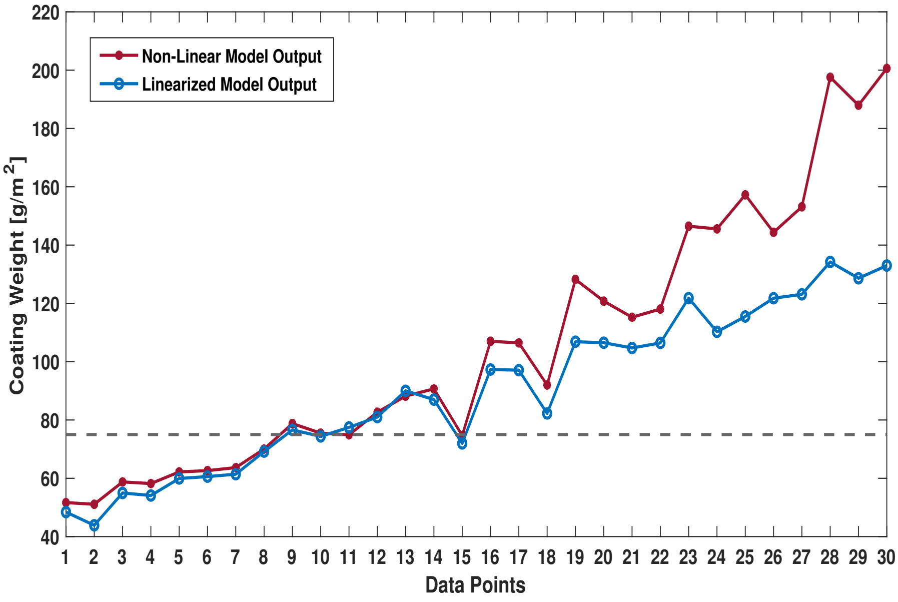

Figure 7-4: Comparison of non-linear model and linearized model around second operating point

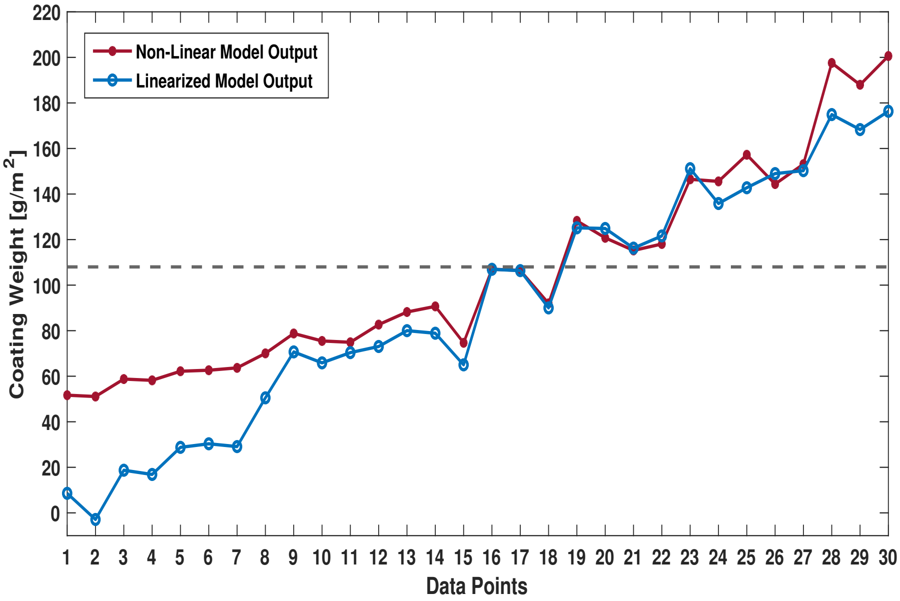

Figure 7-5: Comparison of non-linear model and linearized model around third operating point

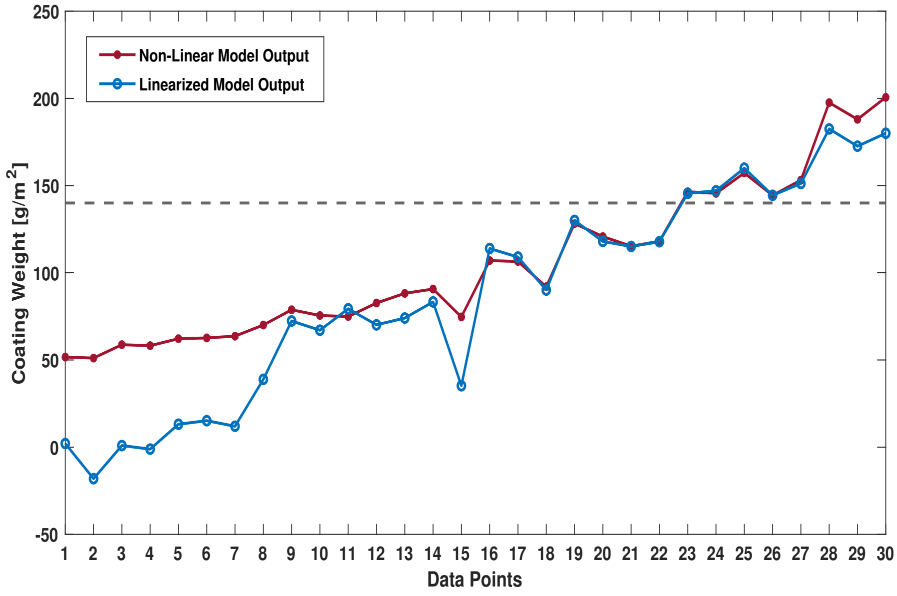

Figure 7-6: Comparison of non-linear model and linearized model around fourth operating point

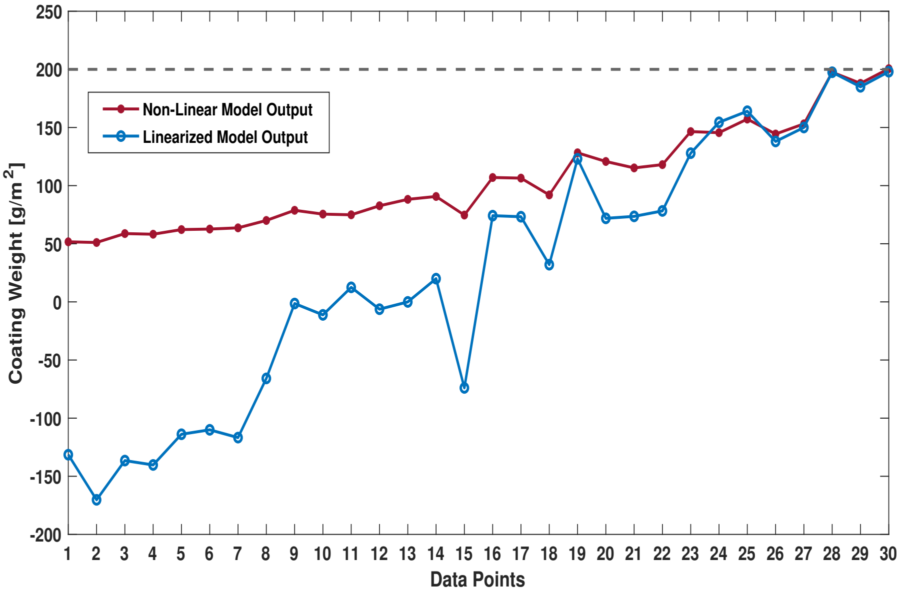

Figure 7-7: Comparison of non-linear model and linearized model around fifth operating point

It can be seen that the five aforementioned linear models appropriately describe the non-linear static coating weight model in the vicinity of the operating point. Moreover, the entire range of the coating weight (50 g/m^2 - 180 g/m^2) is taken care by the linearization. Finally, it is a matter of cascading the linear dynamics of fan with the linearized static model.

Recalling Equation 6-1, the transfer function describing the dynamics of the fan is given as:

$$\frac{\Delta P_0(s)}{\Delta P_{setpoint}(s)} = \frac{0.1142}{s^2 + 0.5405s + 0.1141} e^{-3s} \tag{7-4}$$

With the knowledge of time-delay and the linearized models obtained, the transfer from P_0 to coating weight cw_{delay} is given as:

$$\frac{\Delta cw_{delay}(s)}{\Delta P_0(s)} = \begin{cases} -0.001 \cdot e^{-76s}, & \text{First operating point.} \\ -0.002 \cdot e^{-76s}, & \text{Second operating point.} \\ -0.0044 \cdot e^{-95s}, & \text{Third operating point.} \\ -0.0048 \cdot e^{-60s}, & \text{Fourth operating point.} \\ -0.0089 \cdot e^{-74s}, & \text{Fifth operating point.} \end{cases} \tag{7-5}$$

The time delay given in the above equation corresponds to the strip speeds in the various operating points. On combining the above two transfer functions, we get five process models for different operating points as:

$$\boldsymbol{\frac{\Delta cw_{delay}(s)}{\Delta P_{setpoint}(s)} = \begin{cases} \frac{0.1142}{s^2+0.5405s+0.1141} \cdot -0.001e^{-79s} \\ \frac{0.1142}{s^2+0.5405s+0.1141} \cdot -0.002e^{-79s} \\ \frac{0.1142}{s^2+0.5405s+0.1141} \cdot -0.0044e^{-98s} \\ \frac{0.1142}{s^2+0.5405s+0.1141} \cdot -0.0048e^{-63s} \\ \frac{0.1142}{s^2+0.5405s+0.1141} \cdot -0.0089e^{-77s} \end{cases}} \tag{7-6}$$

7-3 Filter Design

Since the feedback signal (dy) in Figure 7-1 depends on the process disturbance and the noise, the statistical properties of dy are unknown. Given this fact, a proper step would be to implement a first-order low-pass filter $F(s)$ (with cut-off frequency f_c [Hz]) in the feedback loop to stop the high-frequency component going into the controller.

$$F(s) = \frac{2\pi f_c}{s + 2\pi f_c} \tag{7-7}$$

It is important to note that introducing a filter in the control loop or adjusting the cut-off frequency f_c of the filter changes the control loop's dynamic behavior. The low-pass filter must be tuned, taking into consideration the robustness and enhancing disturbance rejection properties. The air-knife wiping process involves a considerable time delay ($60s$ - $150s$), indicating that the disturbances will only be corrected once the delay has passed. This suggests that more noise must be filtered (by reducing the cut-off frequency f_c) so as not to transfer the high-frequency noise in the control input. However, on the other hand, if the cut-off frequency f_c is higher, it will result in a faster-performing control loop with better disturbance rejection properties.

Therefore, the choice of the tuning parameter f_c in the low-pass filter is based on a compromise between [43]:

- Stability, Robustness
- Fast and good disturbance rejection responses

Figure 7-8 illustrates the frequency spectrum of the process noise estimated in Section 4-4. In the air-knife wiping process, it is not recommended to have high-frequency components because they produce quick variations in the control input $P_{setpoint}$ and cause wear in the actuator. But at the same time, it is also desired to have a good disturbance rejection response. Therefore, by analyzing both the factors, an initial choice of 0.1Hz is considered for the cut-off frequency.

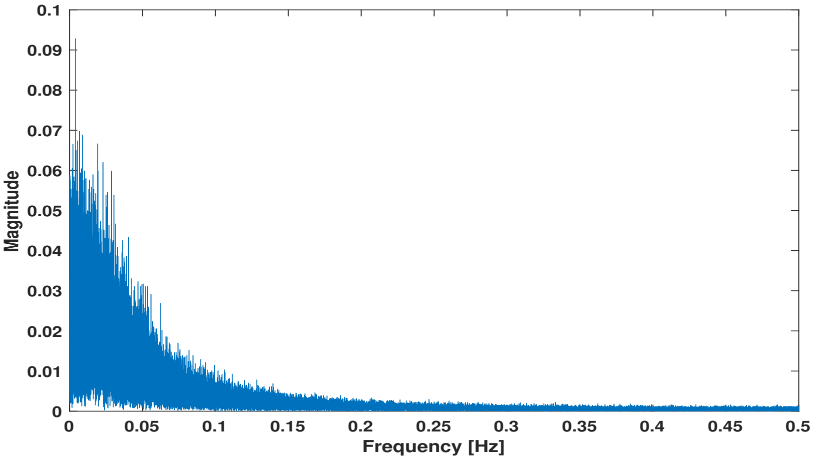

Figure 7-8: FFT of process noise

7-4 Tuning PI Controller

Stability is a key factor in the development of a feedback control system. The controller will overact when the feedback gain becomes too high to render the closed-loop system unstable. Therefore, in this section, the step response of the closed-loop and the frequency response of the loop transfer function will be used to characterize the system's performance and stability.

Let $L(j\omega)$ represent the loop transfer function. Bode's stability criterion states that "the closed-loop system is stable if and only if the loop gain $|L|$ is less than one at the phase cross over frequency" [44], that is:

$$\text{Stability} \leftrightarrow |L(j\omega_{180})| < 1 \tag{7-8}$$

where ω_{180} is the phase cross over frequency defined as $\angle L(j\omega_{180})$ = -180°. In the bode plot, the stability margins, namely gain margin (GM) and phase margin (PM), are used to determine how close to instability a stable closed-loop system is. The GM is "the factor by which the loop gain $|L(j\omega)|$ can be increased until the closed-loop system becomes unstable" [44]. The PM specifies "how much phase lag can be added to $L(s)$ at the crossover frequency ω_c before the phase at this frequency becomes $-180°$ which corresponds to closed-loop instability" [44]. The phase margin (PM) is a safeguard against time delay ambiguity.

The Smith Predictor may be configured such that if the time-delay model is correctly defined, the closed-loop response is fast. The precision of calculating the time delay has been demonstrated in Section 5-4.

To assure stability in a comparatively broader vicinity than the linearized operating points, the controller is also designed for perturbed process models with a ±10% error in the non-linear static gain and ±5% error in the time delay. For the PI controller, the tuning goal is to provide a closed-loop settling time less than 100 seconds for the nominal process model and a maximum of 20% overshoot for the perturbed model. The controllers must not be tuned aggressively; otherwise, they might become unstable when leaving its vicinity of the operating point. By adjusting the PI controller gain and integration time, it is possible to achieve the specified closed-loop requirements.

Tuning PI Controller for First Operating Point: The tuning of the controller resulted in a gain K_c of -453 and an integration time T_i of 8.31 seconds.

$$K_c \left(1 + \frac{1}{T_i s}\right) = -453 \left(1 + \frac{1}{8.31 s}\right) \tag{7-9}$$

To assess the performance of the tuned PI controller, the feedback loop is closed, and a simulation is run with the step input being applied at the reference signal (y_{sp}) and output disturbance signal (d). The step response for the nominal (blue) and perturbed (orange) process models are plotted in Figure 7-9.

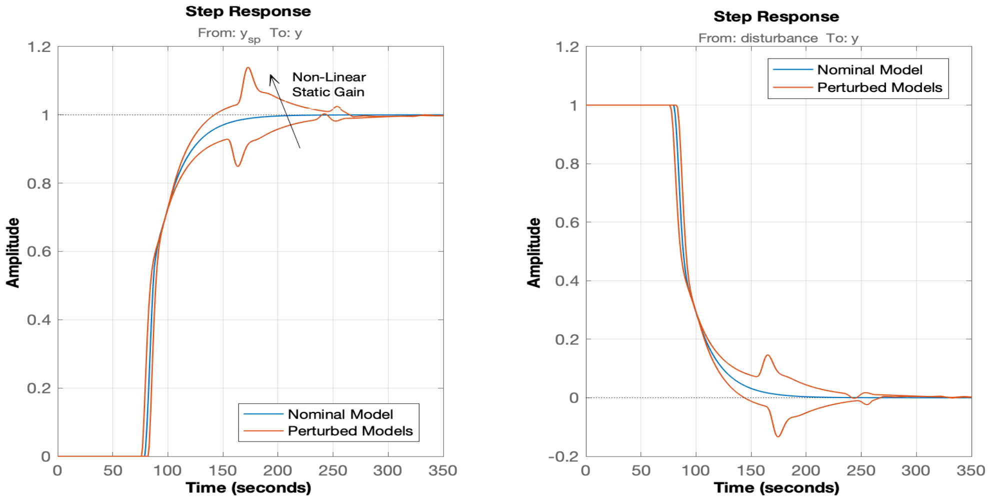

Figure 7-9: Step response

With the closed-loop step response plotted above, one can see that the controller's response is slow with a settling time of 90 seconds (excluding time delay). The settling time is defined as the time after which the output remains within ±5% of its final value. In addition to this, a 14% overshoot and 15% undershoot were calculated in the step response of the two perturbed models. To reduce the Smith Predictor's sensitivity to modeling errors, it is important to have large stability margins in the open-loop transfer function, as shown in Figure 7-10.

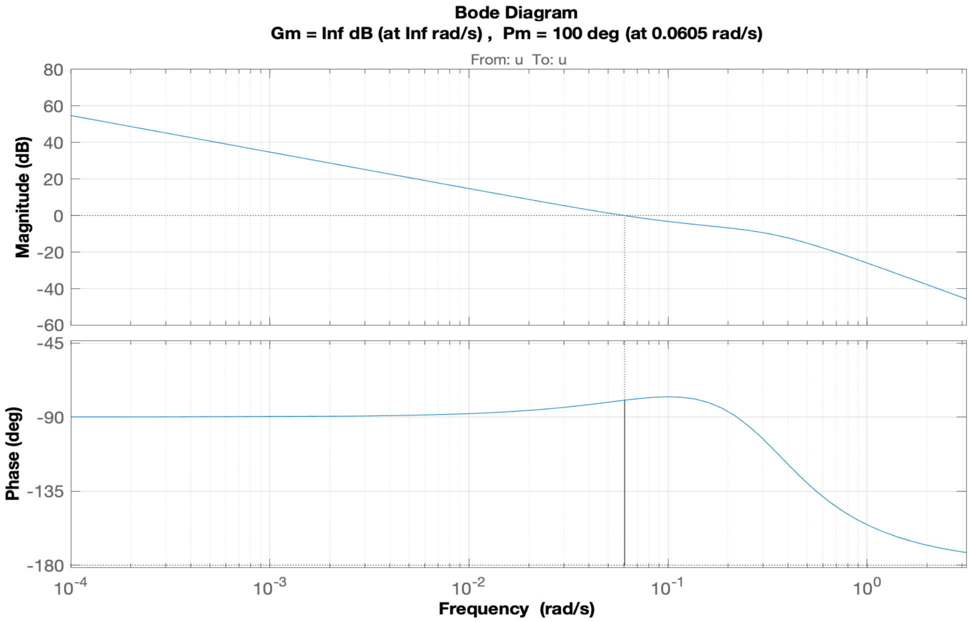

Figure 7-10: Open-loop Bode Plot

The open-loop has ample gain and phase margin. So, the emphasis now is on the open-loop transfer function from y_{sp} to dp with the inner loop closed. This time, a perturbed model with a 10% error in non-linear static gain and a 5% error in time delay was chosen as the process model to provide a deeper insight into the stability margins. In Figure 7-11, the stability margins obtained for the loop transfer function from ysp to dp are provided.

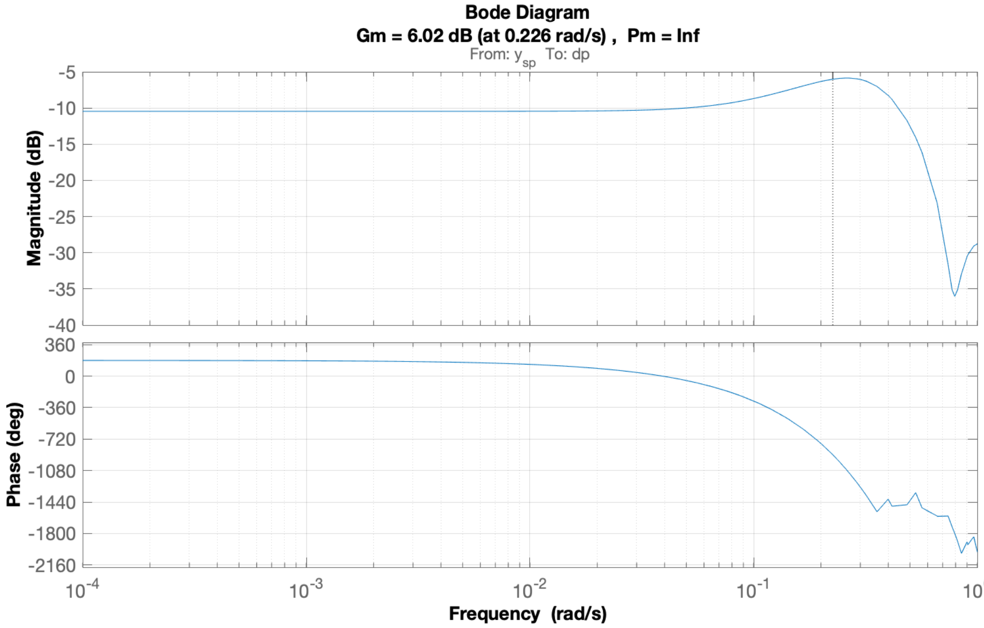

Figure 7-11: Outer open-loop Bode plot

The open-loop transfer function from y_{sp} to dp has sufficient gain and phase margin for the mismatched model. However, in the magnitude plot, a hump is observed at 0.226 rad/s that reduces the gain margin. To address this problem, the filter's cut-off frequency must be lowered until it rolls off before 0.226 rad/s ($\approx 0.03Hz$). After various iterations, a low-pass filter with a cut-off frequency of $0.02Hz$ was chosen. Figure 7-12 verifies that the gain margin has improved near 0.226 rad/s phase crossing.

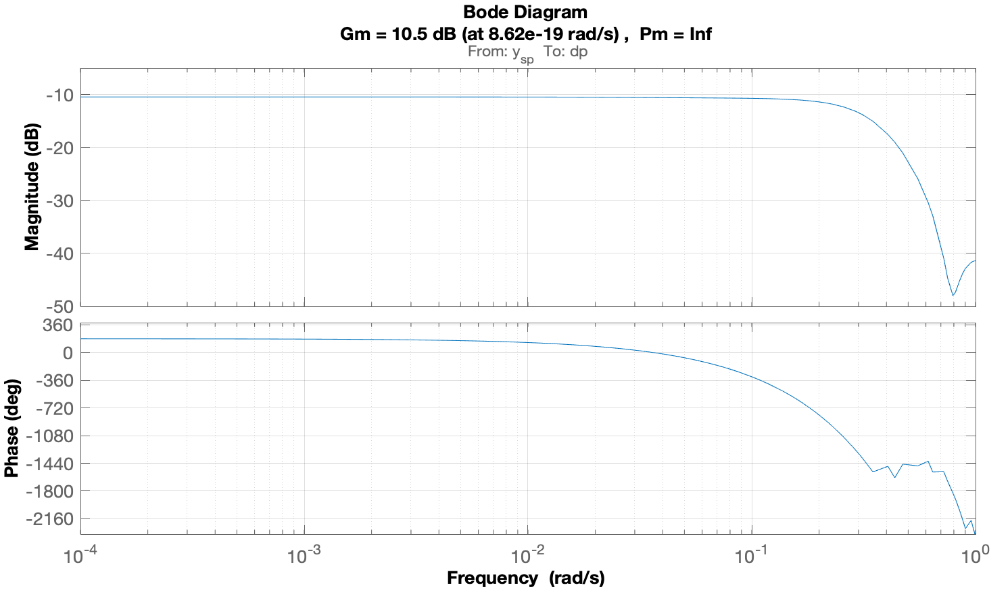

Figure 7-12: Outer open-loop Bode plot with modified filter

Finally, the closed-loop step response for the nominal and perturbed models are plotted in Figure 7-13. The findings are contrasted with the different low pass filter cut-off frequencies.

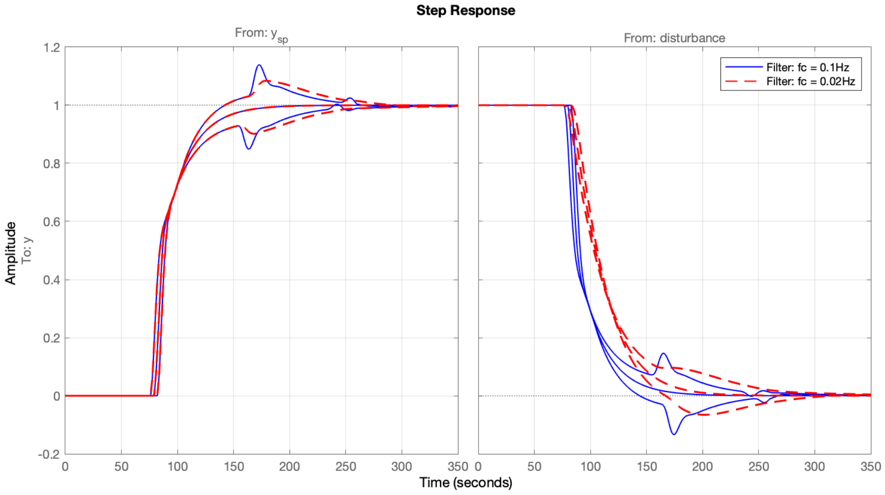

Figure 7-13: Step response for mismatched models with different filter

It can be seen that the filter with a cut-off frequency of $0.02 Hz$ provides an almost consistent performance with less noise getting transferred to the input at the cost of a slightly slower response to the disturbance.

Tuning PI Controller for Other Operating Points: The PI controllers for other operating points were tuned similarly as that for the first operating point. The loop transfer function bode plot and the step responses for all the tuned PI controllers can be found in Appendix C. The tuning parameters: controller gain, K_c, and integration time, T_i obtained for all the operating points are shown in Table 7-1.

Table 7-1: Result of tuning PI controllers for different operating points

Operating Point	Controller Gain, K_c	Integration Time, T_i
1	-453	8.31
2	-172	8.00
3	-135	8.43
4	-150	9.87
5	-75	9.37

The two important characteristics used to evaluate the performance are closed-loop settling time with the nominal model and the undershoot/overshoot for the closed-loop with the perturbed model. The settling time evaluates the response speed, whereas undershoot/overshoot are related to the quality of the response [44]. Table 7-2 indicates both the performance specification for the previously tuned PI controllers at different operating points.

Table 7-2: Comparison of performance specification for different operating points

Operating Point	Settling Time [sec]	Undershoot [%]	Overshoot [%]
1	90	12	11
2	98	15	15
3	94	17	20
4	92	15	17
5	89	18	18

7-5 Simulations

In this section, the control achieved from closed-loop simulations of the non-linear coating weight process is studied. Most of the time, the production data from the coating process includes only steady-state operating conditions, and for the remaining time, it is subjected to different variations. Two main objectives to design the controller are reference tracking and disturbance rejection. The Controller's performance is tested with a data set that includes transient operation with variations in the process variables.

The simulation is performed with data for a production period of 2000 seconds ($\approx$ 33 minutes). The process variables for this production time are presented in Figure 7-14. The strip speed V_s can be seen varying significantly throughout the production period. Furthermore, the strip-to-knife distance (Z) is also not steady for this production period. A step-change in the target coating weight from 50 g/m^2 to 113 g/m^2 is observed at t = 1266 seconds. These variations in the process variables yield the possibility of evaluating the controller's performance for non-steady operating conditions.

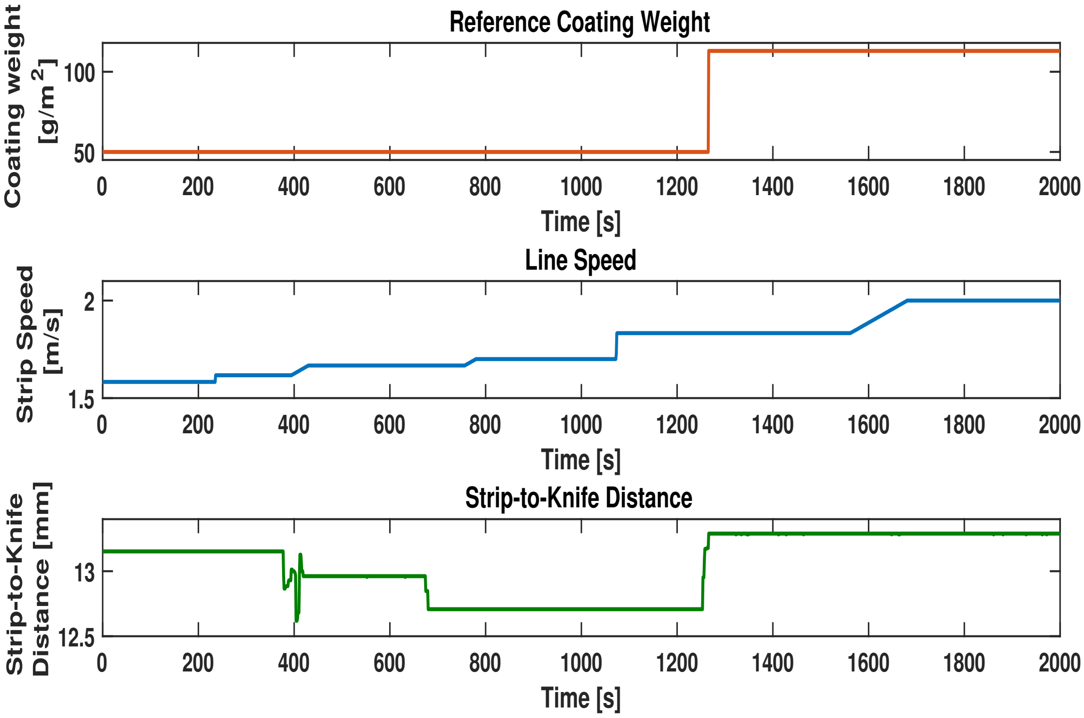

Figure 7-14: Production data for simulation

The non-linear coating weight model developed in Section 6-3 represents the zinc coating process. With the intention to be able to reach the target coating weight of 113 g/m^2 and achieve desired closed-loop specifications, the PI controller tuned for the third operating point must be used i.e., with the controller gain K_c = -135 and integration time T_i = 8.43 seconds. In the interest of evaluating the controller's performance, particularly the settling time, a simulation is performed with no noise present in the process model. According to the production data used for this simulation, the step increase of 0.13 m/s in the strip speed at t = 1073 seconds can be seen as a measured disturbance. Apart from that, a step of 5 g/m^2 is given as a load disturbance at t = 450 seconds so as to examine the disturbance rejection properties. Figure 7-15 shows the response of the coating process when the reference coating weight and the process variables shown in Figure 7-14 were applied to the system. In order to analyze the results better, a dotted line is plotted in Figure 7-15 to represent the time of reference change after the time delay. The settling time for the response is calculated to be 64 seconds (excluding time delay). Moreover, a slow disturbance rejection response can be observed for the step-change in the strip speed at t = 1073 seconds. As expected, the system recovers slowly from the load disturbance only after the time delay has passed. In the next step, the noise is added back in the process, and the simulation is carried out once again. Figure 7-16 shows the response of the system with noise in the process model.

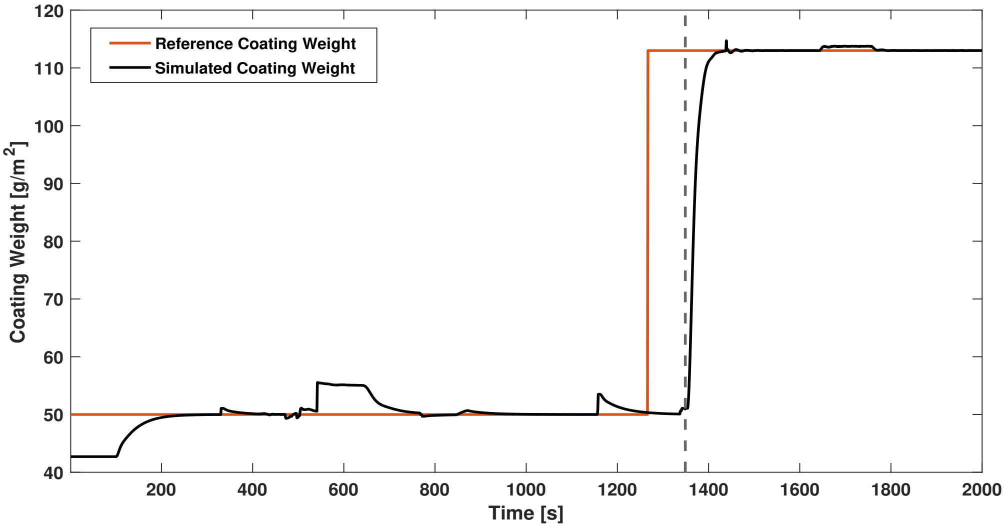

Figure 7-15: Simulated coating weight response without noise

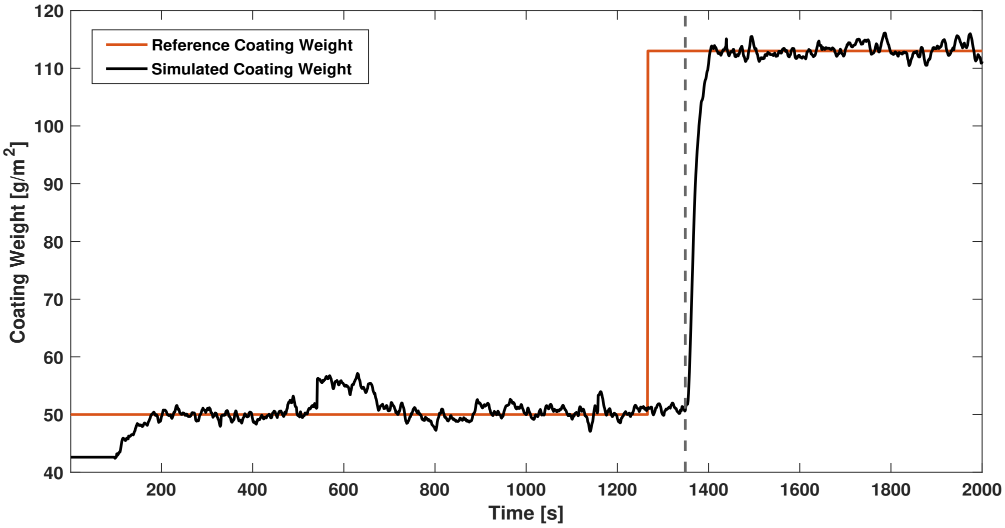

Figure 7-16: Simulated coating weight response with noise

One can see that the system is able to track the reference trajectory. Furthermore, the system is able to recover from both the measured and load disturbances but with a slow response. The control input $P_{setpoint}$ obtained from the PI controller is plotted in Figure 7-17. Because of the low-pass filter, no quick variations are observed in the control input.

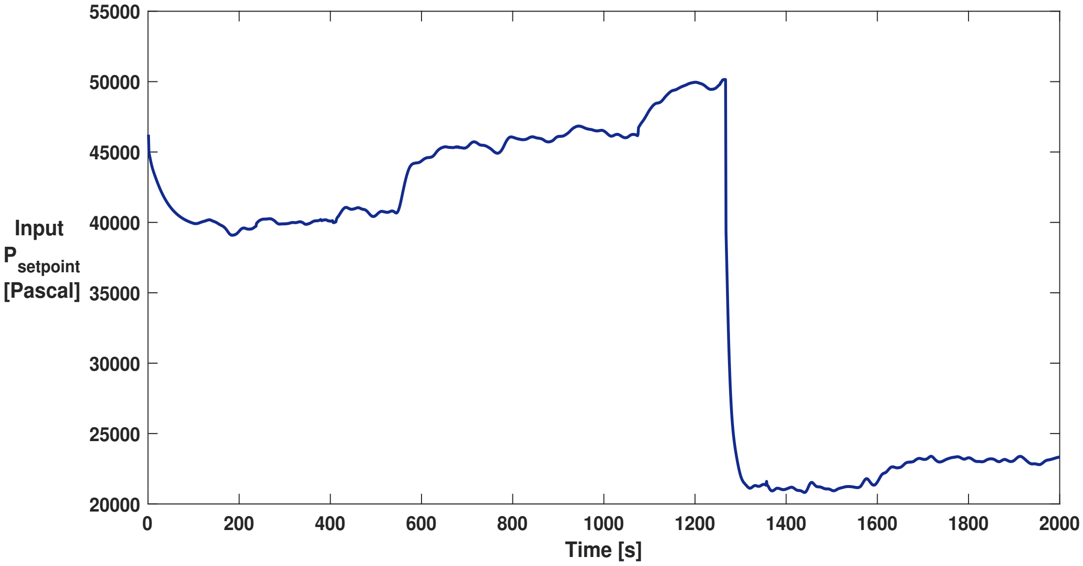

Figure 7-17: Control input $P_{setpoint}$

7-6 Conclusion

The PI controller was tuned for five operating points considering the non-linearity and the vast operating range of the zinc-coating process. To to be able to meet the necessary closed-loop specifications, the controller gains must be chosen in accordance with the correct operating point.

The closed-loop simulations were used to evaluate the performance of the controller during transient operation in the coating process. The settling time of the response to a reference change in input was calculated to be 64 seconds (excluding time delay). However, no overshoot was observed in the closed-loop response. As a consequence of the significant time delay, the response of the system to the load disturbance was observed to be slow.

Chapter 8

Nonlinear Extended Prediction Self-Adaptive Control

8-1 Introduction

As the time delays have been prominent in many scientific areas, there is an increasing interest in the field of control engineering [37, 40]. Transport time delays make control of the process difficult [35].

As discussed in Chapter 7, the most popular dead-time compensation strategy used in the industry is the Smith predictor. However, the system's response with the PI controller was perceived to be sluggish with a considerable amount of settling time. Moreover, the controller had to be tuned for various operating points as the range of all the process variables was too extensive.

This chapter deals with applying an advanced control technique that uses prediction of the future plant output to determine optimum future control inputs. With all the knowledge available about the process dynamics, it is possible to use such an advanced control strategy. This approach comes under the family of Model Predictive Control (MPC) methods.

There are various MPC algorithms that vary in the model used to describe the process and the noise, as well as the cost function to be minimized [35]. One of the algorithms termed as **Extended Prediction Self-Adaptive Control (EPSAC)** has been used with success to account for the time delays, and the ability to handle non-linear systems [12, 45]. In recent years, the EPSAC algorithm has been quite prominent in the industry, and some of the examples can be found in [9, 17, 21, 40].

8-2 Methodology

All the MPC based algorithms, including EPSAC, have the objective to find the optimal control input, which depends on the prediction of the model output. It is computed by optimizing a cost function over a certain horizon, called the prediction horizon N_2. Compared to different MPC algorithms, EPSAC considers the prediction of the model output $y(t+k)$ from two contributions: a term $y_{base}(t+k)$ that does not depend on the future control input and a term $y_{opt}(t+k)$ that does depend on the future control inputs [40].

$$\boldsymbol{y(t+k|t) = y_{base}(t+k|t) + y_{opt}(t+k|t)} \quad k = 1, ..., N_2 \tag{8-1}$$

1. $\boldsymbol{y_{base}(t+k|t)}$ is the basic output that derives from the former control inputs $[u(t-1), u(t-2), u(t-3), ...]$. Such inputs have already been introduced to the process and thereby, their impact on the output can be estimated based on the process model and its state $[x(t-1), x(t-2), x(t-3), ...]$ [45]. As the process has a substantial amount of time delay, various previous inputs may have to be considered. The basic future control scenario $[u_{base}(t+k|t), k = 0, .., N_u - 1]$, which is the postulated sequence of inputs (to be initialized by EPSAC) would also have an impact on $y_{base}(t+k|t)$. Additionally, $y_{base}(t+k|t)$ also includes the influence of the estimated noise and disturbances $d(t|t)$.
2. $\boldsymbol{y_{opt}(t+k|t)}$ is the consequence of future optimizing control inputs $[\delta u(t+k|t), k = 0, .., N_u - 1]$ with $\delta u(t+k|t) = u(t+k|t) - u_{base}(t+k|t), k = 0, ..., N_u - 1$. The design parameter N_u is the control horizon. $y_{opt}(t+k|t)$ can be represented as a discrete-time convolution of impulse response coefficients $h_1, h_2, .., h_k, .., h_{N_2}$ and step response coefficients $g_1, g_2, .., g_k, ..g_{N_2}$ of the system as shown in Equation 8-2 [13, 20].

$$\begin{aligned} y_{\mathrm{opt}}(t+k|t) = h_k \delta u(t|t) + h_{k-1} \delta u(t+1|t) + \ldots + h_{k-N_u+2} \delta u(t+N_u-2|t) \\ + g_{k-N_u+1} \delta u\left(t+N_u-1|t\right) \end{aligned} \tag{8-2}$$

The future sequence of control inputs is a solution to the problem of optimization given by:

$$\min_{u(t|t)...u(t+N_u-1|t)} J, \qquad J = \sum_{k=N_1}^{N_2-1} [r(t+k|t) - y(t+k|t)]^2 + \lambda \sum_{j=0}^{N_u-1} [u(t+j|t)]^2 \tag{8-3}$$

where,

- $y(t+k|t)$: future process output
- $r(t+k|t)$: reference/setpoint
- λ : weighting parameter
- N_u : Control Horizon
- N_1 : Time Delay
- N_2 : Prediction Horizon

With this cost function, the divergence of the process output from the target trajectory and the control effort is taken into account. λ is known as the weighting parameter that specifies the emphasis of the control effort relative to divergence of the process output from the target trajectory. In the coating weight control, there is no need to penalize the control effort.

Instead, it makes more sense to penalize the increment in the control effort. Therefore, the cost function is modified as follows:

$$\min_{u(t|t)\ldots u(t+N_u-1|t)} J, \qquad J = \sum_{k=N_1}^{N_2-1} [r(t+k|t) - y(t+k|t)]^2 + \lambda \sum_{j=0}^{N_u-2} [u(t+j+1|t) - u(t+j|t)]^2 \quad (8\text{-}4)$$

Only the first component of the future control input shall be applied to the process in a receding horizon system. The remainder of the input sequence is omitted, and at the next time instant, the entire optimization process is carried out again. For a process with time-varying delay, the output predictions in the cost function for determining the optimum control sequence must be regarded only after the delay. Therefore, N_1 must be picked equivalent to the time-delay [40, 45].

Among all the tuning parameters, there is also N_u, known as the control horizon. It plays an important role in defining the structure of the future control inputs $[u(t+k|t), k = 1, .., N_u]$. Essentially, N_u control inputs must be postulated, providing as many degrees of freedom as the number of control inputs in the sequence. With $1 \leq N_u \leq N_2$, the control input remain constant after N_u. Figure 8-1 illustrates the concept of EPSAC for a control horizon $N_u = 4$. With the sampling time of one second and a delay of three seconds in the fan dynamics, the best possible choice for the control horizon would be $N_u = N_2 - 3$.

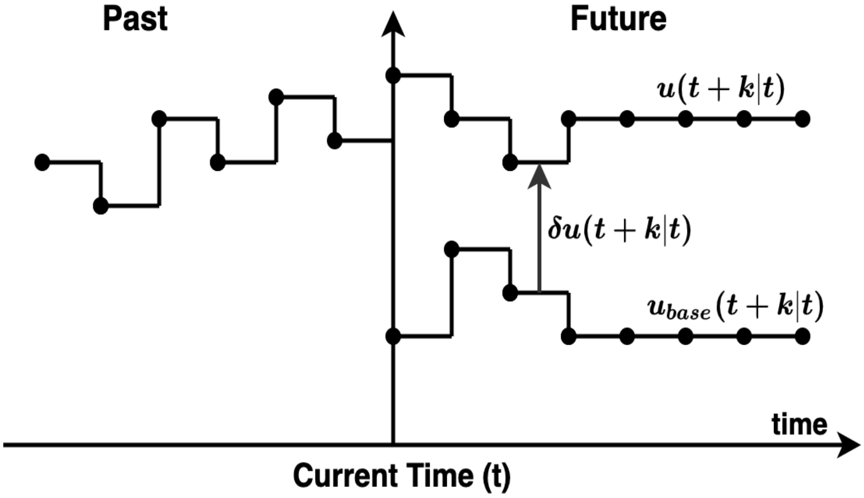

Figure 8-1: EPSAC concept for $N_u = 4$

The concept of two contributors (y_{base} and y_{opt}) in the prediction output, as shown in Equation 8-1 is actually true only for linear systems since it is based on superposition principle. Nevertheless, an improvement has been introduced for non-linear systems: the optimizing control sequence is determined iteratively at each sampling instant, by modifying the basic future control scenario u_{base} in a manner that the optimizing control increments δu_{opt} gradually go to zero. In this way, the basic control scenario u_{base} converges to the optimal solution, and the superposition principle will no longer be involved [20]. This new version, known as the **Non-linear Extended Prediction Self-Adaptive Control (NEPSAC)**, is primarily distinguished with its relative easiness, as it involves repetitive usage of the standard linear EPSAC technique during the controller's sampling time.

For the basic future control selection $u_{base}(t+k|t)$, it is necessary to make reasonable initial guess in order to restrict the number of iterations and hence the computational time. The previously implemented optimal control input is a straightforward yet efficient preference, i.e., $u_{base}(t+k|t) \equiv u(t+k|t-1)$ [45].

For the model output, a parallel structure resulting in the Smith predictor scheme, as shown in Figure 8-2 is implemented. This model is used for estimating the disturbance and the noise, which collects all effects in the measured output that are not present in the model itself. At each sampling instant, an initial condition $x_0(t|t)$ is provided to the NEPSAC controller. The future prediction model consists of the non-linear air-knife model without the time-varying delay model.

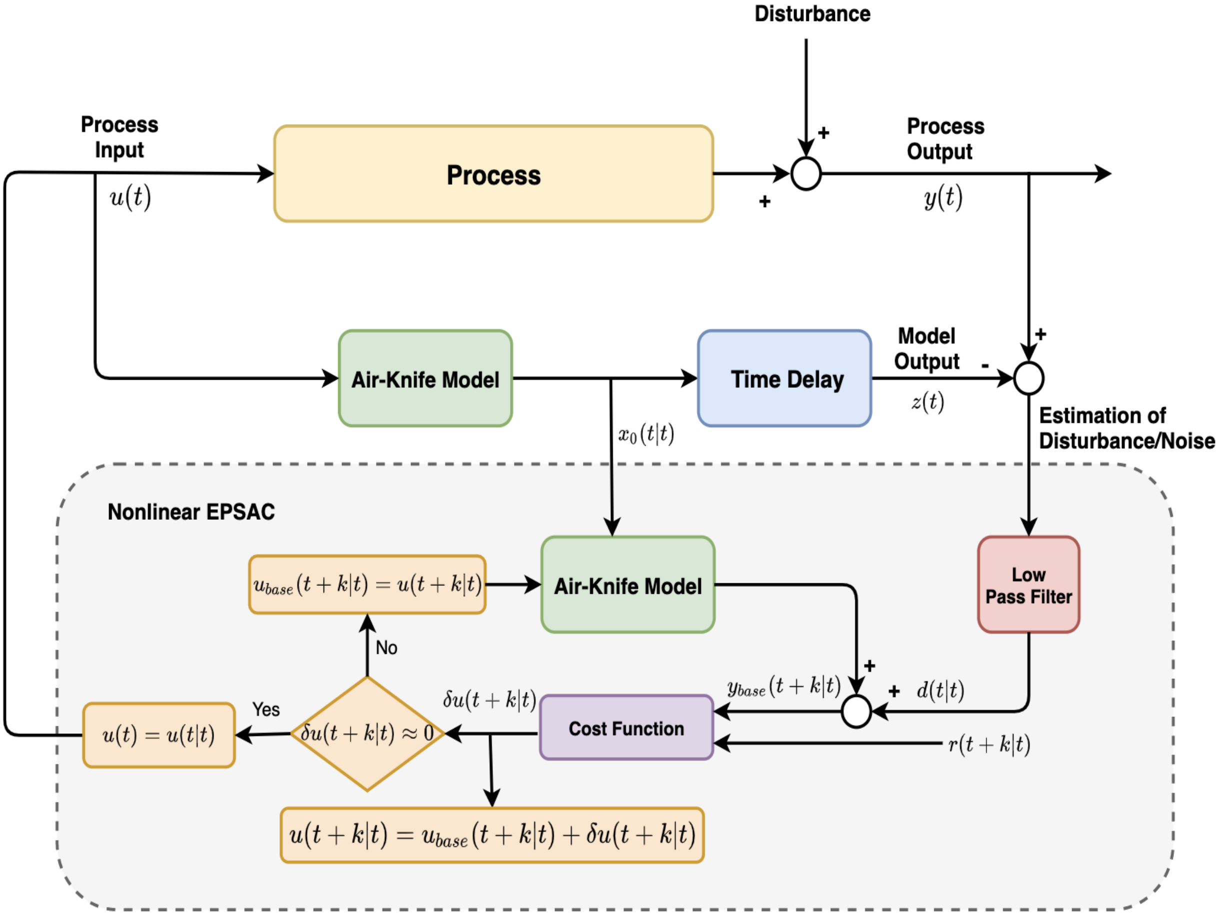

Figure 8-2: Closed-loop control layout of the zinc coating process

For implementing NEPSAC, the next step is to predict the future process output. At each sampling instant, predictions for future model output are made based on the postulated basic input sequence u_{base} and the current state of the system. Using the control loop layout for Non-linear Extended Prediction Self-Adaptive Control (NEPSAC), as shown in Figure 8-2, the procedure to predict the future process output is rigorously simplified. Moreover, when using this structure, N_1 in the optimization problem (Equation 8-4) need not include the transport delay, and therefore, it can be set equal to the constant delay present in the fan dynamics, i.e., $N_1 = 3$.

The prediction horizon N_2 is also an important parameter affecting the controller's performance. It determines for how many numbers of prediction points the cost function will be minimized to calculate the optimum future control inputs. In general, there is no rule for selecting the value of N_2, but if the value of N_2 is picked too small, very little information regarding the process is supplied to the controller, and only a few samples are optimized in the cost function. On the other side, if the value of N_2 is too large, it will unnecessarily increase the computational load for the optimization problem. The best choice of N_2 must be such that the system's transient behavior is involved in the cost function for determining the optimum future control sequence.

Figure 8-2 illustrates the combination of Smith's predictor with NEPSAC being implemented to control the coating weight in the hot-dip galvanizing process. In conclusion, the procedure can be carried out iteratively by running over the following steps at each sampling time:

1. Initialize the basic future control input $u_{base}(t+k|t)$ to the previously applied optimal control input i.e. $u(t+k|t-1)$.
2. Determine the future optimization control actions $u(t+k|t)$ using the optimization mentioned in Equation 8-4. Moreover, optimizing control increments are calculated by $\delta u(t+k|t) = u(t+k|t) - u_{base}(t+k|t), k = 0, ..., N_u - 1$.
3. Compare $u(t+k|t)$ to $u_{base}(t+k|t)$
    - If the change is not small enough, reformulate $u_{base}(t+k|t)$ as $u_{base}(t+k|t) + \delta u(t+k|t)$ and go back to Step 2.
    - If the change is within a specified tolerance, $u(t+k|t) = u_{base}(t+k|t) + \delta u(t+k|t)$ is the optimal control for the current sampling instant.

The algorithm post-convergence results in optimum control for a specified non-linear process. The number of iterations needed in each sampling interval relies on how far the optimum control is from its prior value [13].

The results from the various applications of NEPSAC show that this method performs very well as long as the process model is identified accurately. The controller might lose performance if there are some unmodelled dynamics during the transport of the zinc coating from the air-knives to the cold-coating gauge. This control strategy also offers a lot of tuning knobs, which can be adapted according to the process needs.

On comparing NEPSAC with standard MPC approach, it simplifies the optimization procedure by replacing the non-linear optimization with **iterative quadratic programming** [40]. In this chapter, results from the NEPSAC method will also be compared with the PI controller in Smith Predictor.

8-3 Problem Framework

In this section, a brief formulation of the air-knife model used by NEPSAC is described. The state-space representation of the model is given by Equation 8-5. It is important to clarify that, NEPSAC in general, can be used for controlling non-linear dynamical processes as well.

$$\begin{aligned} \dot{x}(t) &= Ax(t) + Bu(t) \\ y(t) &= f\left(x(t), w(t)\right) \end{aligned} \tag{8-5}$$

where, $x(t)$ is the state vector, $u(t)$ is the input ($P_{setpoint}$), $w(t)$ are the measured disturbances (V_s and Z), $y(t)$ is the output of the system (cw), and f is the static non-linear function that depends on the air-knife wiping pressure P_0 and the measured disturbances V_s and Z ($w(t)$) to calculate the coating weight. A and B are the state matrix and input matrix respectively. It is worth mentioning that the three-second delay in the fan dynamics will be directly introduced in the discrete-time matrices.

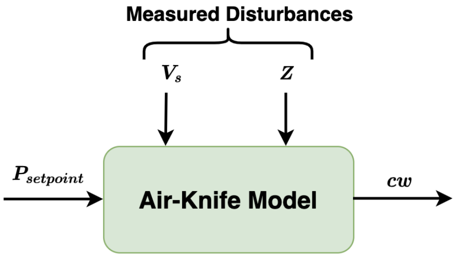

Figure 8-3: Air-Knife Model

As discussed, the NEPSAC method considers the model output $y(t+k|t)$ over the prediction horizon (N_2) from two contributions $y_{base}(t+k|t)$ and $y_{opt}(t+k|t)$. Likewise, the optimized future control input $u(t+k|t)$ is determined over the control horizon (N_u) from the summation of $u_{base}(t+k|t)$ and $\delta u(t+k|t)$.

$$\begin{aligned} y(t+k|t) &= y_{base}(t+k|t) + y_{opt}(t+k|t) \qquad k = 1, ..., N_2 \\ u(t+k|t) &= u_{base}(t+k|t) + \delta u(t+k|t) \qquad k = 0, ..., N_u - 1 \end{aligned} \tag{8-6}$$

As a first step, the basic output $y_{base}(t+k|t)$ is determined from the non-linear system model based on the initially guessed basic future control input sequence $u_{base}(t+k|t)$, the initial state $x_0(t|t)$, and the estimated noise/disturbance $d(t|t)$. Next step is to compute the future optimizing incremental control input $\delta u(t+k|t)$ over the control horizon (N_u) using the optimization problem mentioned in Equation 8-4. Using Equation 8-6, the optimization problem can be rewritten as:

$$\begin{aligned} \min_{\delta u(t|t) \dots \delta u(t+N_u-1|t)} J, \qquad J = \sum_{k=N_1}^{N_2-1} \left[r(t+k|t) - y_{base}(t+k|t) - y_{opt}(t+k|t)\right]^2 \\ + \lambda \sum_{j=0}^{N_u-2} \left[(u_{base}(t+j+1|t) + \delta u(t+j+1|t)) - (u_{base}(t+j|t) + \delta u(t+j|t))\right]^2 \end{aligned} \tag{8-7}$$

As already mentioned, $y_{opt}(t+k|t)$ is the result from the future optimizing incremental control inputs $\delta u(t+k|t)$. For linear systems, $y_{opt}(t+k|t)$ can indeed be represented as a discrete-time convolution of impulse response coefficients and step response coefficients of the system, as shown in Equation 8-2. However, this will not be valid for non-linear systems, and therefore, one possible solution to calculate $y_{opt}(t+k|t)$ is through local linearization. In other words, the air-knife model will be linearized around an operating point $(u_{base}(t), x_{base}(t), w_{base}(t))$ at every iteration over the prediction horizon N_2.

For simplicity, let's define $\delta x(t) = x(t) - x_{base}(t)$. The state equation in the state-space description is linear, and therefore, can be rewritten as following once at the operating point.

$$\dot{\delta x(t)} = A\delta x(t) + B\delta u(t) \tag{8-8}$$

The output equation in the state space description given by Equation 8-5 is linearized around the operating point as following:

$$\begin{aligned} y(t) \approx f\left(x_{base}(t), w_{base}(t)\right) + \left.\frac{\partial f}{\partial x}\right|_{x_{base}(t), w_{base}(t)} &(x(t) - x_{base}(t)) \\ + \left.\frac{\partial f}{\partial w}\right|_{x_{base}(t), w_{base}(t)} &(w(t) - w_{base}(t)) \end{aligned} \tag{8-9}$$

From the first-order Taylor expansion the time-varying matrix $C(t)$ and $D_w(t)$ are obtained, given by:

$$C(t) = \left.\frac{\partial f}{\partial x}\right|_{x_{base}(t), w_{base}(t)} \qquad D_w(t) = \left.\frac{\partial f}{\partial w}\right|_{x_{base}(t), w_{base}(t)} \tag{8-10}$$

Since the model is linearized around an operating point, an additional offset term appears in the state space. The offset term $f\left(x_{base}(t), w_{base}(t)\right)$ is equal to the basic output $y_{base}(t)$. Therefore, the output equation can then be rewritten as:

$$y(t) = y_{base}(t) + C(t)(\delta x(t)) + D_w(t)(w(t) - w_{base}(t)) \tag{8-11}$$

At each iteration, the model is linearized around $w_{base}(t) = w(t)$, thereby, removing the term $D_w(w(t) - w_{base}(t))$ from the state space representation.

$$\begin{aligned} \dot{\delta x(t)} &= A\delta x(t) + B\delta u(t) \\ y_{opt}(t) &= C(t)\delta x(t) \end{aligned} \tag{8-12}$$

Based on the discrete-time state-space, the next step is to have the predictions $y_{opt}(t+k|t)$ over the length of prediction horizon N_2. From this point, the discrete-time state matrix A_d and input matrix B_d given by Equation 6-9 will be used.

$$\begin{aligned} y_{opt}(t+1|t) &= C(t+1|t)\delta x(t+1|t) \\ &= C(t+1|t)\left(A_d\delta x(t|t) + B_d\delta u(t|t)\right) \\ &= C(t+1|t)A_d\delta x(t|t) + C(t+1|t)B_d\delta u(t|t) \end{aligned}$$

$$\begin{aligned} y_{opt}(t+2|t) &= C(t+2|t)\delta x(t+2|t) \\ &= C(t+2|t)\left(A_d\delta x(t+1|t) + B_d\delta u(t+1|t)\right) \\ &= C(t+2|t)\left(A_d\left(A_d\delta x(t|t) + B_d\delta u(t|t)\right) + B_d\delta u(t+1|t)\right) \\ &= C(t+2|t)A_d^2\delta x(t|t) + C(t+2|t)A_dB_d\delta u(t|t) + C(t+2|t)B_d\delta u(t+1|t) \end{aligned}$$

Extending the predictions until the prediction horizon N_2, the following result is obtained:

$$\begin{aligned} y_{opt}(t+N_2|t) &= C(t+N_2|t)\delta x(t+N_2|t) \\ &= C(t+N_2|t)A_d^{N_2-1}\delta x(t|t) + C(t+N_2-2|t)A_d^{N_2-1}B_d\delta u(t|t) + \\ &\quad \cdots + C(t+N_2|t)\left(A_d^{N_k} + A_d^{N_k-1} + \cdots + 1\right)B_d\delta u(t+N_u-1|t) \end{aligned}$$

where, $N_k = N_2 - N_u$. At each iteration, the model is linearized around $x_{base}(t|t) = x(t|t)$, thereby, removing the term $\delta x(t|t)$ from all the prediction equations of $y_{opt}(t+k|t)$. Hence, $y_{opt}(t+k|t), k = 1,..,N_2$ is calculated from the future optimizing incremental control input $\delta u(t+k|t), k = 0,..,N_u-1$ by a prediction matrix G such that:

$$y_{opt}(t+k|t) = G \cdot \delta u(t+k|t) \tag{8-13}$$

where,

$$G = \begin{bmatrix} C(t+1|t)B_d & 0 & \cdots & 0 \\ C(t+2|t)A_dB_d & C(t+2|t)B_d & \cdots & 0 \\ \vdots & & & \vdots \\ C(t+N_u|t)A_d^{N_u-1}B_d & \cdots & \cdots & C(t+N_u|t)B_d \\ C(t+N_u+1|t)A_d^{N_u}B_d & \cdots & \cdots & C(t+N_u+1|t)(A_d+1)B_d \\ \vdots & & & \vdots \\ C(t+N_2|t)A_d^{N_2-1}B_d & \cdots & \cdots & C(t+N_2|t)(A_d^{N_k} + A_d^{N_k-1} + .. + 1)B_d \end{bmatrix}_{N_2 \times N_u}$$

Substituting Equation 8-13 into the optimization problem given by Equation 8-7, the cost function becomes a function of $\delta u(t+k|t), k = 0,..,N_u-1$. Hence, the non-linear optimization is replaced by iterative quadratic programming. The iterative NEPSAC algorithm results in convergence to the optimum input for the non-linear process.

Handling Constraints The NEPSAC method also has the ability to handle system constraints by solving constrained optimization problems. The input $P_{setpoint}$ is regulated by the air-knives, and it has a minimum and maximum operating value as 0 [Pascal] and 60000 [Pascal] respectively.

$$0 \leq u \leq 60000 \tag{8-14}$$

$$0 \leq u_{base} + \delta u \leq 60000$$

With δu as the optimization variable, the constraints in the optimization routine is given as:

$$-u_{base} \leq \delta u \leq 60000 - u_{base} \tag{8-15}$$

These linear inequalities define the feasibility region of the optimization problem, and they can be easily handled with the quadratic programming optimization framework.

Stopping Criterion In the NEPSAC method, the optimizing control sequence δu is determined in an iterative manner, by adapting the basic future control scenario u_{base} so that the optimizing control increments gradually go to zero. Ideally, all the iterations must be completed in a sampling interval. Therefore, it is necessary to define a stopping criterion for the iterations. After performing various simulations, a choice was made to terminate the iterations once δu is less than 100 Pascal (1 mbar). It turns out that a maximum of 4-5 iterations are required in order to converge to an optimum solution. Furthermore, when δu is less than 100 Pascal, it hardly has any influence on the coating weight.

8-4 Simulations

In this section, the control achieved from closed-loop simulations of the non-linear coating weight process is studied. The two main control objectives defined to design the controller remain the same as before: reference tracking and disturbance rejection. The performance of the Smith predictor with NEPSAC is examined with the same data set that was used for the PI controller. The simulation is carried out with the production data shown in Figure 7-14 for a duration of 2000 seconds ($\approx$ 33 minutes). The data includes transient operation with multiple variations in the process variables.

As already mentioned, it is not desirable to have high-frequency components in the control input $P_{setpoint}$ and instead have a more steady operation so as to avoid wear in the actuator. Therefore, the low pass filter with cut-off frequency $f_c = 0.02Hz$ is used to have a fair comparison between the NEPSAC and PI controller in the Smith predictor structure. In order to investigate the influence of various tuning parameters on the performance of the controller, the simulations are performed with no noise in the process model.

8-4-1 Influence of weighting Parameter

In the cost function given by Equation 8-7, the weighting parameter λ penalizes the increment in the control input compared to the process output deviation. With the purpose of having a steady-state input, it is essential to penalize the control input increment. In this sub-section, the influence of the weighting parameter on the control input and the coating weight response is analyzed. Moreover, the other tuning parameters, such as the prediction horizon (N_2) and the control horizon (N_u) must be kept constant in order to study the effect of the weighting parameter independently. For these simulations, the prediction horizon of 20 seconds and a control horizon of 17 seconds is chosen.

Figure 8-4 and Figure 8-5 illustrate the control input $P_{setpoint}$ and the coating weight response (during transient operation) achieved with different values of the weighting parameter. In order to analyze the results better, a dotted line is plotted in Figure 8-5 to represent the time of reference change after the time delay. With $\lambda = 0$, there is no penalty on the increment of control input, and therefore, a steady operation is not achieved. However, with $\lambda = 5 \times 10^{-6}$, steady input is accomplished in addition to the process output following the desired trajectory. With $\lambda = 5 \times 10^{-2}$, the increment in control input is penalized to a greater extent such that a slow coating weight response is seen in Figure 8-5. Therefore, $\lambda = 5 \times 10^{-6}$ seems to be a reasonable choice for the simulations.

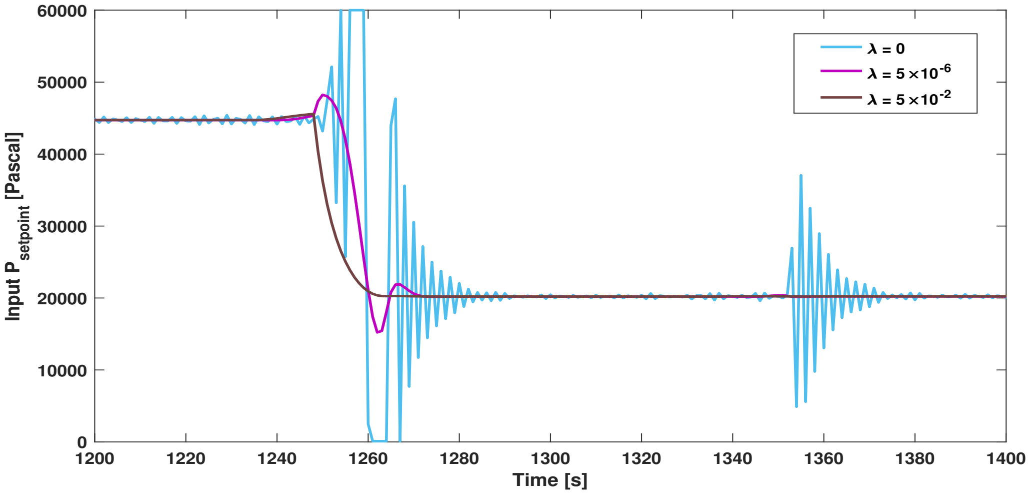

Figure 8-4: Influence of weighting parameter on control input $P_{setpoint}$

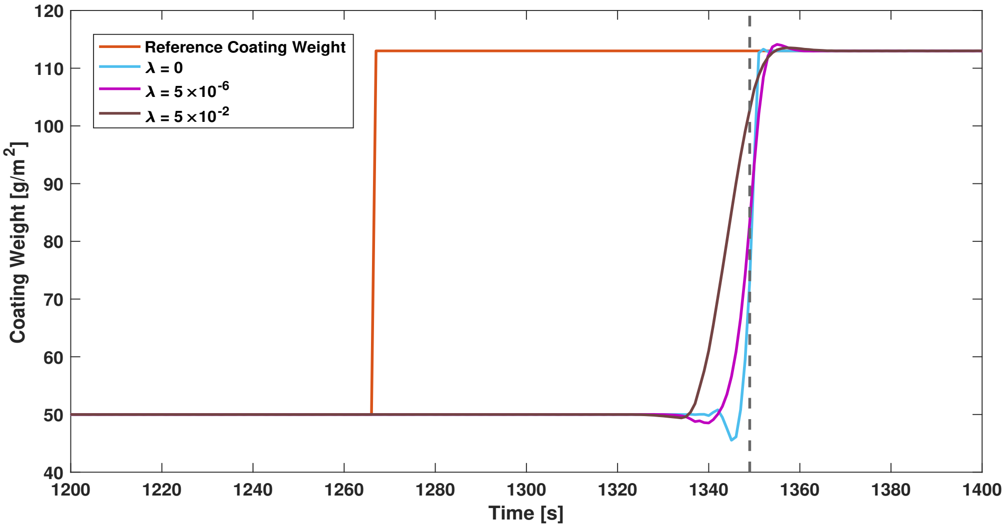

Figure 8-5: Influence of weighting parameter on the coating weight response

8-4-2 Influence of Control Horizon

The control horizon (N_u) defines the number of future control inputs that can be manipulated based on the minimization of the cost function. In general, increasing the control horizon introduces more degrees of freedom at the cost of computational complexity. In this subsection, the influence of the control horizon on the coating weight response is examined. For these simulations, the prediction horizon is fixed to 30 seconds along with the weighting parameter $\lambda = 5 \times 10^{-6}$. Figure 8-6 and Figure 8-7 illustrate the coating weight response and the control input (during transient operation) for different values of the control horizon. As already mentioned, the maximum logical value for the control horizon is $N_u = N_2 - 3$ i.e., 27 seconds.

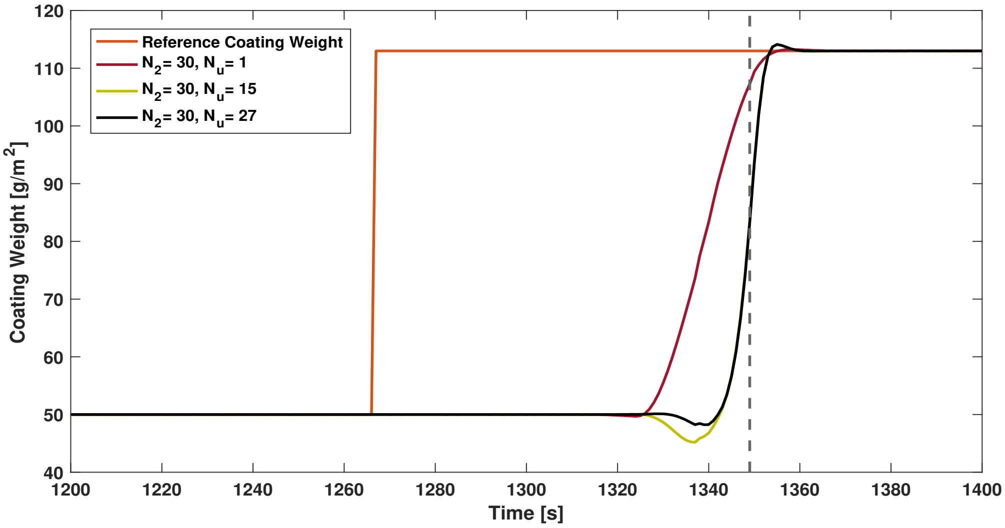

Figure 8-6: Influence of control horizon on the coating weight response

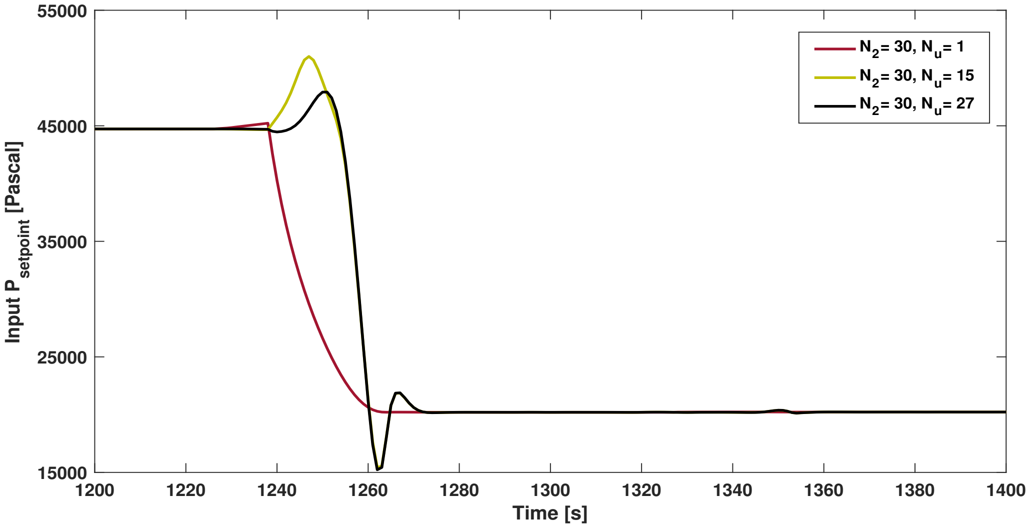

Figure 8-7: Influence of control horizon on control input $P_{setpoint}$

It can be seen that, with a larger control horizon, better tracking performance is achieved with no additional computational challenge being imposed on the computer. Furthermore, the response with control horizon $N_u = 1$ is not desirable for a step-down reference change due to the fact that it will result in an under-coated steel strip. Therefore, the control horizon of three seconds less than the prediction horizon is considered the best choice.

8-4-3 Influence of Prediction Horizon

The prediction horizon (N_2) defines the number of prediction points for which the cost function will be minimized so as to determine the optimal control input. In this sub-section, the influence of the prediction horizon on the coating weight response is studied. For these simulations, the control horizon is chosen to be three seconds less than the prediction horizon along with the weighting parameter $\lambda = 5 \times 10^{-6}$. Figure 8-8 and Figure 8-9 illustrate the coating weight response and the control input (during transient operation) for different values of the prediction horizon.

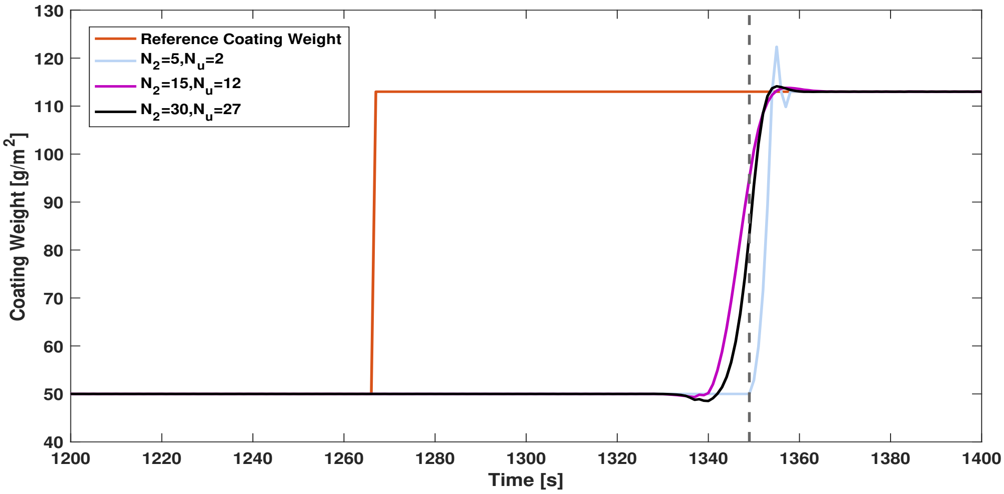

Figure 8-8: Influence of prediction horizon on the coating weight response

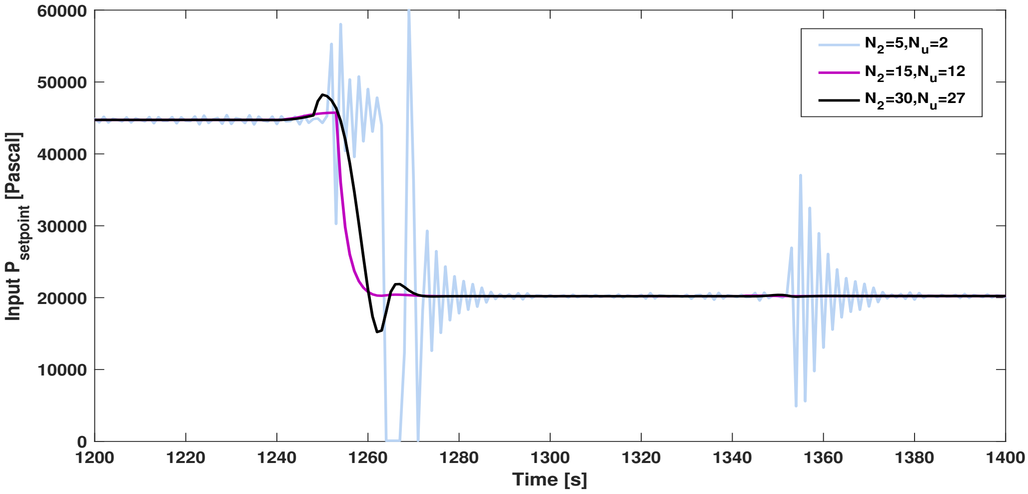

Figure 8-9: Influence of prediction horizon on control input $P_{setpoint}$

It can be seen that, for a small prediction horizon such as $N_2 = 5$, there is an overshoot in the response. When N_2 is small, the future input depends on fewer prediction points, i.e., less information is available to the controller. Hence, this might result in destabilizing the controller. On the contrary, it appears that the higher the prediction horizon, the more steep is the response and better is the reference tracking. However, after a certain value of the prediction horizon, computation load increases on the computer, with no considerable difference being observed in the coating weight response. Finally, to be able to predict the transient behavior, and at the same time, not increase the computational load on the computer, a prediction horizon of 30 seconds is chosen.

8-4-4 Final Simulations

Once all the tuning parameters such as the weighting parameter $\lambda = 5 \times 10^{-6}$, prediction horizon $N_2 = 30$, and control horizon $N_u = 27$ are fixed, the closed-loop simulation is performed to analyze the coating weight response. With the purpose of evaluating the controller's performance, particularly the settling time, the simulation is carried out with no noise in the process model.

Figure 8-10 illustrates the coating weight response. The settling time for the response is calculated to be 4 seconds (excluding time delay). Moreover, it can be seen that the response to the measured disturbance (step change in strip speed at $t = 1073$ second) is fast. It is because NEPSAC optimizes for the future control input based on the prediction of the model output over a certain horizon. Other than the measured disturbance, a step of 5 g/m^2 was given as a load disturbance at t=450 seconds in order to examine the disturbance rejection properties. As expected, it can be seen that the system recovers from the disturbance only after the time delay has passed. In the next step, the noise is included in the process model, and the simulation is performed one more time. The response of the system with noise is illustrated in Figure 8-11.

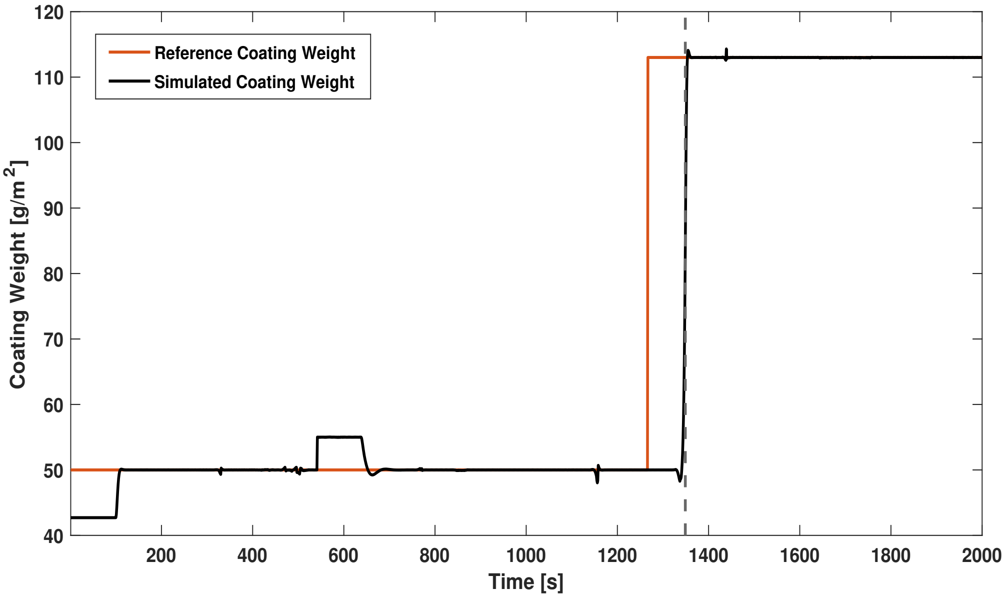

Figure 8-10: Simulated coating weight response without noise

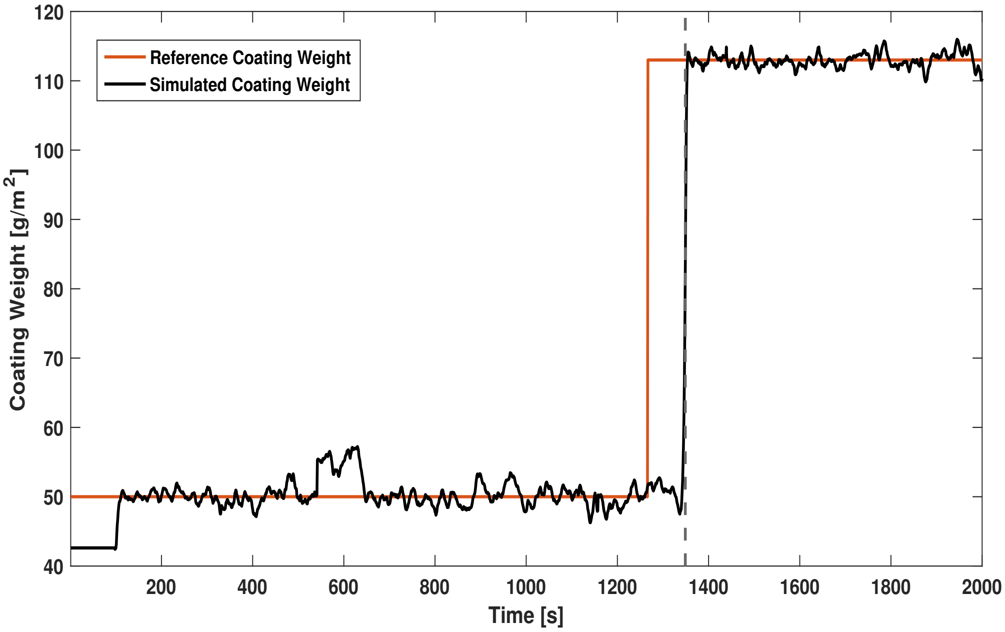

Figure 8-11: Simulated coating weight response with noise

Clearly, it can be seen that the system can track the reference coating weight and it is also able to recover from both the measured and load disturbances. The control input $P_{setpoint}$ achieved from NEPSAC controller is plotted in Figure 8-12.

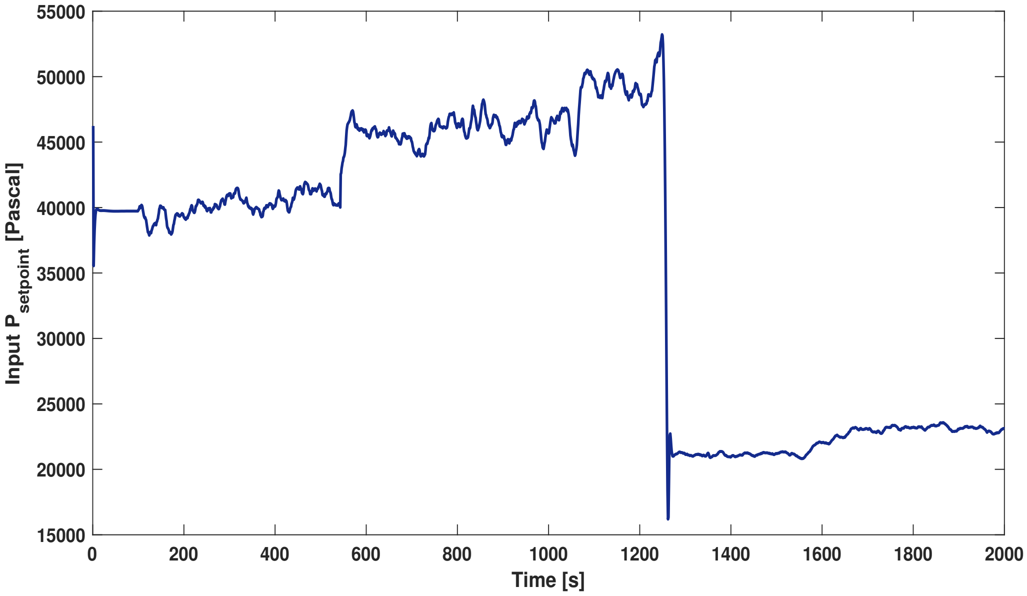

Figure 8-12: Control input $P_{setpoint}$

It can be observed that with the noise present in the coating weight process, there were times when the strip was under-coated, and therefore, it makes sense to add an offset in the target coating weight requirement. The standard deviation of the estimated noise is calculated to be 1.25 g/m^2. Therefore, to obtain an approximately 98% confidence in avoiding the under-coating, an offset equivalent to two times the standard deviation of the noise, i.e., 2.5 g/m^2, is added to the target coating weight. Figure 8-13 illustrates the system's response with the offset added to the reference coating weight.

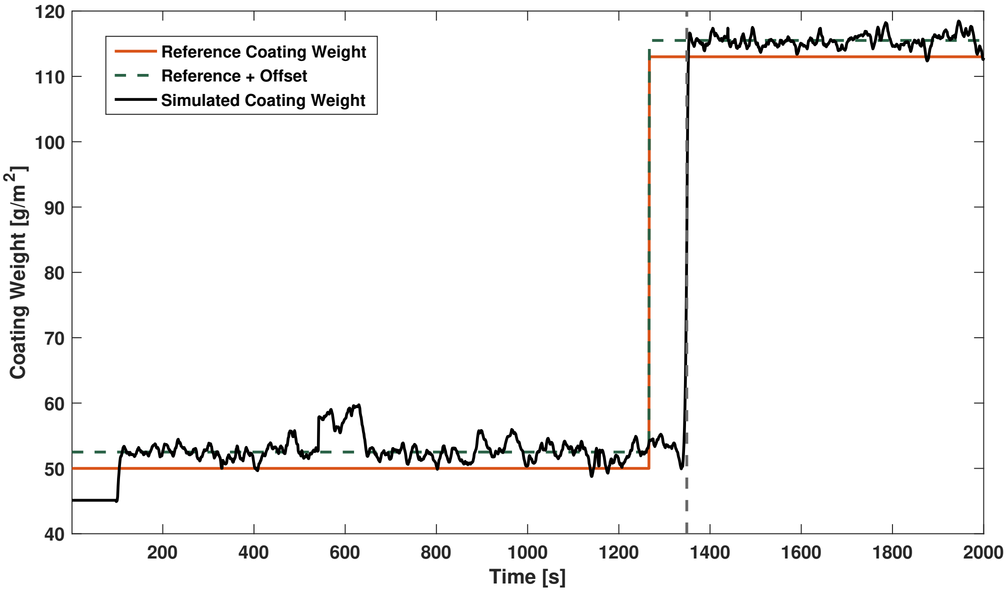

Figure 8-13: Simulated coating weight response

8-5 Comparison of Controllers

In this section, the performance of both the controllers: PI and NEPSAC in the Smith predictor structure is compared. The primary objective of the control is to enhance the performance, i.e., to make the coating weight output behave in a desirable manner. The purpose of this section is to assess the closed-loop performance by analyzing the characteristics such as settling time, rise time, and overshoot. The settling time and rise time are used to describe the response speed, and the overshoot is associated with the response quality [44].

The coating weight response of both the controllers to track the reference is shown in Figure 8-14. To analyze the results better, part of the simulation under transient operating conditions with no noise in the process is plotted. One can see that both the controllers can follow the reference trajectory. However, the accuracy in tracking the target coating weight is undoubtedly better with the NEPSAC controller.

As already mentioned before, the production data used for simulation has a step increase of 0.13 m/s in the strip speed at t = 1073 second (Figure 7-14), which is seen as a measured disturbance. Figure 8-14 clearly illustrates that NEPSAC has a much faster disturbance rejection response compared to the PI controller. Furthermore, the control input $P_{setpoint}$ achieved from both the controllers are plotted in Figure 8-15.

The main characteristics, such as the settling time, rise time, and overshoot, are calculated for both the systems with PI and NEPSAC controller in the Smith predictor structure and are specified in Table 8-1. The settling time and rise time indicated in the table are excluding the time delay.

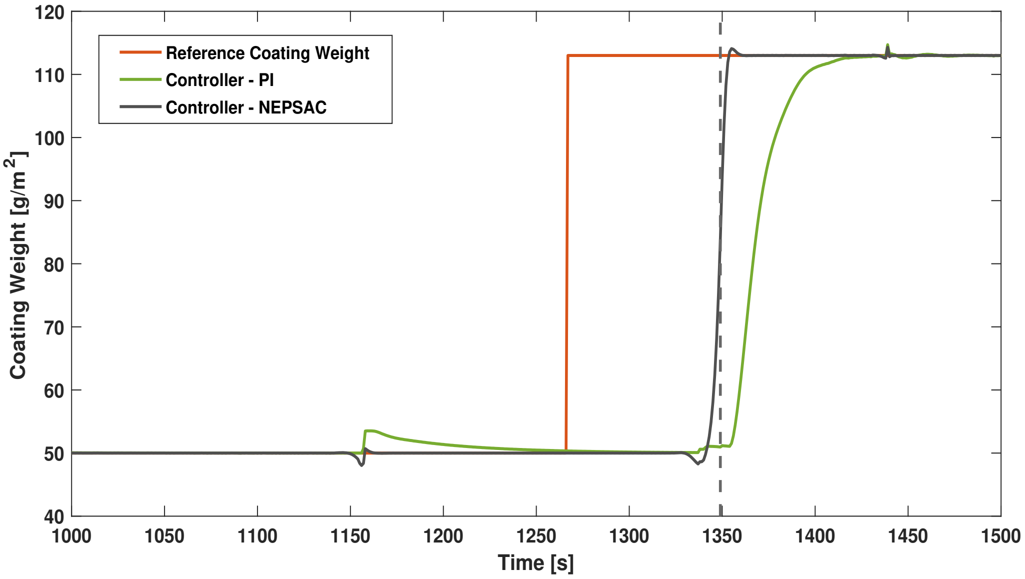

Figure 8-14: Comparison of coating weight response for PI and NEPSAC controllers

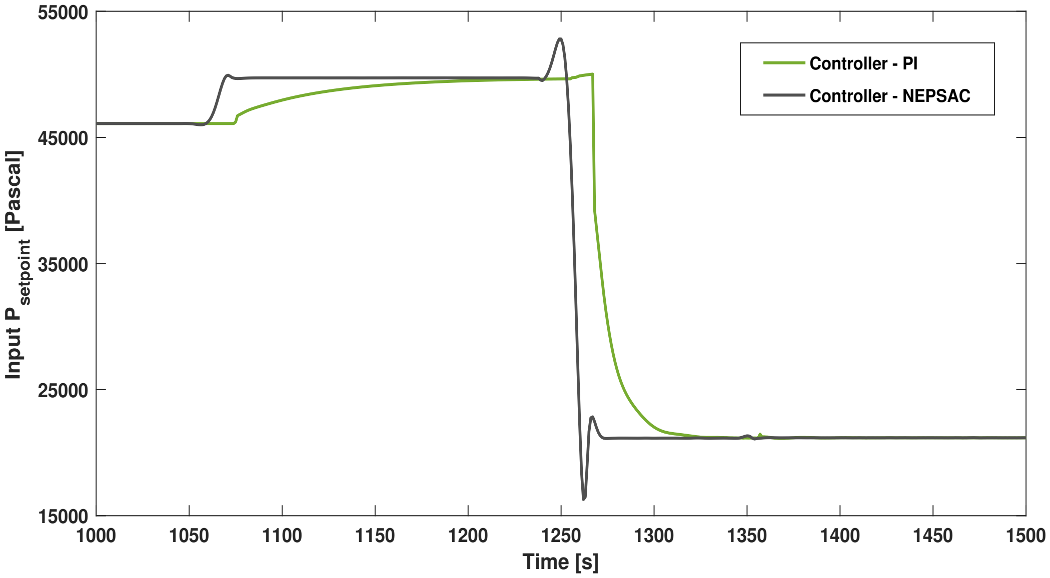

Figure 8-15: Comparison of control input achieved from PI and NEPSAC controllers

Characteristics	PI	NEPSAC
Settling Time [sec]	64	4
Rise Time [sec]	38	3
Overshoot [%]	0	1

Table 8-1: Comparison of time-domain specifications for PI and NEPSAC controllers

In summary, simulations demonstrate that the Smith predictor with the PI controller is not the most accurate way to control the coating weight. It is because the controller is tuned according to a linearized process model. Moreover, because of the high non-linearity, the PI controller is tuned for five different operating points. The Non-linear Extended Prediction Self-Adaptive Control (NEPSAC), on the other hand, performs much better as long as the process model is identified accurately. On top of that, NEPSAC provides many tuning parameters that can be adjusted based on the process needs. With NEPSAC in the Smith predictor structure, it was possible to achieve a small rise time with a small overshoot.

Chapter 9

Conclusions & Outlook

In the final chapter of this thesis, the reader is presented with a summary of the work, conclusion, and recommendations for future research.

9-1 Summary

The primary objective of the thesis was to control the coating weight of the zinc layer with the widely used air-knife wiping system during the hot-dip galvanizing process. The control of coating weight is essential because the overall quality of the product depends on the amount of zinc deposited at the surface of the steel. Over-deposition of zinc results in excessive use of zinc, which is expensive, and an under-coated strip results in rejection. Given that, the main challenge in the closed-loop control was the need to compensate for the measurement delay resulting from the time-varying strip speed over the distance between the air knives and the cold coating gauge.

In Chapter 2, the reader was acquainted with a series of consecutive processes broadly known as hot rolling, cold rolling, annealing, and hot-dip galvanizing that are used to realize the production of flat steel strip. In Chapter 3, background knowledge on the coating weight control equipment, and the coating gauge were provided. Furthermore, the first-principle coating weight model that depends on the process variables such as the strip speed, air-knife wiping pressure, and the strip-to-knife distance was explained. In the end, the pressure and shear stress correlations developed by various authors were also discussed.

Chapter 4 comprised of system identification for the linear dynamics of fan and the non-linear static coating weight model. A second-order transfer function was estimated for the fan's dynamics with a 96.3% fit between the model output and measurement data. With the aim to calculate the coating weight using the first-principle model, the pressure and shear-stress correlations were parameterized based on the existing models in the literature. Few experiments were performed to realize pressure distribution profiles for different air-knife wiping pressures and strip-to-knife distances. Consequently, these pressure profiles were used to estimate the parameters in the pressure correlations. However, the shear-stress correlation parameters were estimated using non-linear grey-box system identification due to the lack of experimental setup for shear stress measurements. It turned out that despite a good match (83.81%) between the measurement data and the non-linear first-principle model, the mean of the modeling error was 0.5 g/m^2. As a result, a third-order polynomial was fitted to the modeling error concerning the three process variables. It was observed that combining the polynomial fit with the first-principle model, the mean of the error dropped to zero. Finally, the chapter was concluded by identifying a noise model in the coating weight process that explains the mismatch between the measurement data and the model output.

In Chapter 5, properties of time delay in continuous-time and discrete-time were discussed. It was pointed out that time-delay in discrete time can be expressed as a rational transfer function, and thereby it becomes a shift in the state variable vector. The reader was also presented with a formulation to calculate the discrete-time time-varying measurement delay. In the end, the accuracy of the estimated time-delay was represented. Chapter 6 dealt with model discretization and the choice of sampling time in order to implement the controller on a digital platform.

Chapter 7 was dedicated to the popular dead-time compensation methods known as the Smith Predictor with PI controller. It was shown that the controller was tuned based on the process model linearized around five operating points. Later, a simulation from the production data was performed to analyze the closed-loop performance of the controller. The coating weight response was seen to follow the reference trajectory with no overshoot and a settling time of around 60 seconds (excluding time delay). However, the response of the system to the measured disturbance and the load disturbance was slow.

In Chapter 8, an advanced control strategy namely Non-linear Extended Prediction Self-Adaptive Control (NEPSAC) was discussed. Similar to MPC algorithm, it computes optimum control inputs by optimizing a cost function over a prediction horizon. However, because of the time-delay, the cost incurred from the initial prediction steps equivalent to the delay duration, must not be considered. As the delay varies with time, it introduces a time-varying parameter (N_1) in the cost function, which increases the complexity of the problem. Therefore, the control strategy was modified by implementing NEPSAC in the Smith predictor structure to deal with the difficulty of time-varying delay. Several simulations with the production data were performed to analyze the closed-loop performance of the controller and to study the influence of various tuning parameters such as the control horizon (N_u), prediction horizon (N_2), and the weighting parameter (λ). It was seen that the coating weight response follows the reference trajectory with a 1% overshoot and a settling time of 4 seconds. Moreover, the response of the coating weight to the measured disturbances (strip speed and strip-to-knife distance) was very fast, since the NEPSAC optimizes for the optimum control input based on the future prediction of the model output.

9-2 Conclusions

The work in this thesis addresses two main objectives: improving the coating weight model and controlling the zinc layer coating weight. From the modeling point of view, it was clearly shown that a better fit is obtained between the measurement data and the first-principle coating weight model with the estimated parameters compared to that of the existing power-law model. The root mean square error for the validation data set of the power-law model, and the estimated model was calculated to be 6.39 g/m^2 and 3.52 g/m^2 respectively. Therefore, this result illustrates the improvement in the coating weight model.

The next goal was to control the coating weight of the zinc layer. The reader was presented with two control schemes: PI controller and NEPSAC in the Smith predictor structure. It was showcased in the thesis that the main challenges mentioned in Section 1-2 were addressed more efficiently by the NEPSAC than the PI controller. First and foremost, the coating weight transients that occur because of the changing strip speed were effectively controlled by NEPSAC. As already stated, this is due to the fact that NEPSAC optimizes for control input based on the predictions of the model output. In the second place, the accuracy in tracking the reference coating weight was undoubtedly better for NEPSAC with a settling time of only 4 seconds compared to 64 seconds of the PI controller. On a final note, the time-varying delay was taken care of by the Smith predictor structure. As long as the prediction model is identified accurately, NEPSAC performs really well. However, any load disturbances and the noise in the coating weight process will only be corrected after the time delay has passed.

9-3 Recommendations for Future Work

While some good results have been obtained, there are still several possibilities available for further improvements and research. Few of them are mentioned below:

- A substantial amount of settling time was observed in the Smith predictor's closed-loop simulation with the PI controller. Hence, it would be advisable to perform a simulation with the existing control of Tata Steel comprising a feed-forward controller in the Smith predictor structure. The feed-forward control would speed up the response, and it would be interesting to compare its results with the control achieved from NEPSAC method.
- Since the experimental equipment used to measure the wall shear stress was not available, the shear-stress model parameters were estimated using non-linear grey-box system identification. The estimate of the parameters could potentially also be computed by performing Computational Fluid Dynamics (CFD) simulation of the air-knife wiping jet.
- Probably an additional step could be towards improving the coating weight model. For this thesis work, it was assumed that there are no dynamics present between the air-knife wiping system and the cold coating gauge. Therefore, the transfer of the strip from the wiping system through the cooling tower, and finally to the coating gauge could be investigated to see if there is some influence of the temperature difference on the coating weight.

Appendix A

Time-Varying Measurement Delay

Algorithm 1: Calculation of Time-Varying Measurement Delay

```
L = 153.5 ← Distance between air-knives and coating gauge (meters);
M = 154 ← Maximum Delay (seconds);
$V_s$ ← Strip Speed (m/s);
$Z$ ← Strip-to-knife Distance (mm);
$P_0$ ← Air-knife wiping pressure (Pascal);
$cw_{ref}$ ← Reference Coating Weight ($g/m^2$);
$cw$ ← Measured Coating Weight ($g/m^2$);
for i = 1:end-M do
    $L_{sum} = 0$ ;
    for k = 0:M do
        $L_{sum} = L_{sum} + V_s(i+k)$ ;
        if $L_{sum} < L$ then
            $k = k + 1$;
        else
            break;
        end
    end
    $cw(i) = cw(i+k)$;
end
$Z = Z$(1:end-M);
$V_s = V_s$(1:end-M);
$P_0 = P_0$(1:end-M);
$cw_{ref} = cw_{ref}$(1:end-M);
```

Appendix B

Zero-Order Hold Discretization

The general linear state space representation is given by the following form:

$$\begin{aligned} \dot{x}(t) &= Ax(t) + Bu(t) \\ y(t) &= Cx(t) + Du(t) \end{aligned} \tag{B-1}$$

At first, the continuous linear time-invariant system is solved for $x(t)$. On rearranging the terms in Equation B-1, it can be written as:

$$\dot{x} - Ax(t) = Bu(t)$$

The above equation is now left multiplied with e^{-At} to get:

$$\mathrm{e}^{-At}\dot{x}(t) - \mathrm{e}^{-At}Ax(t) = \mathrm{e}^{-At}Bu(t)$$

The left side of the equation is the result of chain rule, so it can be rewritten as:

$$\frac{\partial}{\partial t}\left(\mathrm{e}^{-At}x(t)\right) = \mathrm{e}^{-At}Bu(t)$$

Both sides of the equation are integrated to get:

$$\begin{aligned} \mathrm{e}^{-At}x(t) - \mathrm{e}^{0}x(0) &= \textstyle\int_0^t \mathrm{e}^{-A\tau}Bu(\tau)d\tau \\ \mathrm{e}^{-At}x(t) &= \textstyle\int_0^t \mathrm{e}^{-A\tau}Bu(\tau)d\tau + x(0) \end{aligned}$$

In order to find $x(t)$, the equation is left multiplied with e^{At}

$$\begin{aligned} \mathrm{e}^{At}\mathrm{e}^{-At}x(t) &= \mathrm{e}^{At}\textstyle\int_0^t \mathrm{e}^{-A\tau}Bu(\tau)d\tau + \mathrm{e}^{At}x(0) \\ \boldsymbol{x(t)} &\boldsymbol{= \mathrm{e}^{At}x(0) + \mathrm{e}^{At}\textstyle\int_0^t \mathrm{e}^{-A\tau}Bu(\tau)d\tau} \end{aligned} \tag{B-2}$$

Now, the system is discretized by sampling it at even intervals of time step T_s. It is important to note that with the zero-hold method, the input $u(t)$ will remain constant between the samples. To simplify the notation, the following is defined:

$$x[k] = x(kT_s)$$

With the new notation, Equation B-2 can be written as:

$$x[k] = \mathrm{e}^{AkT_s}x(0) + \mathrm{e}^{AkT_s}\int_0^{kT_s} \mathrm{e}^{-A\tau}Bu(\tau)d\tau \tag{B-3}$$

The ultimate aim is to get these equations in the form of discrete state space equation:

$$x[k+1] = A_d x[k] + B_d u[k]$$

Using the Equation B-3, $x[k+1]$ is given by:

$$x[k+1] = \mathrm{e}^{A(k+1)T_s}x(0) + \mathrm{e}^{A(k+1)T_s}\int_0^{(k+1)T_s} \mathrm{e}^{-A\tau}Bu(\tau)d\tau$$

So as to relate $x[k+1]$ to $x[k]$, Equation B-3 is left multiplied with e^{AT_s}:

$$\mathrm{e}^{AT_s}x[k] = \mathrm{e}^{A(k+1)T_s}x(0) + \mathrm{e}^{A(k+1)T_s}\int_0^{kT_s} \mathrm{e}^{-A\tau}Bu(\tau)d\tau$$

This equation is rearranged to solve for the same term present in $x[k+1]$:

$$\mathrm{e}^{A(k+1)T_s}x(0) = \mathrm{e}^{AT_s}x[k] - \mathrm{e}^{A(k+1)T_s}\int_0^{kT_s} \mathrm{e}^{-A\tau}Bu(\tau)d\tau$$

Plugging this term in $x[k+1]$:

$$\begin{aligned} x[k+1] =& \mathrm{e}^{AT_s}x[k] + \mathrm{e}^{A(k+1)T_s}\left(-\int_0^{kT_s} \mathrm{e}^{-A\tau}Bu(\tau)d\tau + \int_0^{(k+1)T_s} \mathrm{e}^{-A\tau}Bu(\tau)d\tau\right) \\ x[k+1] =& \mathrm{e}^{AT_s}x[k] + \mathrm{e}^{A(k+1)T_s}\int_{kT_s}^{(k+1)T_s} \mathrm{e}^{-A\tau}Bu(\tau)d\tau \end{aligned}$$

Everything at this stage is in the right form, but the second term on the right-hand side can still be simplified quite a bit. Note that, because of the zero-order hold method the the input $u(t) \in [k, kT_s)$ is constant. So, the term $Bu(t)$ is taken outside the integral.

$$x[k+1] = \mathrm{e}^{AT_s}x[k] + \mathrm{e}^{A(k+1)T_s}\int_{kT_s}^{(k+1)T_s} \mathrm{e}^{-A\tau}d\tau Bu[k]$$

Next, the term $\mathrm{e}^{A(k+1)T_s}$ is taken inside the integral:

$$x[k+1] = \mathrm{e}^{AT_s}x[k] + \int_{kT_s}^{(k+1)T_s} \mathrm{e}^{A((k+1)T_s-\tau)}d\tau Bu[k]$$

Now, the integral is solved using variable solution. Let's take $v = (k+1)T_s - \tau$, which gives $\frac{dv}{d\tau} = -1 \rightarrow d\tau = -dv$. Considering the new upper and lower bounds of the integral, when $\tau = kT_s$ then $v = T_s$ and when $\tau = (k+1)T_s$ then $v = 0$. The equation is rewritten as:

$$x[k+1] = \mathrm{e}^{AT_s}x[k] - \int_{T_s}^{0} \mathrm{e}^{Av}dvBu[k]$$

On reversing the limits of integration, the sign of the integral is changed:

$$x[k+1] = \mathrm{e}^{AT_s} x[k] + \int_0^{T_s} \mathrm{e}^{Av} dv Bu[k]$$

Finally, the integral is evaluated by recalling that $\frac{d}{dt}\mathrm{e}^{At} = A\mathrm{e}^{At}$ and assuming that A is invertible:

$$\begin{aligned} x[k+1] &= \mathrm{e}^{AT_s} x[k] + A^{-1}\left(\mathrm{e}^{AT_s} - \mathrm{e}^0\right) Bu[k] \\ x[k+1] &= \mathrm{e}^{AT_s} x[k] + A^{-1}\left(\mathrm{e}^{AT_s} - I\right) Bu[k] \end{aligned}$$

Ultimately, the discretized state matrix and the input matrix are derived as follows:

$$\begin{aligned} \boldsymbol{A_d} &= \mathbf{e}^{\boldsymbol{AT_s}} \\ \boldsymbol{B_d} &= \boldsymbol{A^{-1}}\left(\mathbf{e}^{\boldsymbol{AT_s}} - \boldsymbol{I}\right) \boldsymbol{B} \end{aligned} \tag{B-4}$$

Fortunately, the discretized output matrix and feed-through matrix remain the same:

$$\begin{aligned} \boldsymbol{C_d} &= \boldsymbol{C} \\ \boldsymbol{D_d} &= \boldsymbol{D} \end{aligned} \tag{B-5}$$

Appendix C

Tuning of PI Controller

C-1 Tuning PI Controller for Second Operating Point

The tuning of the controller resulted in a gain K_c of -172 and an integration time T_i of 8 seconds.

$$K_c\left(1+\frac{1}{T_i s}\right) = -172\left(1+\frac{1}{8s}\right) \tag{C-1}$$

To reduce the Smith Predictor's sensitivity to modeling errors, it is important to have large stability margins in the open-loop transfer function as shown in Figure C-1.

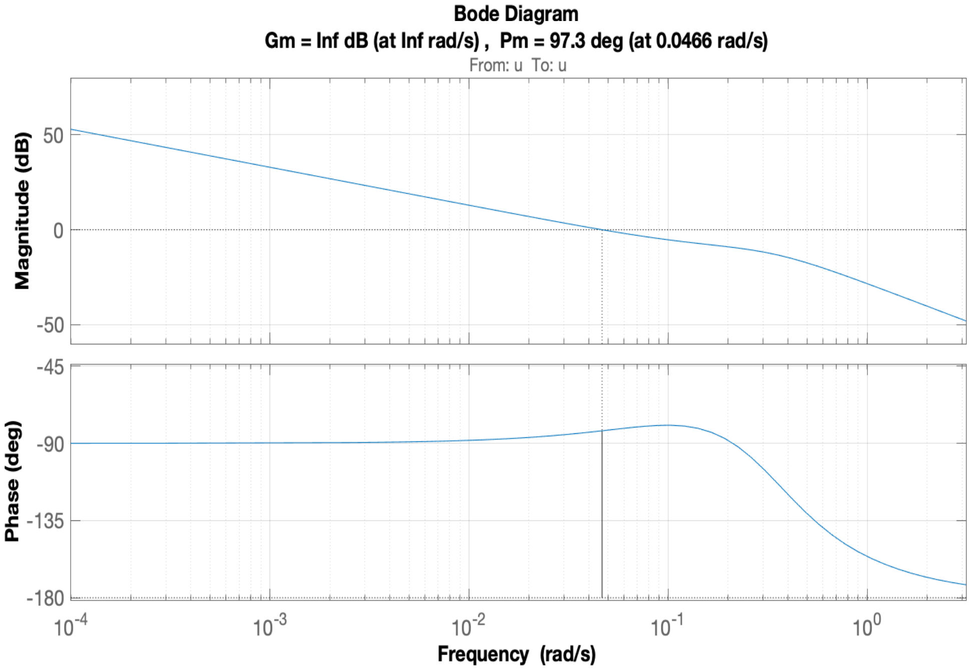

Figure C-1: Open-loop Bode Plot [Second Operating Point]

The open-loop has enough gain and phase margin. So, now the focus is on the open-loop transfer function from y_{sp} to dp with the inner loop closed. To get better insight into stability margins for this loop, a perturbed model with 10% error in nonlinear static gain and 5% error in time delay is chosen as the real process model. Stability margins obtained for the loop transfer function from y_{sp} to dp are shown in Figure C-2. It is important to note that the cut-off frequency of low-pass filter used is $f_c = 0.02$Hz.

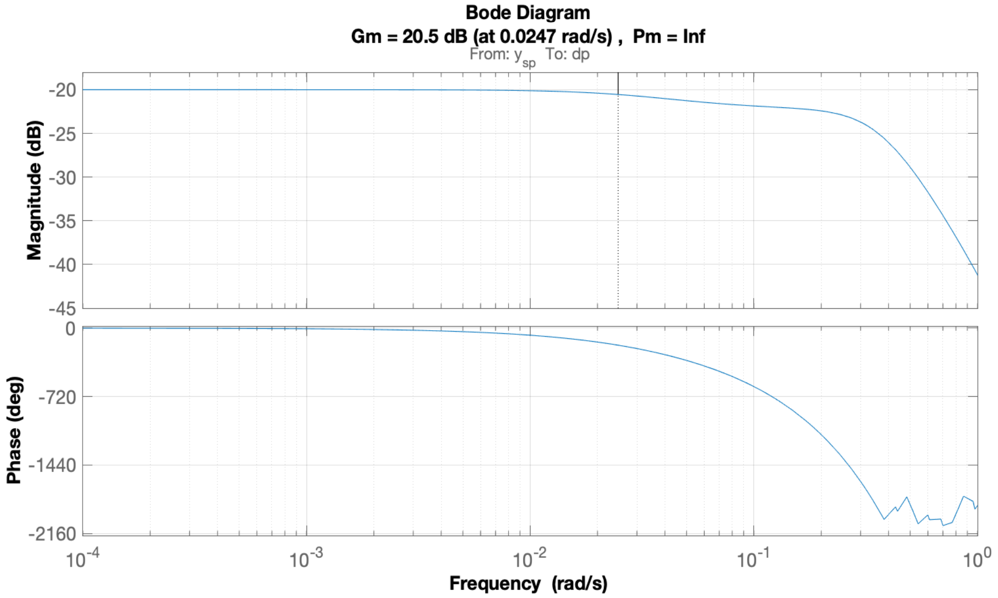

Figure C-2: Outer Open-loop Bode Plot [Second Operating Point]

The open-loop transfer function from y_{sp} to dp also has sufficient gain and phase margin. To assess the performance of the tuned PI controller, the feedback loop is closed and the step input is applied at the reference signal (y_{sp}) and output disturbance signal (d). The step response for the nominal and perturbed model are plotted in Figure C-3.

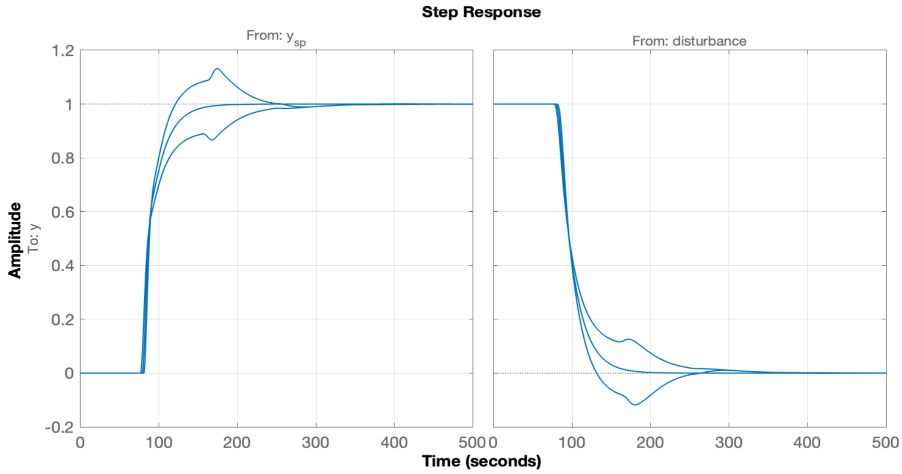

Figure C-3: Step response [Second Operating Point]

With the closed-loop step response plotted above, it can be seen that the response of the controller is slow with a settling time of 98 seconds (excluding time delay). A 15% overshoot and 15% undershoot were calculated in the step response of the two perturbed models. Therefore, both the closed-loop requirements are satisfied.

C-2 Tuning PI Controller for Third Operating Point

The tuning of the controller resulted in a gain K_c of -135 and an integration time T_i of 8.43 seconds.

$$K_c\left(1+\frac{1}{T_i s}\right) = -135\left(1+\frac{1}{8.43s}\right) \tag{C-2}$$

To reduce the Smith Predictor's sensitivity to modeling errors, it is important to have large stability margins in the open-loop transfer function as shown in Figure C-4.

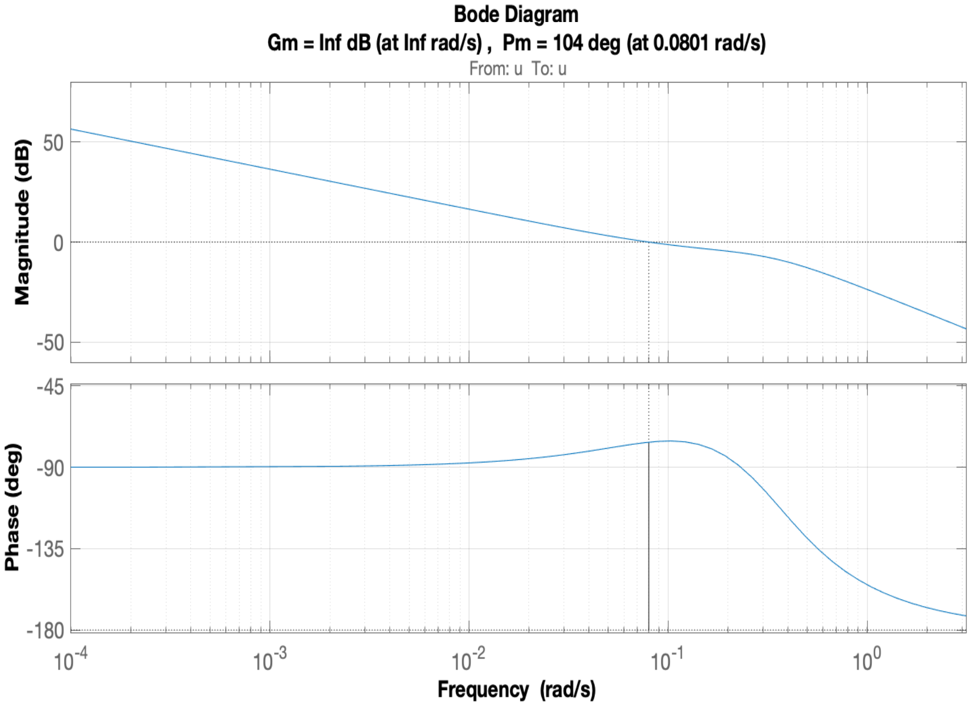

Figure C-4: Open-loop Bode Plot [Third Operating Point]

The open-loop has enough gain and phase margin. So, now the focus is on the open-loop transfer function from y_{sp} to dp with the inner loop closed. To get better insight into stability margins for this loop, a perturbed model with 10% error in nonlinear static gain and 5% error in time delay is chosen as the real process model. Stability margins obtained for the loop transfer function from y_{sp} to dp are shown in Figure C-5. It is important to note that the cut-off frequency of low-pass filter used is $f_c = 0.02$Hz.

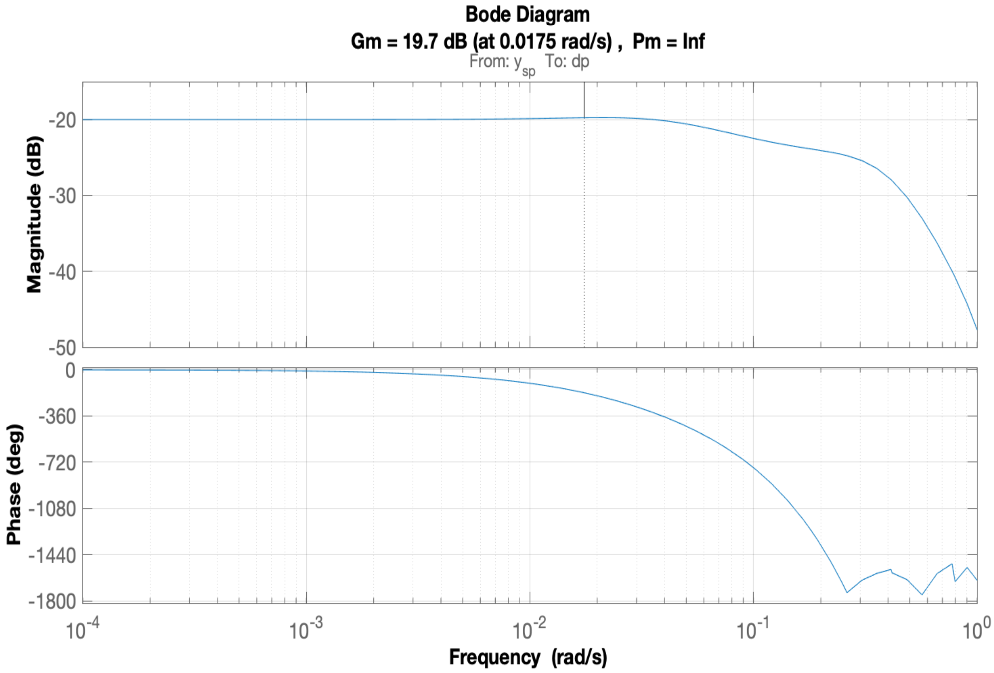

Figure C-5: Outer Open-loop Bode Plot [Third Operating Point]

The open-loop transfer function from y_{sp} to dp also has sufficient gain and phase margin. To assess the performance of the tuned PI controller, the feedback loop is closed and the step input is applied at the reference signal (y_{sp}) and output disturbance signal (d). The step response for the nominal and perturbed model are plotted in Figure C-6.

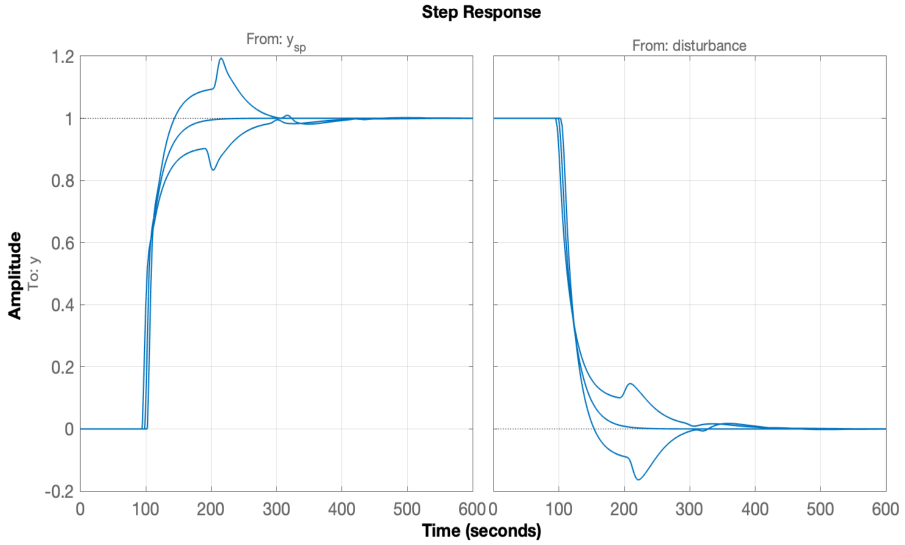

Figure C-6: Step response [Third Operating Point]

With the closed-loop step response plotted above, it can be seen that the response of the controller is slow with a settling time of 94 seconds (excluding time delay). A 20% overshoot and

17% undershoot were calculated in the step response of the two perturbed models. Therefore, both the closed-loop requirements are satisfied.

C-3 Tuning PI Controller for Fourth Operating Point

The tuning of the controller resulted in a gain K_c of -150 and an integration time T_i of 9.87 seconds.

$$K_c\left(1+\frac{1}{T_i s}\right)=-150\left(1+\frac{1}{9.87s}\right) \tag{C-3}$$

To reduce the Smith Predictor's sensitivity to modeling errors, it is important to have large stability margins in the open-loop transfer function as shown in Figure C-7.

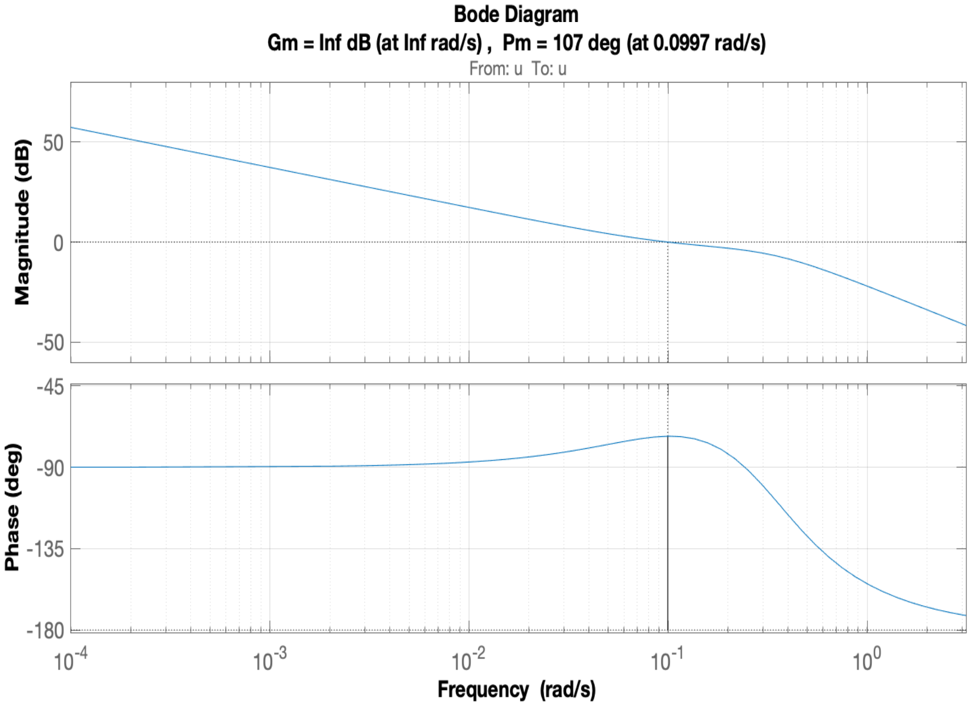

Figure C-7: Open-loop Bode Plot [Fourth Operating Point]

The open-loop has enough gain and phase margin. So, now the focus is on the open-loop transfer function from y_{sp} to dp with the inner loop closed. To get better insight into stability margins for this loop, a perturbed model with 10% error in nonlinear static gain and 5% error in time delay is chosen as the real process model. Stability margins obtained for the loop transfer function from y_{sp} to dp are shown in Figure C-8. It is important to note that the cut-off frequency of low-pass filter used is $f_c = 0.02$Hz.

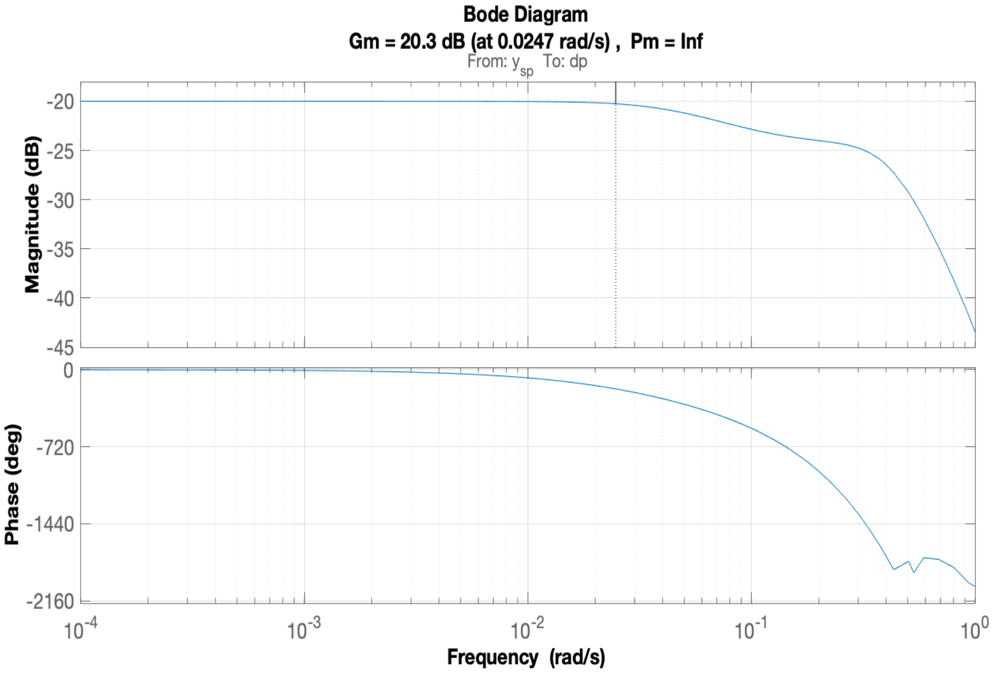

Figure C-8: Outer Open-loop Bode Plot [Fourth Operating Point]

The open-loop transfer function from y_{sp} to dp also has sufficient gain and phase margin. To assess the performance of the tuned PI controller, the feedback loop is closed and the step input is applied at the reference signal (y_{sp}) and output disturbance signal (d). The step response for the nominal and perturbed model are plotted in Figure C-9.

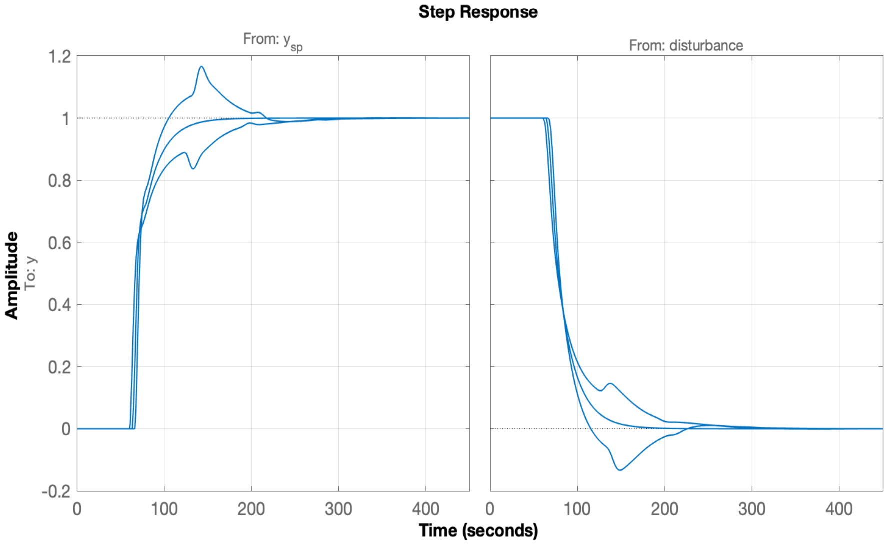

Figure C-9: Step response [Fourth Operating Point]

With the closed-loop step response plotted above, it can be seen that the response of the controller is slow with a settling time of 92 seconds (excluding time delay). A 17% overshoot and

15% undershoot were calculated in the step response of the two perturbed models. Therefore, both the closed-loop requirements are satisfied.

C-4 Tuning PI Controller for Fifth Operating Point

The tuning of the controller resulted in a gain K_c of -75 and an integration time T_i of 9.37 seconds.

$$K_c\left(1+\frac{1}{T_i s}\right) = -75\left(1+\frac{1}{9.37s}\right) \tag{C-4}$$

To reduce the Smith Predictor's sensitivity to modeling errors, it is important to have large stability margins in the open-loop transfer function as shown in Figure C-10.

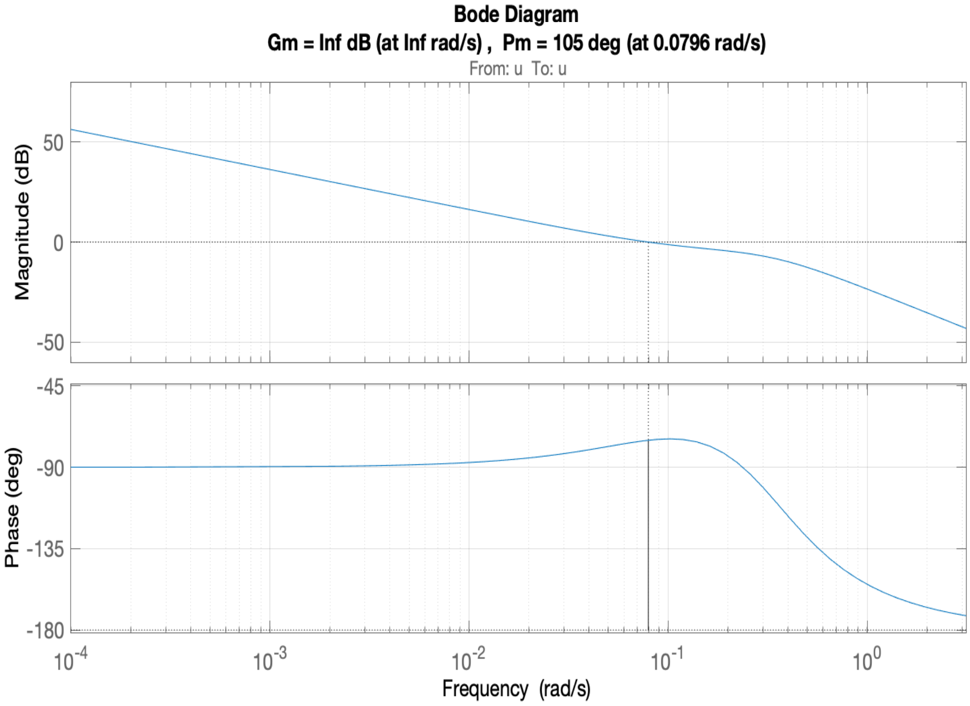

Figure C-10: Open-loop Bode Plot [Fifth Operating Point]

The open-loop has enough gain and phase margin. So, now the focus is on the open-loop transfer function from y_{sp} to dp with the inner loop closed. To get better insight into stability margins for this loop, a perturbed model with 10% error in nonlinear static gain and 5% error in time delay is chosen as the real process model. Stability margins obtained for the loop transfer function from y_{sp} to dp are shown in Figure C-11. It is important to note that the cut-off frequency of low-pass filter used is $f_c = 0.02$Hz.

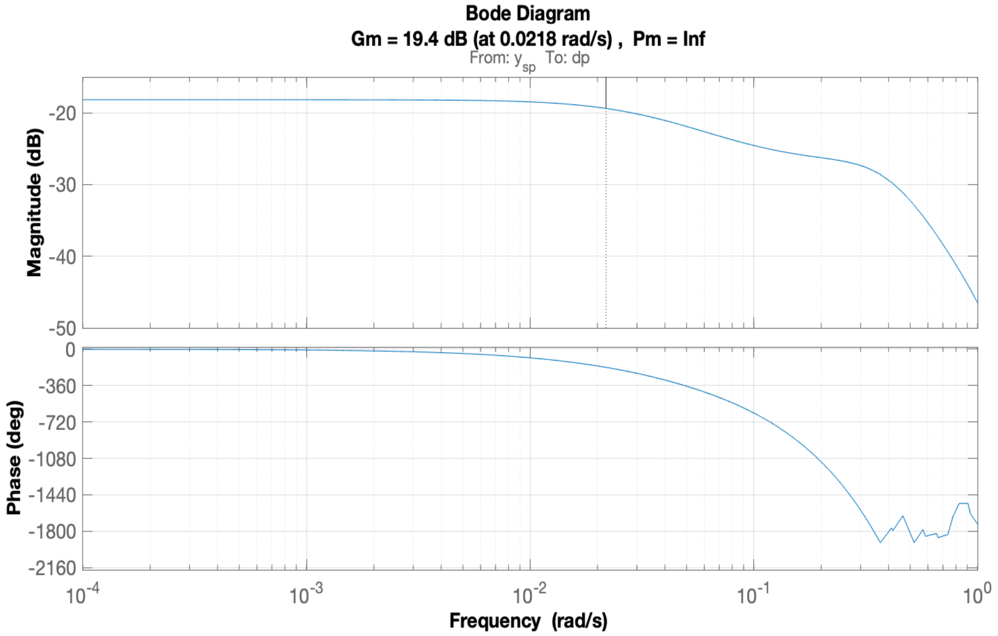

Figure C-11: Outer Open-loop Bode Plot [Fifth Operating Point]

The open-loop transfer function from y_{sp} to dp also has sufficient gain and phase margin. To assess the performance of the tuned PI controller, the feedback loop is closed and the step input is applied at the reference signal (y_{sp}) and output disturbance signal (d). The step response for the nominal and perturbed model are plotted in Figure C-12.

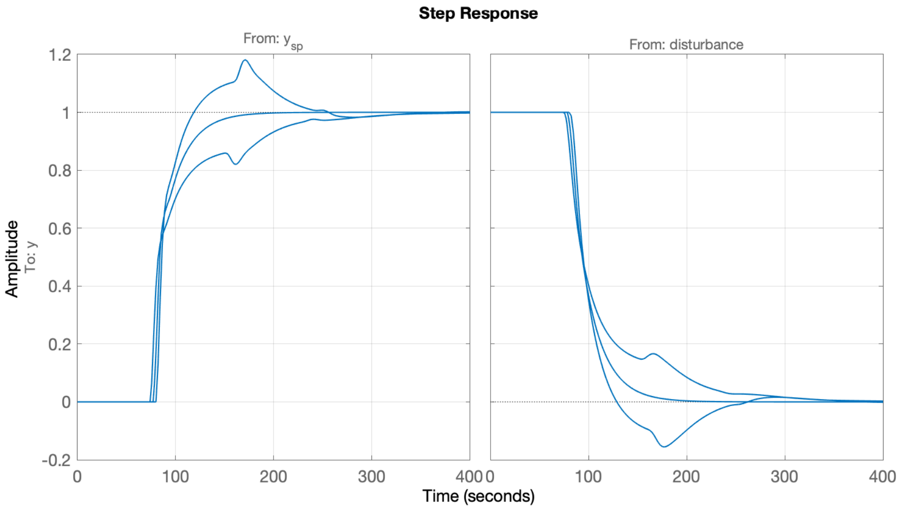

Figure C-12: Step response [Fifth Operating Point]

With the closed-loop step response plotted above, it can be seen that the response of the controller is slow with a settling time of 89 seconds (excluding time delay). A 18% overshoot and 18% undershoot were calculated in the step response of the two perturbed models. Therefore, both the closed-loop requirements are satisfied.

Bibliography

[1] Tata steel in IJmuiden, 2019. https://www.tatasteel.nl/nl/over/organisatie/inijmuiden.

[2] F. Ajersch and F. Ilinca. Review of modeling and simulation of galvanizing operations. *Steel Research International*, 89(1), 2018.

[3] P. Akhil, M. Gupta, and D. Zanwar. Process parameter optimization for zinc coating weight control in continuous galvanizing line. *International Journal of Scientific Engineering Research*, 3(11):1–6, 2012.

[4] S. Beltaos and N. Rajaratnam. Plane turbulent impinging jets. *Journal of Hydraulic Research*, 11(1):29–59, 1973.

[5] Svante Bjorklund. *A Survey and Comparison of Time-Delay Estimation Methods in Linear Systems*. Licentiate thesis, Linkopings University, 2003.

[6] G. Bloch, F. Sirou, V. Eustache, and P. Fatrez. Neural intelligent control for a steel plant. *IEEE Transactions on Neural Networks*, 8(4):910–918, 1997.

[7] Christopher Burnett. The benefits of 'hot' coating weight measurements to coating control. Technical report, Mount Airy, MD, United States, 2012.

[8] Benjamin Nigel Carruthers-Watt. Strip tracking in hot strip mills, 2011.

[9] S. Cristea, C. De Prada, and R. De Keyser. Predictive control of a process with variable dead-time. In *IFAC Proceedings Volumes (IFAC-PapersOnline)*, volume 16, pages 309–314, 2005.

[10] F. A. Cuzzola and T. Parisini. A multivariable control scheme for a hot dip galvanising line process. In *Proceedings of the IEEE International Conference on Control Applications*, pages 938–943, 2010.

[11] C. Dasarathy. Processing of uncoated steel sheets. *Department of Materials Engineering, University of Wales*, 2005.

[12] R. M. C. De Keyser and A. R. Van Cauwenberghe. Extended prediction self-adaptive control. In *IFAC Proceedings Series*, pages 1255–1260, 1985.

[13] A. Dutta, R. De Keyser, and I. Nopens. Robust nonlinear extended prediction self-adaptive control (nepsac) of continuous bioreactors. In *2012 20th Mediterranean Conference on Control and Automation, MED 2012 - Conference Proceedings*, pages 658–664, 2012.

[14] W. J. Edwards, A. J. Carlton, G. F. Harvey, R. F. K. Evans, and P. J. McKerrow. Coating mass control system design for a continuous galvanizing line. *Automatica*, 12(3):225–235, 1976.

[15] C. H. Ellen and C. V. Tu. An analysis of jet stripping of liquid coatings. *Journal of Fluids Engineering, Transactions of the ASME*, 106(4):399–404, 1984.

[16] E. A. Elsaadawy, G. S. Hanumanth, A. K. S. Balthazaar, J. R. McDermid, A. N. Hrymak, and J. F. Forbes. Coating weight model for the continuous hot-dip galvanizing process. *Metallurgical and Materials Transactions B: Process Metallurgy and Materials Processing Science*, 38(3):413–424, 2007.

[17] M. Galvez-Carrillo, R. De Keyser, and C. Ionescu. Nonlinear predictive control with dead-time compensator: Application to a solar power plant. *Solar Energy*, 83(5):743–752, 2009.

[18] H. L. Gerber. Magnetic damping of steel sheet. *IEEE Transactions on Industry Applications*, 39(5):1448–1453, 2003.

[19] N. Guelton and A. Lerouge. Coating weight control on arcelormittal's galvanizing line at florange works. *Control Engineering Practice*, 18(10):1220–1229, 2010.

[20] R. Hodrea, I. Nascu, R. De Keyser, and C. M. Ionescu. Epsac predictive control applied to muscle relaxant administration. In *IFAC Proceedings Volumes (IFAC-PapersOnline)*, volume 45, pages 331–336, 2012.

[21] C. M. Ionescu, R. Hodrea, and R. De Keyser. Variable time-delay estimation for anesthesia control during intensive care. *IEEE Transactions on Biomedical Engineering*, 58(2):363–369, 2011.

[22] O. L. R. Jacobs. Designing feedback controllers to regulate deposited mass in hot-dip galvanizing. *Control Engineering Practice*, 3(11):1529–1542, 1995.

[23] C.E. Jordan, K.M. Goggins, A.O. Benscoter, and A.R. Marder. Metallographic preparation technique for hot-dip galvanized and galvannealed coatings on steel. *Materials Characterization; (United States)*, 31(2):107–114, 1993.

[24] K.J. Keesman. *System Identification: An Introduction.* Advanced Textbooks in Control and Signal Processing. Springer London, 2011.

[25] K. Lee, J. Han, J. Park, B. Kim, and D. Ko. Prediction and control of front-end curvature in hot finish rolling process. *Advances in Mechanical Engineering*, 7(11):1–10, 2015.

[26] Chen Lei, Li Junhong, and Ding Ruifeng. Identification for the second-order systems based on the step response. *Mathematical and Computer Modelling*, 53(5-6):1074–1083, 2011.

[27] Lennart Ljung. *System Identification—Theory for the User.* Prentice Hall PTR, 2011.

[28] Lennart Ljung. *System Identification Toolbox - User's Guide.* The MathWorks Inc., Natick, Massachusetts, 2020. Version 9.12 (Release 2020a). Chapter 1, Page 1-54.

[29] Y. . Lu and S. W. Markward. Development and application of an integrated neural system for an hdcl. *IEEE Transactions on Neural Networks*, 8(6):1328–1337, 1997.

[30] Y. Lu and S. W. Markward. Development and application of an integrated neural system for an hdcl. *IEEE Transactions on Neural Networks*, 8(6):1328–1337, 1997.

[31] Smith J. M. Closer control of loops with dead time. *Chemical Engineering Progress*, 53(5):217–219, 1957.

[32] P. M. Makila and J. R. Partington. Shift operator induced approximations of delay systems. *SIAM Journal on Control and Optimization*, 37(6):1897–1912, 1999.

[33] A. R. Marder. Metallurgy of zinc-coated steel. *Progress in Materials Science*, 45(3):191–271, 2000.

[34] P. Naphade, A. Mukhopadhyay, and S. Chakrabarti. Mathematical modelling of jet finishing process for hot-dip zinc coatings on steel strip. *ISIJ International*, 45(2):209–213, 2005.

[35] J. E. Normey-Rico and E. F. Camacho. *Control of dead-time processes.* Advanced Textbooks in Control and Signal Processing. 2007.

[36] Z. . Pan, X. . Zhou, and P. Chen. Development and application of a neural network based coating weight control system for a hot-dip galvanizing line. *Frontiers of Information Technology and Electronic Engineering*, 19(7):834–846, 2018.

[37] J. . Richard. Time-delay systems: An overview of some recent advances and open problems. *Automatica*, 39(10):1667–1694, 2003.

[38] P. Sahoo and J. Paulo Davim. Comprehensive materials finishing : Surface finish coating. *IEEE Transactions on Industry Applications*, 3(3):38–55, 2017.

[39] I.V. Samarasekera. Hot rolling. *Encyclopedia of Materials: Science and Technology, Elsevier*, pages 3836–3843, 2001.

[40] M. Sbarciog, R. De Keyser, S. Cristea, and C. De Prada. Nonlinear predictive control of processes with variable time delay. a temperature control case study. In *Proceedings of the IEEE International Conference on Control Applications*, pages 1001–1006, 2008.

[41] Bart De Schutter and Ton van den Boom. Lecture notes for the course optimization in systems and control, September 2018.

[42] K. Shin, H. Park, and W. Chung. Synthesis method for the modelling and robust control of coating weight at galvanizing process. *ISIJ International*, 46(10):1442–1451, 2006.

[43] S. Skogestad. Simple analytic rules for model reduction and pid controller tuning. *Journal of Process Control*, 13(4):291–309, 2003.

[44] Sigurd Skogestad and Ian Postlethwaite. *Multivariable feedback control: Analysis and Design.* John Wiley, 2005.

[45] Vincent Theunynck and Steven Himpe. Design and advanced control of a process with variable time delay, 2006.

[46] J. A. Thornton and H. F. Graff. An analytical description of the jet finishing process for hot-dip metallic coatings on strip. *Metallurgical Transactions B*, 7(4):607–618, 1976.

[47] C. V. Tu and D. H. Wood. Wall pressure and shear stress measurements beneath an impinging jet. *Experimental Thermal and Fluid Science*, 13(4):364–373, 1996.

[48] Michel Verhaegen and Vincent Verdult. *Filtering and System Identification: A Least Squares Approach.* Cambridge University Press, 2007.

[49] Nicholas Roy Wigley. *Property prediction of continuous annealed steels.* PhD thesis, Cardiff University, 2012.

[50] H. Wu, R. Speets, G. Ozcan, R. Ekhart, R. Heijke, C. Nederlof, and C. J. Boeder. Non-linear model predictive control to improve transient production of a hot dip galvanising line. *Ironmaking and Steelmaking*, 43(7):541–549, 2016.

[51] Y. Zhang, Q. . Cui, F. . Shao, J. . Wang, and H. . Zhao. Influence of air-knife wiping on coating thickness in hot-dip galvanizing. *Journal of Iron and Steel Research International*, 19(6):70–78, 2012.

Glossary

List of Acronyms

AR	Auto-regressive
GM	Gain Margin
PM	Phase Margin
HDGL	Hot-dip galvanizing line
HSM	Hot Strip Mill
PHF	Preheating furnace
DFF	Direct fired furnace
RTH	Radiant tube heater
GJC	Gas jet cooler
MPC	Model Predictive Control
EPSAC	Extended Prediction Self-Adaptive Control
NEPSAC	Non-linear Extended Prediction Self-Adaptive Control
RMSE	Root Mean Square Error
CFD	Computational Fluid Dynamics

List of Symbols

ϵ	Prediction error
μ	Coating fluid viscosity
ϕ	Activation function
ρ	Coating fluid density
τ_d	Continuous-time delay
θ	Parameter vector

φ	Regression vector
b_p	Half-width of pressure distribution
d	Air-knife opening gap
dp/dx	Pressure gradient in x-direction
G	Non-dimensional effective gravitational acceleration
N_d	Discrete-time delay
p	Pressure imposed on the coating
P_0	Wiping gas pressure
p_m	Maximum Pressure
Q	Non-dimensional withdrawal flux
q	Withdrawal rate
S	Non-dimensional shear stress
u	Coating fluid velocity
V_s	Strip Speed
W	Non-dimensional coating thickness
w	Coating Thickness
Z	Strip-to-knife distance
τ	Shear Stress imposed on the coating
τ_{max}	Maximum Shear Stress